

# Structure development and properties in advanced injection molding processes : development of a versatile numerical tool

**Citation for published version (APA):**

Custódio, F. J. M. F. (2009). *Structure development and properties in advanced injection molding processes : development of a versatile numerical tool*. [Phd Thesis 1 (Research TU/e / Graduation TU/e), Mechanical Engineering]. Technische Universiteit Eindhoven. <https://doi.org/10.6100/IR641679>

**DOI:**

[10.6100/IR641679](https://doi.org/10.6100/IR641679)

**Document status and date:**

Published: 01/01/2009

**Document Version:**

Publisher's PDF, also known as Version of Record (includes final page, issue and volume numbers)

**Please check the document version of this publication:**

- A submitted manuscript is the version of the article upon submission and before peer-review. There can be important differences between the submitted version and the official published version of record. People interested in the research are advised to contact the author for the final version of the publication, or visit the DOI to the publisher's website.
- The final author version and the galley proof are versions of the publication after peer review.
- The final published version features the final layout of the paper including the volume, issue and page numbers.

[Link to publication](#)

**General rights**

Copyright and moral rights for the publications made accessible in the public portal are retained by the authors and/or other copyright owners and it is a condition of accessing publications that users recognise and abide by the legal requirements associated with these rights.

- Users may download and print one copy of any publication from the public portal for the purpose of private study or research.
- You may not further distribute the material or use it for any profit-making activity or commercial gain
- You may freely distribute the URL identifying the publication in the public portal.

If the publication is distributed under the terms of Article 25fa of the Dutch Copyright Act, indicated by the "Taverne" license above, please follow below link for the End User Agreement:

[www.tue.nl/taverne](http://www.tue.nl/taverne)

**Take down policy**

If you believe that this document breaches copyright please contact us at:

[openaccess@tue.nl](mailto:openaccess@tue.nl)

providing details and we will investigate your claim.

# **Structure development and properties in advanced injection molding processes**

*development of a versatile numerical tool*

CIP-DATA LIBRARY TECHNISCHE UNIVERSITEIT EINDHOVEN

Custódio, F.J.M.F.

Structure development and properties in advanced injection molding processes: development of a versatile numerical tool /  
by Frederico José Marques Ferreira Custódio. - Eindhoven: Technische Universiteit Eindhoven, 2009.

A catalogue record is available from the Eindhoven University of Technology Library. Proefschrift. - ISBN 978-90-386-1652-0

This thesis was prepared with the  $\text{\LaTeX}2_{\epsilon}$  documentation system.  
Reproduction: University Press Facilities, Eindhoven, The Netherlands.  
Cover design: Sjoerd Cloos.

This research was funded by the Portuguese Foundation for Science and Technology (FCT), under the PhD grant SFRH / BD / 16544 / 2004 / C3MW.

# **Structure development and properties in advanced injection molding processes**

*development of a versatile numerical tool*

PROEFSCHRIFT

ter verkrijging van de graad van doctor aan de  
Technische Universiteit Eindhoven, op gezag van de  
Rector Magnificus, prof.dr.ir. C.J. van Duijn, voor een  
commissie aangewezen door het College voor  
Promoties in het openbaar te verdedigen  
op maandag 16 maart 2009 om 16.00 uur

door

**Frederico José Marques Ferreira Custódio**

geboren te Leiria, Portugal

Dit proefschrift is goedgekeurd door de promotor:

prof.dr.ir. H.E.H. Meijer

Copromotoren:

dr.ir. G.W.M. Peters

en

dr.ir. P.D. Anderson

Saber? Que sei eu?  
Pensar é descrer.  
- Leve e azul é o céu -  
Tudo é tão difícil  
De compreender!...

A ciência, uma fada  
Num conto de louco...  
- A luz é lavada -  
Como o que nós vemos  
É nítido e pouco!

Que sei eu que abrande  
Meu anseio fundo?  
Ó céu real e grande,  
Não saber o modo  
De pensar o mundo!

Fernando Pessoa

To my parents



# Contents

---

<b>Summary</b>	<b>xi</b>
<b>1 Introduction</b>	<b>1</b>
<b>2 Modeling aspects</b>	<b>9</b>
2.1 Governing equations for the injection problem . . . . .	9
2.1.1 Flow problem . . . . .	10
2.1.2 Temperature problem . . . . .	14
2.1.3 Front-capturing technique . . . . .	17
2.1.4 Boundary conditions . . . . .	17
2.2 Numerical methods . . . . .	19
2.3 FEM formulation for the injection problem . . . . .	20
2.3.1 Flow problem . . . . .	20
2.3.2 Convection equation . . . . .	21
2.3.3 Energy equation . . . . .	23
2.4 Conclusions . . . . .	24
<b>3 Flow-induced stresses in gas-assisted injection molding</b>	<b>25</b>
3.1 Introduction . . . . .	25
3.2 Problem definition . . . . .	29
3.3 Flow-induced stresses . . . . .	30
3.3.1 Choice of the viscoelastic model . . . . .	30
3.3.2 Boundary conditions . . . . .	32
3.3.3 Numerical integration . . . . .	32
3.4 Case study . . . . .	32
3.4.1 Processing conditions . . . . .	33
3.4.2 Results & discussion . . . . .	35
3.5 Conclusions . . . . .	38



<b>4</b>	<b>Thermally and pressure-induced stresses in GAIM</b>	<b>43</b>
4.1	Introduction . . . . .	43
4.2	Thermally and pressure-induced stresses . . . . .	47
4.2.1	Linear thermo-viscoelastic model . . . . .	47
4.2.2	Incremental formulation . . . . .	50
4.2.3	Post-ejection structural analysis . . . . .	53
4.3	Case study . . . . .	54
4.3.1	Processing conditions . . . . .	54
4.3.2	Results & discussion . . . . .	55
4.4	Conclusions . . . . .	61
<b>5</b>	<b>Crystallization in injection molding prototype flows</b>	<b>63</b>
5.1	Introduction . . . . .	64
5.2	Injection molding prototype flows . . . . .	68
5.2.1	Material selection . . . . .	68
5.2.2	The multipass rheometer - morphology development under quasi-isothermal conditions . . . . .	70
5.2.3	The capillary rheometer - morphology development under non-isothermal conditions . . . . .	71
5.3	Morphological characterization by polarized optical light microscopy .	72
5.3.1	MPR experiments . . . . .	72
5.3.2	Capillary rheometer experiments . . . . .	73
5.4	Computation of the flow kinematics . . . . .	75
5.4.1	Viscous flow problem . . . . .	75
5.4.2	Boundary conditions . . . . .	79
5.5	Modeling crystallization . . . . .	80
5.5.1	Quiescent crystallization . . . . .	80
5.5.2	Modeling flow effects on crystallization . . . . .	85
5.6	Modeling results & discussion . . . . .	93
5.6.1	MPR . . . . .	93
5.6.2	Capillary rheometer . . . . .	100
5.7	Conclusions . . . . .	104
<b>6</b>	<b>3-D Simulation of Injection molding: exploring the RCE mold</b>	<b>107</b>
6.1	Introduction . . . . .	107
6.2	Rotation compression expansion mold - RCE mold . . . . .	109
6.3	Experimental procedures . . . . .	110
6.3.1	Material and processing conditions . . . . .	110
6.3.2	Microstructure characterization . . . . .	110
6.4	Experimental results & discussion . . . . .	112
6.5	3-D computations of the RCE mold . . . . .	116

---

6.5.1	Boundary conditions . . . . .	117
6.6	Computational results & discussion . . . . .	118
6.6.1	Benchmark problem . . . . .	118
6.6.2	RCE mold kinematics . . . . .	120
6.7	Conclusions . . . . .	124
<b>7</b>	<b>Conclusions and recommendations</b>	<b>127</b>
7.1	Conclusions . . . . .	127
7.2	Recommendations . . . . .	129
	<b>Samenvatting</b>	<b>143</b>
	<b>Acknowledgments</b>	<b>145</b>
	<b>Curriculum vitae</b>	<b>147</b>



# Summary

---

Injection molding is one of the most widespread technologies for processing polymer products. The capability to shape parts of complex geometry at high production rates justifies its extensive use and range of applications. Even though injection molding is used for the processing of different types of resins, most of the injection molded polymers are thermoplastics. Ever since the early 1950s injection molding has been playing an important role in polymer processing industry. Since then it has benefited from significant technological developments. Many of which have been aimed at improving production efficiency and enhancing the quality of molded parts. Also, variations of the conventional technology, referred to as non-conventional injection molding techniques, have been developed and commercialized by machine manufacturers. Notably, gas-assisted injection molding and multi-component injection molding. Additionally to these developments, the injection molding process has become more of an integrative manufacturing process. Today complex products made of different materials including metallic components can be obtained within a single injection molding cycle. As production processes tend to become more complex, additional challenges are posed by product developers. More specifically, the decreasing length scales of products, the combination of multiple materials and the need to control products' properties throughout their lifetime, are some of the critical issues that demand for research effort.

Numerical models of injection molding have been under development for the past 30 years. The focus of such models has mostly been on the improvement of product's design in order to avoid such problems as inhomogeneous filling of the mold cavity, unbalanced pressure and thermal fields, and typical product defects like weld lines and air traps. A next step was the development of numerical models aimed at property prediction. Notably, significant research was devoted to predict shrinkage and warpage of injection molded amorphous polymers.

Given the usefulness of such predictive approaches to product developers, this thesis aims to contribute new routes to predict the final properties of injection molded parts.

Continuing previous work done in our group, we further extend a fully 3-D numerical model for injection molding, VIp3D, whose equations and numerical methods we present in Chapter 2. On this numerical platform we implement several models to predict the morphology and related properties of injection molded parts. In Chapter 3 we study the processing of amorphous polymers via gas-assisted injection molding (GAIM), analyzing the development of residual stresses in a simple geometry. More specifically, we analyze first the impact of this technology on the frozen-in orientation and, consequently, on the development of flow-induced stresses. A decoupled approach is adopted in which elastic effects are assumed not to influence the flow kinematics. Then, in Chapter 4, we assess how thermally and pressure-induced stresses develop in the GAIM process, using a linearized viscoelastic model. In order to make our analysis comparable, we model the injection molding of a 3-D-approximated geometry using standard injection molding and GAIM. For each case the resulting residual stresses are predicted.

The remaining part of the thesis addresses semi-crystalline polymers, and focuses on how the morphology of isotactic Polypropylene (iPP) evolves upon injection molding. Given the complexity of the crystallization phenomenon, and its strong dependence on flow conditions, its study under the complex thermomechanical environment of the injection molding process is not straightforward. Furthermore, one cannot neglect the influence of the flow history acquired during plastification on the microstructure of the final parts. Thus, simpler flows, with well defined conditions, are required to validate crystallization kinetics models. In Chapter 5 we first analyze and model the morphology development of iPP in two experimental setups: a multipass rheometer and a capillary rheometer. In both of these devices the material is subjected to well-defined flow conditions with a controlled deformation history. Hence, valid correlations can be drawn between processing conditions and the developed morphologies. To predict the final morphology of samples, we employ a model in which a set of differential-type equations is solved in a staggered way with the flow problem. The model describes the morphology being developed in terms of the shape, size and volume of crystalline structures. The predicted thickness of the oriented layers is compared with polarized optical microscopy results. The modeling of such experiments is a necessary first step prior to facing all the complexities of a real injection molding process. In this thesis, we will refer to these experiments as prototype flows.

In Chapter 6, we present a combined experimental and numerical study on the morphology development of injection molded iPP discs. Injection molding experiments are conducted using the innovative RCE (rotation compression and expansion) mold, that can impose additional drag and squeezing flows, from the rotation and linear displacement of one of its walls, to the melt during the filling phase. In order to assess the influence of the operating mold parameters, we characterize the microstruc-

ture and measure the molecular orientation of the injection molded discs. Fully 3-D simulations are then carried out to compute the flow kinematics induced by the RCE mold, and therefore relate this to the developed microstructure.

Chapter 7 summarizes the main conclusions of this work and presents recommendations for future research in the field of predicting the morphology and microstructure of injection molded products via numerical modeling.



## CHAPTER ONE

# Introduction

---

## Injection molding

In polymer processing, injection molding is second only to extrusion in terms of production quantities. It is used to process a vast range of polymeric products in many different applications, from plastic commodities to complex automotive components. Even though significant technological developments have greatly enhanced the efficiency of the process and the quality of molded parts, the working principle of an injection molding machine has remained unchanged, and is illustrated in Figure 1.1.

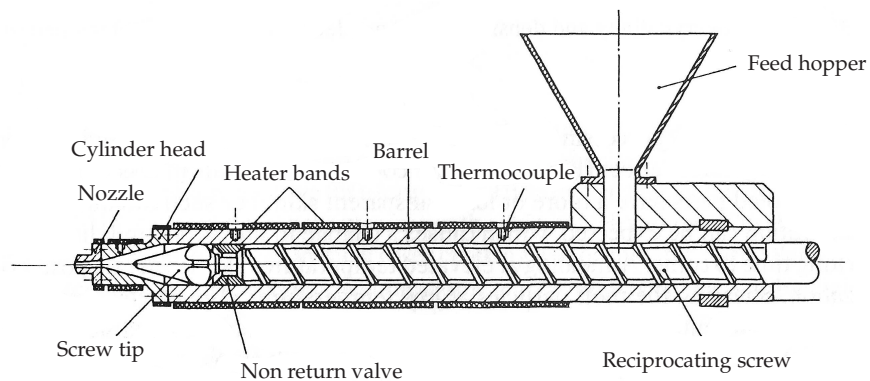


**Figure 1.1:** Injection unit of an injection molding machine.

The process starts with the addition of solid material in the form of granules or powder via a hopper into an extruder, which consists of a reciprocating screw inside a



heated barrel. There, the material granules (or powder), by the combined action of heating and mechanical work, are transformed into a homogeneous melt that is transported towards the front of the screw. This process is called plastification, and plays an important role in the quality of molded parts. A proper plastification should result in a uniform temperature and, consequently, a uniform viscosity of the melt, which is essential to avoid product defects [92]. After plastification of sufficient polymer, the screw is pushed forward by a hydraulic cylinder causing the material to flow through the nozzle into the mold cavity. The molding cycle consists of three phases: an injection phase, a packing phase and a holding phase, which can be depicted by the time evolution of pressure inside the mold cavity, see Figure 1.2.

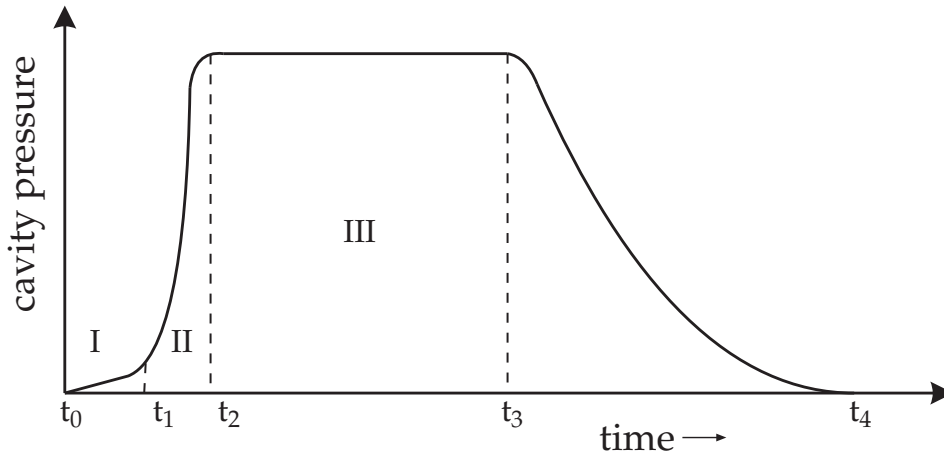


**Figure 1.2:** Pressure evolution inside the mold during the injection molding cycle.

During the injection phase (I),  $t_0 \rightarrow t_1$ , the polymer melt fills the mold cavity until the cavity is just filled. During the compression phase (II),  $t_1 \rightarrow t_2$ , typically an extra 15% of material is forced into the mold cavity, characterized by a steep increase of the pressure level inside the cavity. Last, the holding phase takes place (III),  $t_2 \rightarrow t_3$ , during which additional material is forced through the still molten core to compensate for the volumetric change that the material undergoes upon cooling. The switch from injection pressure to holding pressure can be made dependent on different criteria: volume of injected material, injection pressure, clamping force or pressure inside the cavity. The latter is accepted to give the best results in terms of parts' quality. Upon switching to the holding phase, a holding pressure is specified rather than a certain volume flow rate. As the gate freezes-off at time  $t_3$ , and no additional material can be forced into the mold, the pressure begins to decay until the end of the cycle ( $t_4$ ), upon which the part is ejected.

## Non-conventional injection molding techniques

A number of variations of the conventional injection molding process have been developed. Gas-assisted injection molding, GAIM, is a process which involves partial filling of the mold cavity with polymer melt, followed by injection of gas through the molten core to complete filling and supply a packing pressure, see Figure 1.3(b). GAIM processes usually employ a needle placed inside the injection nozzle, from where gas is injected, see Figure 1.3(a). GAIM allows the injection molding of parts with both thin (typically < 5 mm) and thick (typically > 5 mm) regions, which under the conventional technology would develop surface defects (sink marks) due to the high volumetric shrinkage. The process significantly reduces cooling times, injection pressure and clamping force, since the packing and holding phases are done at much lower pressure levels. Other advantages include design flexibility, weight reduction and an improved dimensional stability.

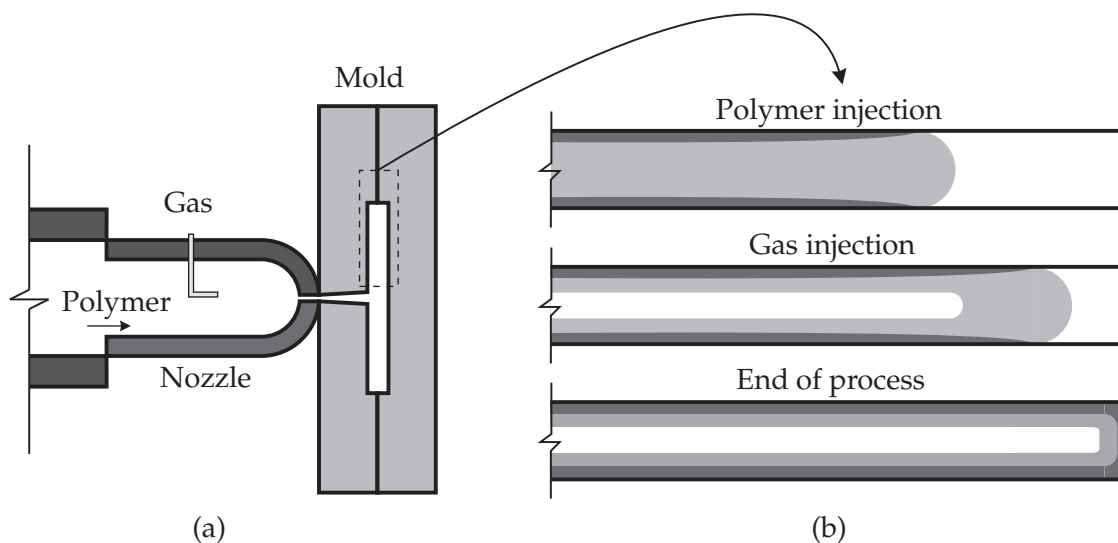


**Figure 1.3:** (a) Injection nozzle equipped with a gas injection needle. (b) Filling a mold cavity via GAIM: dark gray denotes the solidified polymer layer and light gray the polymer melt. The white core denotes the gas.

## Structure development in injection molding

The final properties of injection molded parts are the result of a complex interaction between the polymer molecular structure, the processing conditions and the geometry of the part. During the injection molding cycle, the material is subjected to severe conditions. It has to be heated into the liquid state, subjected to high pressures (up to 100 MPa) and, subsequently, quenched at high cooling rates (up to  $100 \text{ K s}^{-1}$ ). Such changes in the material state take place within seconds and, therefore, far beyond equilibrium. Depending on the polymer type, e.g. amorphous or semi-crystalline,

the problems associated with processing and property tailoring change, since the underlying physical processes and related material-states change.

For amorphous polymers, processing conditions mainly affect the optical and mechanical behavior. A critical issue is the dimensional stability of molded parts. In Figure 1.4 we show the time evolution of strain in a polystyrene injection molded strip [12] induced by dimensional changes. Its length decreases and its width increases in a non-uniform manner (the increase is largest close to the gate). Such dimensional

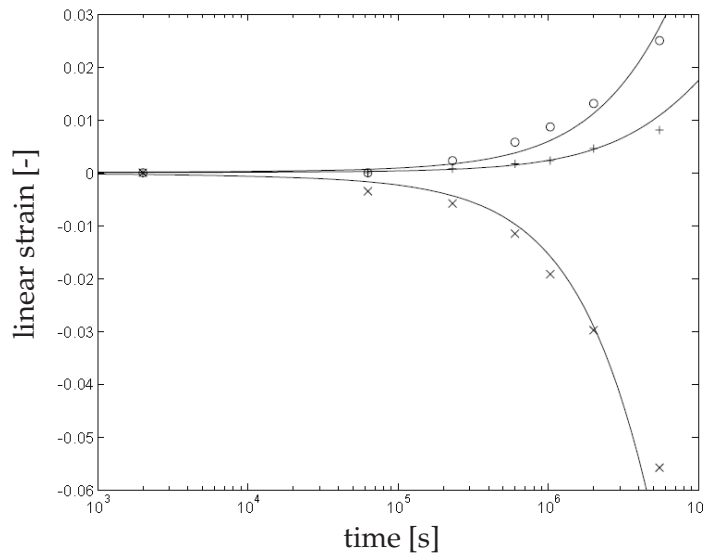


**Figure 1.4:** Measured (symbols) and predicted (lines) strain due to recovery of the length ( $\times$ ), and width at 75( $\circ$ ) and 110( $+$ ) mm from the gate. Storage temperature 343 K; Caspers [12].

changes are induced by several factors: density changes throughout the molded part, relaxation of thermally and pressure-induced stresses, which yield short-term dimensional changes, and relaxation of the frozen-in flow-induced stresses, which relate to molecular orientation. All of these affect the dimensional stability of molded parts, although the time scales of their occurrence are different. Changes in density, apart from physical ageing, occur directly during cooling, and can induce anisotropic shrinkage, since the pressure and cooling history is different for each material fluid point. Thermally and pressure-induced residual stresses mostly determine short term geometrical changes that often result in warpage of the part. They originate from differential shrinkage, induced by the combined effect of inhomogeneous cooling and vitrification under a transient pressure field. These stresses were computed in [8] and are responsible for the existence of tensile stresses in the surface of injection molded parts, see Figure 1.5(a).

Birefringence is a key property for many applications and is solely determined by the degree of frozen-in orientation, which affects, besides the optical behavior, the

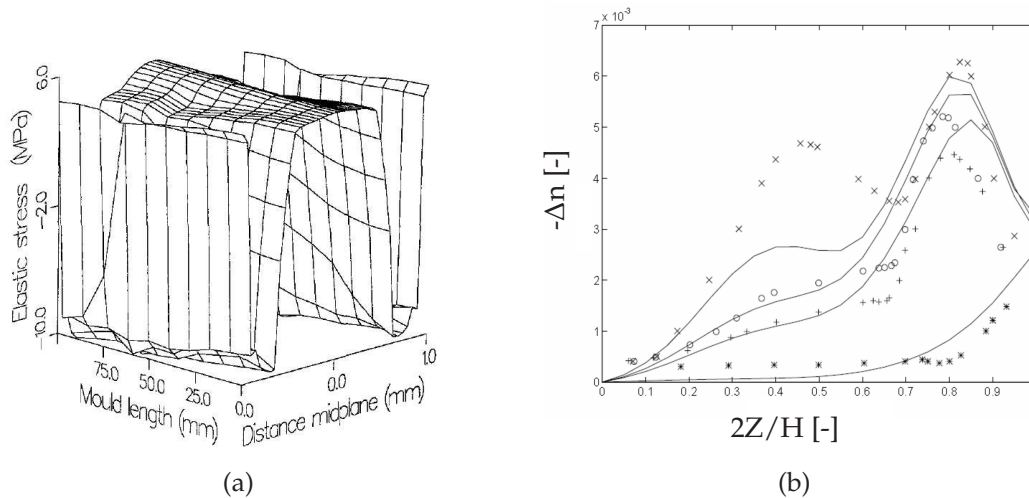


**Figure 1.5:** (a) Computed thermally and pressure induced stress profile in an injection molded strip upon ejection (Baaijens [8]). (b) Measured (symbols) and predicted (lines) residual birefringence across half the thickness at 25( $\times$ ), 41( $\circ$ ), 60( $+$ ) and 110( $*$ ) mm from the gate (Caspers [12]).

long term dimensional stability of molded parts as shown in Figure 1.4. In Figure 1.5(b) we show the predicted and measured residual birefringence ( $\sim$  orientational entropic stresses) profile across the thickness of an injection molded strip. Upon processing, molecules attain a preferential orientation according to the flow direction. In Figure 1.6(a) we schematically illustrate the flow kinematics involved during the filling phase of injection molding, in which the velocity profile and the local phenomena in the flow front (fountain flow), determine the molecular orientation during filling, see Figure 1.6(b).

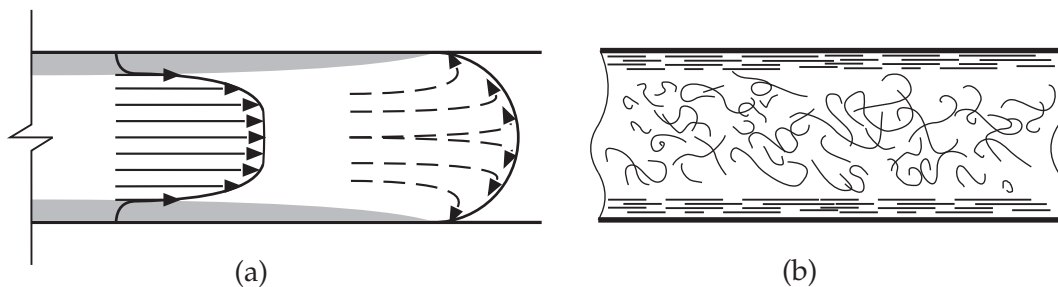


**Figure 1.6:** (a) Velocity profile during filling and (b) resulting molecular orientation upon the filling phase.

Typically, close to the wall the orientation of molecules is frozen-in, and is reflected by the first peak in birefringence in Figure 1.5(b). In the core region, due to fast molecular relaxation, random coils exist. The second peak in orientation originates from the packing phase when material flows through the still molten core to com-

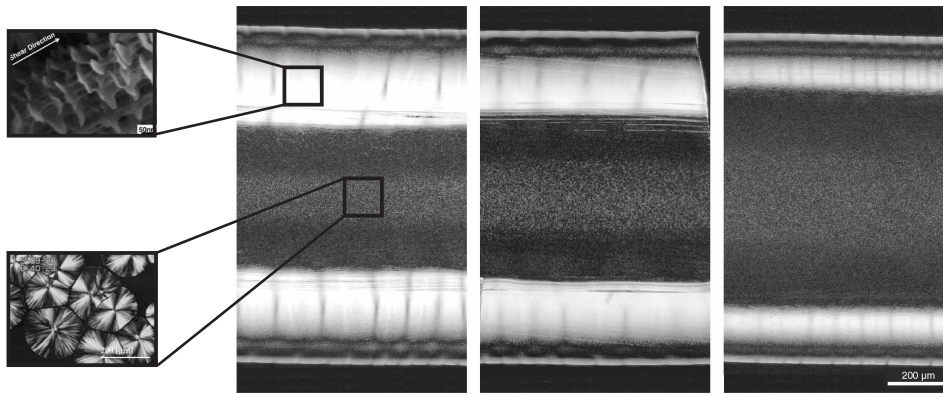


**Figure 1.7:** Optical micrographs of injection molded samples of HDPE at positions (from left to right) close to the gate, in the middle of samples and far from the gate, reproduced from Schrauwen et al. [97]. The enlargements are shown in order to illustrate the underlying crystalline structures in the different morphological layers: shish kebabs in the oriented layer (top left), reproduced from [43], and spherulites in the core region (bottom left), reproduced from [115].

compensate for shrinkage. Although velocity gradients are small during packing, significant orientation is still induced given the long relaxation times of molecules at low temperatures. In time, relaxation processes induced by the lower entropy associated with oriented molecules yield dimensional changes.

In the case of semi-crystalline materials the difficulties in controlling the final properties of injection molded parts are significantly higher, since these materials crystallize in an anisotropic manner under the complex inhomogeneous thermal and mechanical histories that material elements experience in the injection molding process. Therefore, unlike amorphous polymers, not only the high end tail of the molecular weight distribution orients, but all molecules become involved in the oriented crystallization process. Even though the influence of thermal history on crystallization kinetics is well understood, the drastic (and overruling) effect of flow on crystallization is still far from a comprehensive understanding. Since flow and temperature histories change for each material point during processing, crystallization kinetics are locally defined. Typically, the morphology of an injection molded part, when visualized under optical light microscopy, consists of different layers: a highly oriented layer close to the mold wall, a transition layer followed by an oriented shear layer (where the shear rates are highest), and a spherulitic core at the center of the sample. Such a morphology can be seen in Figure 1.7, as well as the evolution (change in thickness) of oriented layers along the flow path. The fibrillar type of crystalline structures observed in the oriented layer are the so-called shish-kebab structures whose length and density are highly dependent on flow conditions.

The intrinsic anisotropy of injection molded parts made of semi-crystalline materials was investigated by Schrauwen et al. [97], who analyzed the resulting anisotropic mechanical behavior of injection molded strips made of high density polyethylene (HDPE). Tensile specimens were cut from the strips parallel to the flow direction

and perpendicular to it at different locations, see Figure 1.8. Different behavior is measured. The tensile bars cut parallel are found to behave in a ductile manner and to deform homogeneously. Those cut perpendicular behave in a brittle manner close to the gate, while far from it necking occurs.

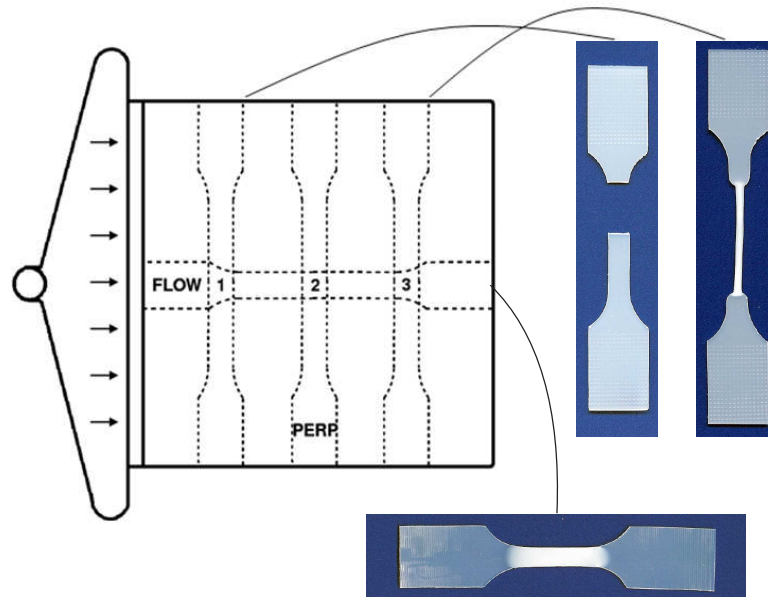


**Figure 1.8:** Schematic drawing of an injection molded strip with a V-shaped gate. Cutting positions for parallel and perpendicular to flow tensile specimens are indicated. Corresponding results of the tensile tests are illustrated (Schrauwen [96]).

## Modeling of injection molding

Over the past three decades, much effort has been spent on modeling the injection molding process. It is beyond the scope of this short introduction to review all of its development stages, but for a detailed review the reader is referred to [62, 83]. After Hieber and Shen first proposed the so called  $2\frac{1}{2}$ -D approach, most modeling work followed this method [14–16, 36, 59, 88, 90, 107]. Other related processes, such as multi-component injection molding [133] and gas-assisted injection molding [119], have also been modeled within the  $2\frac{1}{2}$ -D frame. This approach makes use of a lubrication approximation: the pressure field is solved with finite elements in 2-D and the temperature and velocity fields with finite differences in 3-D. Even though this method benefits from lower computation times, it is limited to cavities for thin walled, weakly curved, but geometrically complex products. Moreover, the flow kinematics are oversimplified, neglecting the fountain flow effect [18] and the local phenomena in junctions and corners.

With the tremendous increase of computing power, the numerical modeling of injection molding, in which the velocity, pressure and temperature field are computed

fully 3-D, has become possible, e.g. [31, 47, 49, 117]. In [31], Haagh has shown 3-D simulations of the injection molding process and gas-assisted injection molding using a pseudo concentration method [117] to track the material-fluid points and to capture the polymer-air and polymer-gas interface. He applied dynamic Robin boundary conditions at the mold walls to impose a slip or no-slip condition, depending on the local concentration, i.e. air or polymer. In [47], full 3-D simulations of injection molding were also computed, but a level-set method [85] was used instead to capture the interface. The model was further extended in [49] to simulate co-injection molding.

### **Scope of this work**

This work deals with the development of a numerical tool to predict the morphology and properties of injection molded parts. More specifically, by modeling the complex thermal-mechanical environment of injection molding, it assesses the predictive capabilities of novel constitutive and kinetic models, to describe the morphological changes in the microstructure of injection molded materials.

A model to predict flow-induced, thermally-induced and pressure-induced stresses in injection molded parts of amorphous polymers, is now derived for the case of gas-assisted injection molding.

Complex crystallization phenomena in injection molding are usually addressed with phenomenological models that try to predict the material morphology developed upon injection. The use of elaborated rheological models, which couple molecular deformation to crystallization, is usually restricted to simple experiments under mild flow conditions. In this work we propose a model, within the framework of molecular-based rheological modeling, to predict the development of the microstructure of the crystalline phase in injection molded parts.

The influence of processing conditions on the microstructural development of semi-crystalline polymers is further assessed by the use of an innovative molding tool, the RCE (rotation, compression and expansion) mold [102]. By imposing controlled in-plane and through the thickness deformation fields during mold filling, this mold allows the microstructure development in injection molding discs to be manipulated. An experimental and numerical approach is adopted to understand how the complex flow fields generated relate to the microstructure developed.

The thesis ends by summarizing the major conclusions and giving recommendations for future research.

## CHAPTER TWO

# Modeling aspects

---

### Abstract

In this chapter, we introduce the balance equations and, subsequently, decompose the injection problem into a flow problem and a temperature problem. For each of these problems the governing equations are simplified with respect to the process requirements and modeling assumptions. The related constitutive equations and boundary conditions are given and justified, and a numerical method is introduced that deals with the multi-component flow problem, referred to as front-capturing method.

### 2.1 Governing equations for the injection problem

The balance equations for mass, momentum and internal energy read:

$$\frac{\partial \rho}{\partial t} + \nabla \cdot \rho \mathbf{u} = 0, \quad (2.1)$$

$$\rho \frac{\partial \mathbf{u}}{\partial t} + \rho \mathbf{u} \cdot \nabla \mathbf{u} = \nabla \cdot \boldsymbol{\sigma} + \rho \mathbf{g}, \quad (2.2)$$

$$\rho \dot{e} = \boldsymbol{\sigma} : \mathbf{D} - \nabla \cdot \mathbf{q} + \rho r + \rho h_r R_c, \quad (2.3)$$

where  $\rho$  represents density and  $\mathbf{u}$  the velocity field,  $\boldsymbol{\sigma}$  the Cauchy stress tensor,  $\mathbf{g}$  is the body force per unit mass and  $\dot{e}$  is the rate of change of internal energy. The terms on the right-hand side of the energy equation, Equation (2.3), represent the work done to deform the material, with  $\mathbf{D}$  the rate of deformation tensor, the heat transferred by conduction, with  $\mathbf{q}$  the heat flux, the heat transferred by radiation,  $r$ ,



and internal heat generation with  $R_c$  the reaction rate, and  $h_r$  the reaction heat. To solve these equations appropriate constitutive equations have to be specified for the Cauchy stress tensor, the heat flux, as well as an equation of state for the density and internal energy, i.e.  $e = e(p, T)$ , where  $p$  and  $T$  denote pressure and temperature respectively, introduced in the forthcoming section. Additionally, initial and boundary conditions have to be prescribed.

### 2.1.1 Flow problem

During the filling phase, the effects of compressibility on flow are negligible, but during the packing and holding phases compressibility becomes the key phenomenon that drives the development of residual orientation and stresses. As pointed out by Shoemaker [101], during the packing phase typically up to 15% of additional polymer can be pushed into the mold. Since we want to describe all phases of the injection molding process in a single model, we consider the polymer density to be dependent on the state variables, temperature and pressure:

$$\rho = \rho(p, T). \quad (2.4)$$

In injection molding the flow kinematics are mostly determined by kinematic boundary conditions, characterized by no slip conditions at the walls, and by a prescribed flow rate, or pressure, at the gate. Therefore, the precise choice of the constitutive equation for the stress tensor in the momentum equation, has only a small effect on the overall kinematics as long as the shear viscosity is captured correctly. Clearly, in regions with bifurcations or close to the flow front, where significant elongation takes place, this assumption is violated. Nevertheless, a viscous approach, versus a viscoelastic approach, has the advantages of saving a tremendous amount of computing effort and avoiding flow instabilities that arise at high Weissenberg numbers, see Hulsen et al. [44], which are typical for injection molding flow conditions. The influence of viscoelastic instabilities in injection molding was notably analyzed by Grillet et al. [29] and Bogaerds et al. [10], however such analysis are beyond the scope of this thesis.

The constitutive equation for the Cauchy stress tensor  $\boldsymbol{\sigma}$  is given by:

$$\boldsymbol{\sigma} = -p\mathbf{I} + \boldsymbol{\tau}, \quad (2.5a)$$

$$p = p_0 - \mu \text{tr}(\mathbf{D}), \quad (2.5b)$$

$$\boldsymbol{\tau} = 2\eta\mathbf{D} - \frac{2}{3}\eta(\text{tr}(\mathbf{D}))\mathbf{I} = 2\eta\mathbf{D}^d, \quad (2.5c)$$

where  $\mu$ , the bulk viscosity, expresses the difference between the thermodynamic pressure  $p$  in a non-equilibrium state (flowing fluid) and the equilibrium pressure  $p_0$ . According to Batchelor [9]  $\mu$  can be regarded as an expansion damping coefficient which accounts for the pressure lag in a system with continuously changing

**Table 2.1:** Characteristic values of injection molding process variables for thermoplastics.

variable	unit	characteristic value	
		polymer	air
$\rho_0$	kg m <sup>3</sup>	10 <sup>3</sup>	1
$\eta_0$	Pa s <sup>-1</sup>	10 <sup>4</sup>	10 <sup>-5</sup>
$c_{p0}$	J kg <sup>-1</sup> K <sup>-1</sup>	10 <sup>3</sup>	10 <sup>3</sup>
$\lambda_0$	W m <sup>-1</sup> K <sup>-1</sup>	10 <sup>-1</sup>	10 <sup>-2</sup>
$\alpha_0$	K <sup>-1</sup>	10 <sup>-6</sup>	10 <sup>-3</sup>
$k_0$	Pa <sup>-1</sup>	10 <sup>-9</sup>	10 <sup>-5</sup>
$L$	m	10 <sup>-1</sup>	
$H$	m	10 <sup>-3</sup>	
$U$	m s <sup>-1</sup>	10 <sup>-1</sup>	
$\tau$	s	10 <sup>0</sup> - 10 <sup>1</sup>	

state variables, namely  $\rho$  and the internal energy  $e$ . For most cases, except those in which rates of expansion approach the order of magnitude of shear rates, e.g. shock waves, the term  $\mu \text{tr}(\mathbf{D})$  can be neglected. We assume a generalized Newtonian behavior in which the viscosity is made dependent on pressure, temperature and  $\mathbf{D}^d$ , the deviatoric part of the rate of deformation tensor  $\mathbf{D}$ . It reads:

$$\eta = \eta(p, T, \mathbf{D}^d). \quad (2.6)$$

In order to assess the relevance of compressibility in the momentum equation, when modeling the injection molding process, we carry out a scaling analysis to find the order of magnitude of the compressible terms. For that, we need to introduce characteristic time and length scales, as well as the order of magnitude of related variables in the injection molding process, listed in Table 2.1. Additionally, the equations' variables are replaced by the dimensionless ones, given in Table 2.2. The coordinates are scaled with respect to the characteristic length scales  $L$  and  $H$ . The ratio  $\epsilon$  denotes the type of geometry, thin-walled geometries are characterized by  $\epsilon \ll 1$ . The velocity components  $v$  and  $w$  are coupled to the characteristic velocity  $U$  via the ratio  $\epsilon$ . Since compressibility only affects the extensional stresses, we rewrite the extra stress tensor taking only the normal components into account:

$$\tau_{ii} = 2\eta \frac{\partial u_i}{\partial x_i} - \frac{2}{3}\eta(\text{tr}(\mathbf{D})) \quad \text{for } i = 1, 2, 3. \quad (2.7)$$

Before attempting to write a dimensionless form of Equation (2.7), we start by rewriting the continuity equation introducing the state variables, pressure and temperature ( $p, T$ ):

**Table 2.2:** Dimensionless variables.

$x = x^*L$	$y = y^*L$	$z = z^*H = z^*\epsilon L$
$\epsilon = \frac{H}{L}$	$u = u^*U$	$v = v^*V = v^*\epsilon U$
$w = w^*W = w^*\epsilon U$	$t = t^*\tau$	$T = T^*(\Delta T)_0$
$p = p^*\Delta p_0$		

$$\text{tr}(\mathbf{D}) = \nabla \cdot \mathbf{u} = -\frac{1}{\rho} \left( \frac{\partial \rho}{\partial t} + \mathbf{u} \cdot \nabla \rho \right), \quad (2.8)$$

$$\text{tr}(\mathbf{D}) = -\frac{1}{\rho} \left( \frac{D\rho}{Dt} \right), \quad \rho(T, p), \quad (2.9)$$

thus

$$\text{tr}(\mathbf{D}) = -\frac{1}{\rho} \left( \frac{\partial \rho}{\partial T} \dot{T} + \frac{\partial \rho}{\partial p} \dot{p} \right). \quad (2.10)$$

Introducing in Equation (2.10) the thermal expansion coefficient and the isothermal compressibility defined as:

$$\alpha = -\frac{1}{\rho} \left( \frac{\partial \rho}{\partial T} \right)_p, \quad (2.11)$$

$$\kappa = \frac{1}{\rho} \left( \frac{\partial \rho}{\partial p} \right)_T, \quad (2.12)$$

respectively, it yields:

$$\text{tr}(\mathbf{D}) = \alpha \left( \frac{\partial T}{\partial t} + \mathbf{u} \cdot \nabla T \right) - \kappa \left( \frac{\partial p}{\partial t} - \mathbf{u} \cdot \nabla p \right). \quad (2.13)$$

The dimensionless form of Equation (2.13) can be found by replacing the original variables by dimensionless ones, given in Table 2.2:

$$\text{tr}(\mathbf{D})^* = \frac{\alpha \Delta T_0}{\tau} \frac{\partial T^*}{\partial t^*} + \frac{U \alpha \Delta T_0}{H} \mathbf{u}^* \cdot \nabla^* T^* - \frac{\kappa \Delta p_0}{\tau} \frac{\partial p^*}{\partial t^*} - \frac{U \kappa \Delta p_0}{L} \mathbf{u}^* \cdot \nabla^* p^*, \quad (2.14)$$

where  $\nabla T$  is scaled with respect to  $\Delta T_0/H$ , and  $\nabla p$  with respect to  $\Delta p_0/L$ .

Having found a dimensionless form for  $\text{tr}(\mathbf{D})$ , we can next write the extra stress tensor, Equation (2.7), in a dimensionless form. After dividing by  $(\eta_0 U/L)$  it reads:

$$\tau_{ij}^* = 2 \frac{\partial u_i^*}{\partial x_j^*} - \frac{2}{3} \left( \frac{\alpha \Delta T L}{\tau U} \frac{\partial T^*}{\partial t^*} + \frac{\alpha \Delta T L}{H} \mathbf{u}^* \cdot \nabla^* T^* - \frac{\kappa \Delta p_0 L}{\tau U} \frac{\partial p^*}{\partial t^*} - \kappa \Delta p_0 \mathbf{u}^* \cdot \nabla^* p^* \right). \quad (2.15)$$

Next we estimate the order of each term in Equation (2.15). A characteristic pressure drop,  $\Delta p_0$ , is defined as  $\eta_0 L U / H^2$ , and the characteristic time for packing and holding is assumed to range between one to ten seconds. Using the characteristic values given in Table 2.1 we find:

$$\frac{\alpha \Delta T L}{\tau U} = 10^{-4} \quad \text{or} \quad 10^{-5} \quad (2.16)$$

$$\frac{\alpha \Delta T L}{H} = 10^{-2} \quad (2.17)$$

$$\frac{\kappa \Delta p_0 L}{\tau U} = 10^{-2} \quad \text{or} \quad 10^{-3} \quad (2.18)$$

$$\kappa \Delta p_0 = 10^{-2} \quad (2.19)$$

Clearly compressibility effects can be neglected, i.e.,

$$\|\text{tr}(\mathbf{D})\mathbf{I}\| \ll \|\mathbf{D}\|. \quad (2.20)$$

Inertia can also be neglected in injection molding simulations due to the dominance of viscous forces. Estimating the Reynolds number  $\text{Re} = \frac{\rho_0 U H}{\eta_0}$  using the values in Table 2.1, one finds it to be of order  $10^{-5}$  for the polymer and  $10^2$  for air. In order to circumvent problems caused by the relatively high Reynolds number on the air/gas phase, we model the air and gas phases with a fictitious fluid whose viscosity is set  $10^4$  lower than that of the polymer melt and with a density set equal to air density. This allows to neglect inertia in all phases, i.e. polymer melt and fictitious fluid/gas, and hence, solve only the Stokes equation, Equation (2.22), for the entire computational domain. During the filling phase we consider the flow to be incompressible and only during the subsequent packing and holding phases we model the material's compressibility. Using these assumptions, the continuity and momentum equations reduce, in the injection phase, to:

$$\nabla \cdot \mathbf{u} = 0, \quad (2.21)$$

$$\nabla p = \nabla \cdot \boldsymbol{\tau}, \quad (2.22)$$

in which  $\boldsymbol{\tau}$  is the extra stress tensor. For the packing and holding phases, the full form of the mass balance, Equation (2.1), is solved. A constitutive equation for the specific volume is still to be specified. The extra stress tensor according to the generalized Newtonian flow description is given by:

$$\boldsymbol{\tau} = 2\eta(T, p, \mathbf{D}^d)\mathbf{D}. \quad (2.23)$$

The specific relation for  $\eta(T, p, \mathbf{D}^d)$  will be specified later on.

### 2.1.2 Temperature problem

Under the assumption that thermal radiation is negligible during the filling, packing and holding stages in injection molding, and considering that no heat source is present in the process, the energy balance equation, Equation (2.3), reduces to:

$$\rho\dot{e} = \boldsymbol{\tau} : \mathbf{D} - \nabla \cdot \mathbf{q}. \quad (2.24)$$

The extra stress tensor,  $\boldsymbol{\tau}$ , in Equation (2.24) is defined in Equation (2.23). Batchelor [9] derives from thermodynamic considerations that the change in internal energy can be expressed as:

$$\rho\dot{e} = \rho c_p \dot{T} - \alpha T \dot{p}, \quad (2.25)$$

with  $\alpha$  the thermal expansion coefficient, defined in Equation (2.11). The last term of Equation (2.25) represents the heat of compression. The heat capacity,  $c_p$ , is a local material property that is a function of pressure, temperature and the material label  $c$  (i.e. polymer or air/gas).

$$c_p = c_p(c). \quad (2.26)$$

We apply Fourier's law as the constitutive relation between heat flux and temperature. Assuming isotropic heat conduction it reads:

$$\mathbf{q} = -\lambda \nabla T. \quad (2.27)$$

The heat conduction coefficient,  $\lambda$ , can be a function of pressure and temperature, however in this study it is set only to depend on the material label  $c$  (i.e. polymer or air/gas),

$$\lambda = \lambda(c). \quad (2.28)$$

Introducing Equations (2.25)–(2.28) in Equation (2.24) yields:

$$\rho c_p \dot{T} = 2\eta \mathbf{D} : \mathbf{D} + \nabla \cdot (\lambda \nabla T) + \alpha T \dot{p}. \quad (2.29)$$

For amorphous polymers, the glass transition temperature,  $T_g$ , is used as a criterion

for a non-flow condition. Below  $T_g$  the fluid viscosity is set to a value that exceeds the melt viscosity by a factor of  $10^4$ , which means that the velocity at the *solidified* layer is almost zero.

### Scaling the energy equation

In order to simplify the problem, and reduce computation times, a scaling analysis is performed on the energy equation, Equation (2.29), to identify the terms relevant for the injection molding process.

The shear rate,  $\dot{\gamma}$ , is related to the second invariant of the rate of deformation tensor  $II_{2D}$  according to:  $\dot{\gamma} = \sqrt{|II_{2D}|}$ , with  $II_{2D}$  defined as  $II_{2D} = \text{tr}(\mathbf{2D})^2 - \text{tr}(\mathbf{2D}^2)$ . Using Tables 2.1 and 2.2, and introducing the ratio  $\epsilon$  to scale all coordinates with respect to the same characteristic length ( $L$ ), we find the order of these two terms to be:

$$\text{tr}(\mathbf{2D})^2 \sim \mathcal{O}\left(\left(\frac{U}{L}\right)^2 \left(\frac{\partial u}{\partial x}\right)^2\right), \quad (2.30)$$

and

$$\text{tr}(\mathbf{2D}^2) \sim \mathcal{O}\left(\left(\frac{U}{\epsilon L}\right)^2 \left(\frac{\partial u^*}{\partial z^*}\right)^2\right). \quad (2.31)$$

Since  $\epsilon$  is of order  $10^{-2}$  we find  $\text{tr}(\mathbf{2D})^2 \ll \mathbf{2D} : \mathbf{D}$ . Thus, for scaling purposes the shear rate can be reduced to  $\dot{\gamma} = \sqrt{\mathbf{2D} : \mathbf{D}}$ , with its order of magnitude determined by the highest velocity gradient:

$$\dot{\gamma}^* = \frac{U}{\epsilon L} \frac{\partial u^*}{\partial z^*}. \quad (2.32)$$

The dimensionless form of the energy equation reads:

$$\begin{aligned} \frac{1}{\epsilon^2 \text{Fo}} \frac{\partial T^*}{\partial t^*} + \epsilon \text{Pe} \mathbf{u}^* \cdot \nabla^* T^* &= 2\text{Br} \dot{\gamma}^{*2} + \nabla^* \cdot (\lambda^* \nabla^* T^*) + \\ &\frac{\text{BrSr}}{\text{Gc}} T^* \frac{\partial p^*}{\partial t^*} + \frac{\text{Br}}{\text{Gc}} T^* \mathbf{u}^* \cdot \nabla p^*. \end{aligned} \quad (2.33)$$

For typical injection molding parts ( $\epsilon \lll 1$ ), the dimensionless numbers used in Equation (2.33) are:

$$\text{Fo} = \frac{\lambda_0 \tau}{\rho_0 c_{p0} L^2}, \quad \text{Fourier} \quad (2.34)$$

$$\text{Pe} = \frac{\rho_0 c_{p0} U L}{\lambda_0}, \quad \text{Péclet} \quad (2.35)$$

$$\text{Br} = \frac{\eta_0 U^2}{\lambda_0 (\Delta T)_0}, \quad \text{Brinkman} \quad (2.36)$$

$$\text{Sr} = \frac{L}{\tau U}, \quad \text{Strouhal} \quad (2.37)$$

$$\text{Gc} = \frac{1}{\alpha_0 (\Delta T)_0}, \quad \text{Gay-Lussac} \quad (2.38)$$

Using the characteristic values given in Table 2.1, the order of magnitude of the dimensionless groups in Equation (2.33), can be estimated:

$$\underbrace{\frac{1}{\epsilon^2 \text{Fo}} \frac{\partial T^*}{\partial t^*}}_{10^1 \tau^{-1}} + \underbrace{\epsilon \text{Pe} \mathbf{u}^* \cdot \nabla^* T^*}_{10^3} = \underbrace{2 \text{Br} \dot{\gamma}^{*2}}_{10^1} + \underbrace{\nabla^* \cdot (\lambda^* \nabla^* T^*)}_1 + \underbrace{\frac{\text{BrSr}}{\text{Gc}} T^* \frac{\partial p^*}{\partial t}}_{10^{-3} \tau^{-1}} + \underbrace{\frac{\text{Br}}{\text{Gc}} T^* \mathbf{u}^* \cdot \nabla p^*}_{10^{-3}}. \quad (2.39)$$

Regardless of the characteristic time one may choose, e.g. filling, packing, the last two terms can be dropped out from Equation (2.39). Physically, this implies that the heat generated due to compression is negligible. Hence, the energy equation can be reduced to:

$$\frac{1}{\epsilon^2 \text{Fo}} \frac{\partial T^*}{\partial t^*} + \epsilon \text{Pe} \mathbf{u}^* \cdot \nabla^* T^* = 2 \text{Br} \dot{\gamma}^{*2} + \nabla^* \cdot (\lambda^* \nabla^* T^*). \quad (2.40)$$

Introducing in Equation (2.33) the characteristic process values for air, listed in Table 2.1, the order of magnitude of the terms change. The first term becomes of order  $10^2 \tau^{-1}$ , the convection term containing  $\epsilon \text{Pe}$  term is of order  $10^1$  and the Brinkman number equal to  $10^{-6}$ . Additionally we find the Brinkman number of the fictitious fluid to be of order  $10^{-2}$ . The order of magnitude of the remaining terms does not change. We can conclude that in addition to the last two terms, also the viscous dissipation term, as expected, can be neglected in the air domain. In practice however, we set the viscous dissipation term to zero in the air domain,  $c < 0.5$ , since the computed velocity field, based on fictitious fluid properties, is not representative of the actual air velocity field.

### 2.1.3 Front-capturing technique

In order to track the polymer/air and polymer/gas interfaces we use a front-capturing technique, also known as *pseudo concentration method*, which was proposed by Thompson [117]. Each material point, or infinitesimal material volume element, is labeled with a scalar  $c$ , and the material labels for polymer, air and gas core are convected with the velocity  $\mathbf{u}$  throughout the domain. Boundary conditions are made dependent on  $c$ . The method requires the addition of a pure (passive scalar) convection equation that gives the evolution of the material label distribution:

$$\frac{\partial c}{\partial t} + \mathbf{u} \cdot \nabla c = 0. \quad (2.41)$$

As initial condition the material labels are set to zero over the entire domain  $\Omega$ , and at the inlet the following boundary conditions are assigned:

$$c(\mathbf{x}, t = 0) = 0, \quad \mathbf{x} \in \Omega, \quad (2.42)$$

$$c(\mathbf{x}, 0 < t < t_{\text{fill}}) = 1, \quad \mathbf{x} \in \Gamma_e. \quad (2.43)$$

The interface is captured for  $c$  equal to 0.5. The material properties are made dependent on the local value of the concentration,  $c$ , and are discontinuous across the interfaces polymer-air and polymer-gas. For the air or gas phase,  $c < 0.5$ , the fictitious-fluid properties are assigned, while for the case  $c \geq 0.5$  the polymer properties are chosen. We also perform particle tracking, using Equation (2.41), but instead of prescribing at the inlet boundary a concentration value  $c$ , we prescribe a time label,  $t$ , convecting basically the flow history.

### 2.1.4 Boundary conditions

#### Flow problem

Assuming a computational domain  $\Omega$ , Figure 2.1, boundary conditions are specified at  $\Gamma_e$ ,  $\Gamma_w$  and  $\Gamma_v$ , designating the mold entrance, mold walls, and the air vents, respectively.

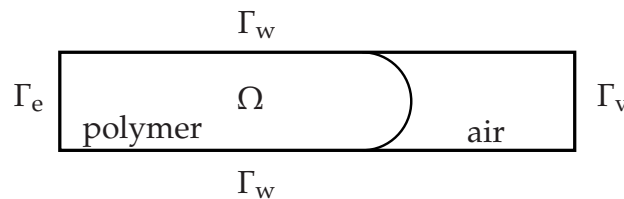


Figure 2.1: Computational domain.



In industry, the injection molding conditions used often employ a dynamic filling phase in which pressure continuously changes to assure a certain prescribed injection speed. Instead, during the subsequent packing and holding phases, pressure is prescribed. Accordingly, we prescribe a volume flow rate while filling the mold cavity, by means of a fully-developed velocity profile, and an imposed pressure (i.e. normal stress) during the packing and holding stages. At the mold walls we use adjustable Robin boundary conditions that allow the change from slip to no-slip depending on the material label  $c$  at the wall. If air touches the wall,  $c = 0$ , a slip boundary condition is assigned, if instead polymer is,  $c \geq 0.5$ , a no-slip condition is imposed by setting a traction force at the wall. Accordingly, the boundary condition for the velocity and stress components  $u_t$  and  $\sigma_t$  in tangential direction read:

$$au_t + \sigma_t = 0 \quad \forall \mathbf{x} \in (\Gamma_w \cup \Gamma_v), \quad (2.44)$$

in which the dimensionless ‘Robin penalty parameter’  $a$  is defined as

$$a = a(c) = \begin{cases} \geq 10^6 & \text{if } c \geq 0.5: \text{ no slip or leakage} \\ 0 & \text{if } c < 0.5: \text{ slip or leakage} \end{cases}$$

Air is only allowed to exit the cavity at air vents,  $\Gamma_v$ . For this a Robin condition is assigned for the velocity and stress components  $u_n$  and  $\sigma_n$  in normal direction:

$$u_n = 0 \quad \forall \mathbf{x} \in \Gamma_w \quad (2.45)$$

$$au_n + \sigma_n = 0 \quad \forall \mathbf{x} \in (\Gamma_w \cup \Gamma_v), \quad (2.46)$$

in which  $a$  is again given by Equation (2.45). However, in this case the term ‘slip’ should be replaced by ‘leakage’.

### Temperature problem

An initial temperature field is prescribed over the entire domain corresponding to the air/fictitious fluid phase,

$$T_i = T_0(\mathbf{x}, t = 0) \quad \mathbf{x} \in \Omega. \quad (2.47)$$

At the injection gate  $\Gamma_e$  the injection temperature is prescribed,

$$T = T_e(\mathbf{x}, t) \quad \in \Gamma_e, t > 0. \quad (2.48)$$

For the mold walls, either a Dirichlet boundary condition or a mixed boundary condition can be prescribed,

$$T = T_w(\mathbf{x}, t = 0, t) \quad \mathbf{x} \in \Gamma_w \cup \Gamma_v, t \geq 0, \quad (2.49)$$

or

$$k \frac{\partial T}{\partial n} = h(T - T_\infty), \quad (2.50)$$

respectively, in which  $h$  is the heat transfer coefficient.

## 2.2 Numerical methods

We use a finite element solution algorithm to solve the flow and heat transfer problems in 3-D, early developed in our group by Haagh and Van de Vosse [31]. The Stokes and energy equation are coupled but solved within each time step in a segregated manner. The Stokes equations, Equation (2.1) and Equation (2.22), that compose the flow problem are solved by a velocity-pressure formulation that is discretized by a standard Galerkin finite element method (GFEM). Since during the filling phase the flow is incompressible, and in the subsequent phases (packing and holding) compressible, two different weak forms are found after performing the Galerkin finite element discretization. The system of equations is solved in an integrated manner, both velocity and pressure are treated as unknowns. In case of 2-D computations the discretized set of algebraic equations is solved using a direct method based on sparse multifrontal variant of Gaussian elimination (HSL/MA41) - direct solver (HSL), for details the reader is referred to [2–4]. In 3-D computations the resulting system of linear equations consists of generally large sparse matrices, and often iterative solvers are employed which use successive approximations to obtain a convergent solution. Furthermore, they avoid excessive CPU time and memory usage. In our 3-D computations we use a generalized minimal residual solver (GMRES) [93], in conjunction with an incomplete LU decomposition preconditioner. The computational domain is discretized with elements with discontinuous pressure of the type Crouzeix-Raviart -  $Q_2P_1^d$ , 2-D quadrilateral or brick 3-D finite elements, in which the velocity is approximated by a continuous piecewise polynomial of the second degree, and the pressure by a discontinuous complete piecewise polynomial of the first degree. The degrees of freedom at the nodal points correspond to the velocity components while at the central node the pressure and pressure gradients are computed. The integration on the element is performed using a 9-point (2-D) or 27-point (3-D) Gauss rule.

Special care has to be given to solve the front-capturing convection equation. Convection dominated problems give rise to unstable solutions with spurious

node-to-node oscillations, referred to as wiggles. To overcome this problem the Streamline-Upwind Petrov-Galerkin (SUPG) method, proposed by Brooks and Huges [11], is the most employed and thus adopted in our model.

## 2.3 FEM formulation for the injection problem

We use a finite element solution algorithm to solve the flow and heat transfer problem in 3-D earlier developed in our group [31]. The Stokes and energy equation are solved in a segregated manner.

### 2.3.1 Flow problem

The continuity and Stokes equations, Equation (2.1) and Equation (2.22), that compose the flow problem are solved by a velocity-pressure formulation that is discretized by a standard Galerkin finite element method (GFEM). Since during the filling phase the flow is incompressible and in the subsequent stages (packing and holding) compressible, two different weak forms after performing the Galerkin finite element discretization:

#### Filling stage

$$\int_{\Omega} 2\eta \mathbf{D}(\mathbf{u}) : \mathbf{D}(\mathbf{v}) d\Omega - \int_{\Omega} p(\nabla \cdot \mathbf{v}) d\Omega + \int_{\Omega} (\nabla \cdot \mathbf{u}) q d\Omega = \int_{\Gamma} \mathbf{t} \cdot \mathbf{v} d\Gamma, \quad (2.51)$$

in which  $q, \mathbf{v}$  denote the weighting functions for pressure and velocity, respectively. The traction force,  $\mathbf{t}$ , is defined as:

$$\mathbf{t} = 2\eta \mathbf{D}(\mathbf{u}) \cdot \mathbf{n} - p \mathbf{n} \quad \text{on} \quad \partial\Omega. \quad (2.52)$$

After applying the spatial discretization, the equations written in matrix form read,

$$\begin{bmatrix} \mathbf{S} & \mathbf{L}^T \\ \mathbf{L} & \mathbf{0} \end{bmatrix} \begin{Bmatrix} \mathbf{u}^h \\ \mathbf{p}^h \end{Bmatrix} = \begin{Bmatrix} \mathbf{f} \\ \mathbf{0} \end{Bmatrix}, \quad (2.53)$$

in which  $[\mathbf{S}]$  is the stiffness matrix,  $[\mathbf{L}]$  represents the discretized operator  $-\nabla$  and  $\{\mathbf{f}\}$  is the right hand side vector containing the essential boundary conditions and traction forces. The discretized velocity and pressure are given by  $\mathbf{u}^h$  and  $\mathbf{p}^h$ , respectively. In a matrix form the weak form leads to:

$$\mathbf{L}_{ij} = \int_{\Omega} \psi_i \nabla(\phi_j) d\Omega, \quad (2.54)$$

$$\mathbf{S}_{ij} = \int_{\Omega} \eta \left[ (\nabla\phi \cdot \nabla\phi^T) \mathbf{I} + (\nabla\phi \nabla\phi^T)^c \right] d\Omega, \quad \text{where } \mathbf{A}^c \equiv \mathbf{A}^T, \quad (2.55)$$

where  $\phi_i$  and  $\psi_i$  are the shape functions for the velocity and pressure respectively.

### Packing and holding stages

To take into account compressibility the original form of the continuity equations, Equation (2.1), has to be discretized. The weak form of the flow problem becomes:

$$\int_{\Omega} 2\eta \mathbf{D}(\mathbf{u}) : \mathbf{D}(\mathbf{v}) d\Omega - \int_{\Omega} p(\nabla \cdot \mathbf{v}) d\Omega + \int_{\Omega} (\nabla \cdot \mathbf{u}) q d\Omega = \int_{\Gamma} \mathbf{t} \cdot \mathbf{v} d\Gamma + \int_{\Omega} g q d\Omega, \quad (2.56)$$

in which  $g$  contains the right hand side of the continuity equation, more specifically the time derivative of density. After applying the spatial discretization, the equations written in matrix form read,

$$\begin{bmatrix} \mathbf{S} & -\mathbf{K} \\ -\mathbf{L} & 0 \end{bmatrix} \begin{Bmatrix} \mathbf{u}^h \\ \mathbf{p}^h \end{Bmatrix} = \begin{Bmatrix} \mathbf{f} \\ \mathbf{g} \end{Bmatrix}, \quad (2.57)$$

with  $\mathbf{K}$  defined as:

$$K_{ij} = \int_{\Omega} \psi_i \nabla(\rho \phi_j) d\Omega. \quad (2.58)$$

The right hand side vector  $\mathbf{g}$  contains a partial derivative of the density in the following manner: let us consider the continuity equation, for a single element it reads:

$$K_{ij}^e u_j^i = g_i^e \quad \text{for } i = 1, \dots, m^e \text{ and } j = 1, \dots, n^e, \quad (2.59)$$

in which  $n^e$  and  $m^e$  are the number of degrees of freedom per elements for the velocity and pressure gradient, respectively. Suppose that  $i = 1$  corresponds to the pressure unknown, and  $i = 2, \dots, m^e$  to the pressure gradient unknowns. Then  $\mathbf{g}^e = [g_1^e \dots g_m^e]^T$  is given by:

$$g_i^e = \begin{cases} - \int_e \psi_i \frac{\rho^n - \rho^{n-1}}{\Delta t} de & \text{for } i = 1 \\ 0 & \text{for } i = 2, \dots, m^e \end{cases}$$

in which the superscripts  $n$  and  $n-1$  denote subsequent time levels. Thus, the time derivative of density,  $\frac{\partial \rho}{\partial t}$ , is taken into account by a first order approximation in time, and a piece-wise constant approximation in space.

### 2.3.2 Convection equation

It is well known that the standard GFEM method in convection dominated problems, i.e. high Péclet number, gives rise to unstable solutions with spurious node-to-node

oscillations referred to as wiggles. To overcome this problem many researchers focused on developing the so called up-winding methods. Among all, the Streamline-Upwind Petrov-Galerkin (SUPG), [11], has been the most employed. In this method a streamline upwind function  $\pi$  is added to the continuous weighting function  $\phi$  used in the GFEM formulation, yielding a modified weighting function. As a consequence the weighting function is no longer in the same space as the approximate solution and the matrix is no longer symmetric as it would be in a Galerkin formulation. The modified weighting function  $\tilde{\phi}$  is given by:

$$\tilde{\phi} = \phi + \pi, \quad (2.60)$$

in which  $\pi$  is generally of the form:

$$\pi = k\mathbf{u} \cdot \nabla\phi. \quad (2.61)$$

Different functions can be specified for  $k$ , however for time-dependent problems in [98] the following expression suggested:

$$\pi = \left( \left( \frac{2}{\Delta t} \right)^2 + \left( \frac{2\|\mathbf{u}\|}{h} \right)^2 + \left( \frac{4\zeta}{h} \right)^2 \right)^{-\frac{1}{2}} \mathbf{u} \cdot \nabla\phi, \quad (2.62)$$

with  $h$  being the width of the element in the direction of the flow,  $\Delta t$  the computational step size and  $\phi$  the shape function. The parameter  $\zeta$  is defined as:

$$\zeta = \underline{u}^c \lambda \underline{u}, \quad (2.63)$$

where  $\lambda$  is a diffusion tensor (which is a null tensor in case of pure convection case). The weak form of the convection equation reads:

$$\int_{\Omega} \frac{\partial c}{\partial t} \tilde{\phi} d\Omega + \int_{\Omega} (\mathbf{u} \cdot \nabla c) \tilde{\phi} d\Omega = 0, \quad (2.64)$$

in which  $\phi$  is the weight function. After spacial discretization, the equation reads:

$$[\mathbf{M}]\{\dot{c}\} + [\mathbf{N}(\mathbf{u})]\{c\} = \{0\}, \quad (2.65)$$

in which the matrix  $[\mathbf{M}]$  and the convection matrix  $[\mathbf{N}(\mathbf{u})]$  have the following finite element formulation:

$$M_{ij} = \int_{\Omega} \tilde{\phi}_i \phi_j d\Omega, \quad (2.66)$$

$$N_{ij}(\mathbf{u}) = \int_{\Omega} \tilde{\phi}_i \mathbf{u}^h \cdot \nabla \phi_j d\Omega. \quad (2.67)$$

We use the theta method to perform the time discretization of the convection equation, Equation (2.41), which reads:

$$[\mathbf{M}]\left\{\frac{c^{n+1} - c^n}{\Delta t}\right\} + \theta[\mathbf{N}(\mathbf{u}^{n+1})]\{c^{n+1}\} + (1 - \theta)[\mathbf{N}(\mathbf{u}^n)]\{c^n\} = \{0\}. \quad (2.68)$$

The subscripts  $n + 1$  and  $n$  indicate consecutive time steps. The above formulation can be approached by a two-step procedure which yields a set of equations that can be solved more efficiently:

$$\left(\frac{[\mathbf{M}]}{\theta\Delta t} + [\mathbf{N}(\mathbf{u}^{n+\theta})]\right) \{c^{n+\theta}\} = \frac{[\mathbf{M}]}{\theta\Delta t}\{c^n\} \quad (2.69)$$

$$\{c^{n+1}\} = \frac{1}{\theta} \left( \{c^{n+\theta}\} - (1 - \theta)\{c^n\} \right). \quad (2.70)$$

For  $\theta = 0$  this scheme reduces to a first order forward Euler scheme, while for  $\theta = 1$  the first order backward Euler scheme results. When  $\theta = 0.5$  the second order Crank-Nicholson scheme results. If  $0.5 < \theta < 1$  the scheme is unconditionally stable, hence for any choice of  $\Delta t$  the integration process results. In our case, following Haagh and Van de Vosse [31], we set  $\theta$  to  $0.5 + \alpha\Delta t$ , with  $\alpha$  being a small positive real number, to suppress oscillations in  $c$  without affecting the order of accuracy. At the end of each time step we round everywhere in the computational domain the material labels either to zero or unity, with the exception of those in the elements containing the interface, to suppress any oscillation in the material-label field.

### 2.3.3 Energy equation

The energy equation is a convection diffusion equation and the way to solve it with the finite element method is similar to that employed for the convection equation, in fact the convection equation is just a special case in which the diffusion coefficient is set to zero. Also for this case, to circumvent oscillations in the temperature field, the SUPG method is applied. The weak form and the spacial discretization are given below:

$$\int_{\Omega} \frac{\partial T}{\partial t} \tilde{\phi} d\Omega + \int_{\Omega} (\mathbf{u} \cdot \nabla T) \tilde{\phi} d\Omega, + \int_{\Omega} \alpha \nabla T \nabla \tilde{\phi} d\Omega = 0, \quad (2.71)$$

$$[\mathbf{M}]\{\dot{T}\} + [\mathbf{N}(\mathbf{u})]\{T\} + \mathbf{D}\{T\} = \{f\}. \quad (2.72)$$

The matrix  $[\mathbf{M}]$ , the convection matrix  $[\mathbf{N}(\mathbf{u})]$ , the diffusion matrix  $[\mathbf{D}]$  and the right-hand side vector  $\{f\}$  have the following finite element formulation:

$$M_{ij} = \int_{\Omega} \rho c_p \tilde{\phi}_i \phi_j d\Omega, \quad (2.73)$$

$$N_{ij}(\mathbf{u}) = - \int_{\Omega} \rho c_p (u^h \cdot \nabla \tilde{\phi}_i) \phi_j d\Omega, \quad (2.74)$$

$$D_{ij} = \int_{\Omega} \lambda \nabla \tilde{\phi}_i \cdot \nabla \phi_j d\Omega, \quad (2.75)$$

$$f = 2 \int_{\Omega} \tilde{\phi}_i \mathbf{D}^d : \mathbf{D}^d d\Omega. \quad (2.76)$$

$$(2.77)$$

The time discretization of the energy equation followed the same scheme adopted for the convection equation.

## 2.4 Conclusions

The set of equations necessary to model all phases of the injection molding process with gas-injection in full 3-D have been derived, applied and simplified based on scaling arguments. Their numerical solution has been discussed. Now we are ready and equipped to start to derive frozen-in orientation and stresses.

## CHAPTER THREE

# Flow-induced stresses in gas-assisted injection molding

---

### Abstract

The development of flow-induced stresses in gas-assisted injection molding (GAIM) is investigated. A 3-D finite element model for injection molding that employs a front-capturing technique is used. The model captures the kinematics of the flow front and is able to describe the gas bubble shape and to predict the thickness of the residual layer. For the computation of flow-induced stresses a decoupled approach is adopted, in which elastic effects are neglected in the momentum balance. In a staggered procedure, the computed flow kinematics are plugged into a non-linear viscoelastic equation from which flow-induced stresses are computed. The Rolie-Poly equation is chosen given its outstanding capacity to describe the rheology of polymers under shear and elongation flows. A 2-D approximated injection molding case is chosen, in which polycarbonate (PC) is injection molded into a rectangular cavity. In order to establish a clear comparison, flow-induced stresses are computed for the same geometry using standard injection molding and GAIM. The impact of GAIM on flow-induced stresses is impressive, since computed stress profiles show a substantial decrease in stress magnitudes. Therefore a substantial decrease in anisotropy of physical properties is expected in GAIM parts.

### 3.1 Introduction

Gas-assisted injection molding, GAIM, was originally developed as a technology to produce parts with hollow sections, structural ribs, bosses or parts with regions with



significant changes in thickness. When parts with such geometrical features are processed via conventional injection molding, items with poor surface quality and an unpredictable final shape result. This is due to the process incapacity to compensate for the large polymer shrinkage inside the mold. GAIM is mostly used because it improves products' dimensional stability and surface quality, as well as it increases production efficiency. More specifically, it reduces the part's weight and the cycle time, injection pressure and clamping force. Moreover, the development of surface defects, the so-called sink marks, is inhibited as a consequence of the reduced shrinkage. The process involves the following subsequent steps: first polymer melt is injected until the mold cavity becomes partly filled. Next, (or during the polymer injection) gas is injected into the mold, pushing the polymer melt until all the cavity walls become wetted by a polymer film. In the end, the gas is vented and the part cooled and ejected. The gas injection stage consists of a first gas penetration, in which the cavity walls are wetted by the polymer melt, and a secondary penetration in which gas, under pressure control, holds the polymer under pressure to compensate for shrinkage.

Additional processing parameters have to be taken into account in GAIM, namely the delay time between melt and gas injection, the shot weight i.e. amount of polymer melt injected and the gas pressure. The combination of these parameters with the conventional injection molding parameters, e.g. injection speed, mold temperature, is far from trivial, making of GAIM a cumbersome process to optimize. Typically, when optimizing the production of gas-assisted injection molded parts one aims to control the gas penetration length and the thickness of the residual layer of solidified polymer (polymer film). Additionally, one tries to avoid typical GAIM defects, the so-called fingering effects, that are associated with high gas pressure, and are responsible for the penetration of gas inside the polymer residual layer.

To address these experimental difficulties, and avoid costly trial and error experiments, significant research was devoted to model GAIM. Most of the models that were developed are based on the so-called 2.5-D formulation, Chen et al. [13], Li et al. [72], in which the pressure field is solved with finite elements in 2-D and the temperature and velocity fields with finite differences in 3-D. However, to properly model GAIM this approach poses serious limitations, since it is limited to thin-walled and weakly curved geometries which are not representative for most of the parts processed via GAIM. Also, as pointed out by Khayat et al. [63], for thin walled parts the shape of the gas/melt front exhibits a severe curvature as opposed to that of the melt front, due to the decrease of the cross sectional height caused by previous solidification of polymer melt at the mold walls. This curvature cannot be captured by models using the Hele-Shaw formulation and hence the shape of the gas bubble and the residual wall thickness cannot be accurately predicted. These limitations, along with the exceptional increase in computing power, have motivated the extension of GAIM models from a 2.5-D frame to a full 3-D approach, Haagh and Van de Vosse [31], Ilinca and Héту [48], Johnson et al. [54], Khayat et al. [63], Polynkin et al. [91]. In [31] a full 3-D GAIM finite-element model was proposed. The authors used a pseudo concentration method to capture the polymer front and gas/melt interface. Model predictions for a non-Newtonian fluid under isothermal and non-isothermal condi-

tions were presented for different geometries and compared to experimental results. For isothermal conditions the computational results match the experimental ones, however for non-isothermal conditions the results deviated, which was attributed to lack of experimental control. In [54] the authors also used a pseudo-concentration method to simulate GAIM, but focused on isothermal flow conditions. Also in [91] a full 3-D model in combination with a pseudo-concentration method was used to simulate GAIM, however the authors chose a part with a complex geometry and gave particular emphasis on the importance of prescribing thermal boundary conditions that mimic the ones present inside the mold cavity. For that, they have introduced a special type of Biot boundary conditions which make use of an adaptive heat transfer coefficient that is made dependent on both time and position.

Until nowadays the numerical studies reported on GAIM, Johnson et al. [54], Li et al. [73], Parvez et al. [89], Polynkin et al. [91], have mainly focused on the prediction of the gas bubble shape and thickness of the residual polymer layer as a function of process variables i.e. shot weight, gas pressure, etc. In [54] the authors compared the predicted residual wall thickness with experiments, using a 2-D and a 3-D model. Additionally, they performed tensile testing on specimens obtained under the conventional technology and via GAIM, and measured a higher tensile modulus for the specimens processed by conventional injection molding. Dimakopoulos and Tsamopoulos [19], analyzed the effects of the fluid's compressibility, inertia, contact conditions at the walls, and the initial amount of liquid, for the GAIM of fluids partially occupying straight or complex tubes. However, there has not been yet a study devoted to the computation of residual stresses in gas-assisted injection molded parts. Since one of the advantages of GAIM is the decrease in amount of residual stresses and, hence, an improvement in the dimensional stability, such computations are of utmost importance to support this.

Residual stresses in injection molding are responsible for the dimensional stability of molded parts and the anisotropy of their properties, i.e. mechanical and optical. There are mainly two sources of residual stresses, Baaijens [8], Meijer [83]. The first, flow-induced stresses, are viscoelastic in nature and originate from the resistance of molecules to attain a preferential alignment with the flow direction (entropy driven). The second, the so-called thermally and pressure-induced stresses, originate from differential shrinkage induced by the combined effect of inhomogeneous cooling and pressure.

Upon processing, polymer molecules in the melt become aligned within flow direction, attaining a degree of orientation that is dependent on the strain rate and on the relaxation times of individual molecules. However, once molecules become orientated, stresses in the fluid start to develop, a phenomena usually depicted by an increase of the first normal stress difference. Such stress development is related to the decrease in entropy of the molecules. When flow is applied, molecules can no longer adopt a conformation that maximizes their entropy, the so-called random coil conformation, and as a consequence entropic stresses are originated. Frozen-in flow-induced stresses are known to dictate the long-term dimensional stability of injection

molded parts. Throughout the life time of a molded part, relaxation processes that yield shrinkage take place as oriented molecules strive to reach for more favorable conformations. However, since the molecule's relaxation time becomes extremely high upon cooling through the glass transition temperature,  $T_g$ , typically such processes take place over long times. As it was shown by Caspers [12] the resulting shrinkage depends on the molecular orientation, being higher in the flow direction. Additionally to this, as was pointed out by Struik [114], flow-induced stresses also affect the thermal expansivity of polymers below  $T_g$ , as they result in a negative contribution to the reversible coefficient of thermal expansion. Furthermore, frozen-in orientation also introduces anisotropy of physical properties, e.g. mechanical, optical and thermal.

It has been reported by Baaijens [8], Douven [22], Kamal et al. [58], Zoetelief et al. [134] that the magnitude of flow-induced stresses is about one to two orders lower than the magnitude of thermally and pressure induced stresses. However, Wimberger-Friedl et al. [132] show, by comparing polystyrene (PS) with polycarbonate (PC), that the ratio between these two contributions to the final residual stresses depends on the polymer. Notably, for PS the magnitude of flow-induced stresses is much higher than for PC injection-molded parts. Such a difference is explained on the basis of the lower molecular weight and lower relaxation times of PC chains. As chains are more flexible and their relaxation mechanisms faster, they become harder to orient with the flow. However, the contribution of thermally and pressure induced stresses is supposed to be higher for PC instead, since these stresses scale with the material modulus. The authors conclude that the birefringence in injection molded PC parts results from both contributions, equal in magnitude, of flow-induced stresses and of residual stresses.

In this work we propose a method for the computation of flow-induced stresses in GAIM. We extend the finite element 3-D model developed by Haagh and Van de Vosse [31] for GAIM and follow a decoupled approach in which the velocity-pressure problem is solved independently from the stress problem. Hence, at every computational time step we compute the flow kinematics assuming a generalized Newtonian fluid behavior, and plug them into a viscoelastic model to compute residual stresses. Such a staggered-scheme approach was validated in Baaijens [8], where it was shown that minor differences in terms of normal stresses result, compared to employing a viscoelastic constitutive model in the momentum equation. The decoupled approach gathers the advantages of saving a tremendous amount of computing effort and avoiding flow instabilities that arise at high Weissenberg numbers, see Hulsen et al. [44], which are typical for the injection molding flow conditions. The study of such instabilities is beyond the scope of this thesis.

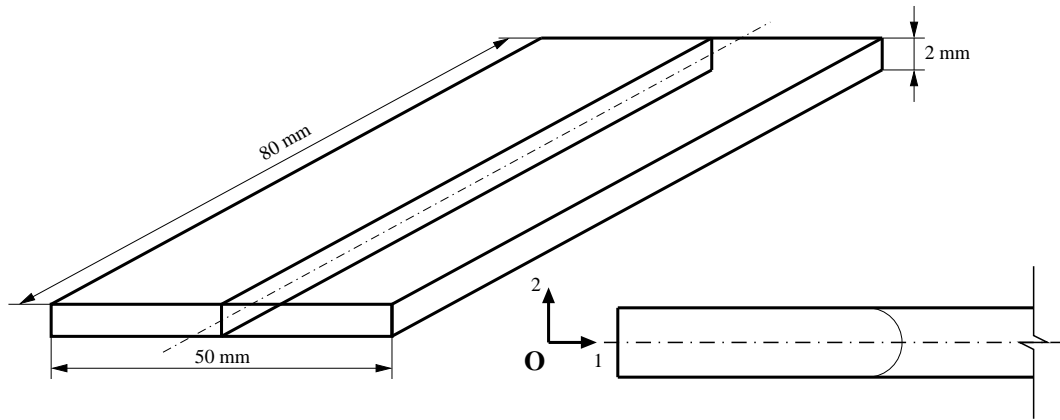


Figure 3.1: Sketch of the cavity geometry.

## 3.2 Problem definition

To evaluate the development of flow-induced stresses in gas-assisted injection molding parts, we depart from an earlier study, done by Baaijens [8], in which flow-induced stresses were computed for PC plates injection molded via the standard injection technology. Baaijens used an Hele-Shaw formulation to predict the flow kinematics and used the Leonov model to compute viscoelastic flow-induced stresses. In our study we apply a fully 3-D model to the same injection problem, i.e. geometry, material and processing conditions, to study the development of flow-induced stresses when using conventional or gas-assisted injection molding. Significant differences are obviously expected when using a fully 3-D based approach without the Hele-Shaw assumptions which are: constant pressure across the mold thickness, negligible velocity in the thickness direction, small velocity gradients and negligible thermal conduction parallel to the mid plane. Moreover, since we capture the fountain flow, the melt stretched at the flow front region is expected to contribute to the final flow-induced stress profiles. In order to properly describe the elongation happening at the flow front we use the Rolie-Poly-model, see Likhtman and Graham [76], due to its known capacity to accurately describe the rheology of linear polymers in both shear and extensional flows.

To make the problem computationally cheaper and to be able to compare results with standard 2.5-D analysis, we investigate a 2-D problem, taking a cross section of the original 3-D geometry of 80x2 mm (length, height), see Figure 3.1. The gate is located at the channel entrance.

### 3.3 Flow-induced stresses

The total Cauchy stress tensor is the sum of an elastic and a viscous part:  $\boldsymbol{\sigma} = \boldsymbol{\sigma}_e + \boldsymbol{\sigma}_v$ . The elastic part is split into a hydrostatic part and a deviatoric part Equation (3.1). For a proper description of the polymer rheology, i.e. accurate residual stress predictions, a discrete number of relaxation times and their corresponding moduli are required, see Douven [22]. From stress-relaxation rheology measurements,  $G(t)$ , the relaxation modulus, is fitted over time, in what is usually designated as a Maxwell fit, see Macosko [78]. Using a multi-mode description, to properly describe the rheological behavior of the polymer, the deviatoric part of the elastic extra stress tensor is given by Equation (3.2):

$$\boldsymbol{\sigma} = -p\mathbf{I} + \boldsymbol{\tau} + \boldsymbol{\sigma}_v, \quad (3.1)$$

$$\boldsymbol{\tau} = \sum_{j=1}^m \frac{\eta_j}{\tau_j} \bar{\mathbf{B}}_{ej}^d. \quad (3.2)$$

#### 3.3.1 Choice of the viscoelastic model

Though in injection molding the flow is shear dominated, in the flow-front region the polymer melt is highly stretched due to the fountain flow. Hence, the flow generated is spatially in-homogeneous, resulting in a combination of shear and extensional contributions. In literature, results reported on the calculation of flow-induced stresses in injection molding, often neglect fountain flow by adopting a lubrication approximation that assumes negligible velocity gradients parallel to the flow direction and negligible velocities across the thickness direction. However in our model we capture the fountain flow in the overall kinematics, and thus we need a model that is able to accurately predict the rheological behavior of polymers under shear and extensional flows. Likhtman and Graham [76] presented a new model, the Rolie-Poly model, for the rheology of linear polymers. Reported results show a good agreement with rheological measurements in steady and transient regimes in both shear and elongation. The model is of the differential type, and in its single-mode form it reads:

$$\overset{\nabla}{\mathbf{B}}_e + \frac{1}{\lambda_d}(\mathbf{B}_e - \mathbf{I}) + \frac{2(1 - \sqrt{(3/\text{tr}(\mathbf{B}_e)))})}{\lambda_R} \left( \mathbf{B}_e + \beta \left( \frac{\text{tr}(\mathbf{B}_e)}{3} \right)^\delta (\mathbf{B}_e - \mathbf{I}) \right) = \mathbf{0}. \quad (3.3)$$

The molecular dynamic mechanisms taken into account in the derivation of this model, such as chain reptation, chain stretch and convective constraint release, appear in the above equation, each associated with a different term. Hence, each term of the equation addresses a specific molecular mechanism. This feature makes this model particularly physically intuitive. For higher strain rates the Rolie-Poly model, in its single mode form, produces a faster stress growth when compared to the full theory. The explanation presented by Likhtman and Graham [76], is that the full the-

ory contains a spectrum of stretch-relaxation times, reflecting different parts of the chain, where as the single mode equation assumes uniform stretch. To compensate for the overprediction of the steady-state stress at large rates, the authors advise to set  $\beta$  to 0. In the model two time scales are of importance:  $\tau_d$ , the disengagement (reptation) time, and  $\tau_R$ , the Rouse (stretching) time. The disengagement times are obtained from stress relaxation measurements, in which the relaxation modes are fitted. The Rouse time  $\tau_R$  can be estimated by the following relationship for monodispersed melts proposed by Doi and Edwards [20]:

$$\tau_R = \frac{\tau_d}{3Z}, \quad (3.4)$$

in which  $Z$ , the number of entanglements per chain, is calculated from the weigh averaged molecular weigh  $M_w$  and the averaged molar mass between entanglements  $\langle M_e \rangle$ :

$$Z = \frac{M_w}{M_e}. \quad (3.5)$$

Since compressibility is a key issue during the packing and holding phases we next introduce a compressible version of the Rolie-Poly equation, Equation (3.3). For that we adopt the approach used by Baaijens [8], who proposed a compressible version of the Leonov model. Assuming that the polymer cannot undergo a permanent plastic volume change, and that the deformation tensor  $F$  can be decomposed multiplicatively into an elastic part ( $F_e$ ) and a plastic ( $F_p$ ) part:  $F = F_e \cdot F_p$ , the determinant of the deformation tensor  $J$ , is only attributed to elastic deformation:

$$J_p = \det(F_p) = 1, \quad J_e = \det(F_e) = \det(F) = J. \quad (3.6)$$

Volumetric changes embedded in  $F_e$  can be split from the deviatoric response according with Simo [106] by the following kinematic split:

$$\bar{F}_e = J^{-1/3} F_e, \quad (3.7)$$

in which  $\bar{F}_e$  is the *volume preserving part* of the elastic part of the deformation tensor. The elastic Finger tensor ( $B_e$ ) relates to the elastic part of the deformations tensor  $F_e$  in the following manner:

$$B_e = F_e \cdot F_e^c \quad ; \quad \bar{B}_e = \bar{F}_e \cdot \bar{F}_e^c. \quad (3.8)$$

The *volume preserving part* of the elastic Finger can be obtained from  $B_e$  according to:

$$\bar{B}_e = J^{-2/3} B_e. \quad (3.9)$$

### 3.3.2 Boundary conditions

As a boundary condition for the computation of flow-induced stresses, we assume that the material injected inside the mold cavity carries no deformation history. This assumption is not consistent with the fully developed velocity profile prescribed at the inlet. However, given the high temperatures in the melt prior to injection, one can assume that any deformation history in the material is erased. Thus, the boundary condition for the stress problem reads:

$$\bar{\mathbf{B}}_e = \mathbf{I} \quad \forall \mathbf{x} \in \Gamma_e, t \geq 0. \quad (3.10)$$

### 3.3.3 Numerical integration

To perform the numerical integration of the Rolie-Poly equation, Equation (3.3), we use a second-order Adams-Bashford explicit scheme. For the first two time steps the numerical integration follows a first order *forward Euler* method. Accordingly, the time marching scheme reads:

for time step  $\leq 2$ ,

$$\bar{\mathbf{B}}_e^{n+1} \approx \bar{\mathbf{B}}_e^n + \mathbf{f}(\mathbf{u}, \bar{\mathbf{B}}_e, \nabla \mathbf{u}, (\nabla \mathbf{u})^T)|^n \Delta t, \quad (3.11)$$

for time step  $> 2$ ,

$$\bar{\mathbf{B}}_e^{n+1} \approx \bar{\mathbf{B}}_e^n + \left( \frac{3}{2} \mathbf{f}(\mathbf{u}, \bar{\mathbf{B}}_e, \nabla \mathbf{u}, (\nabla \mathbf{u})^T)|^n - \frac{1}{2} \mathbf{f}(\mathbf{u}, \bar{\mathbf{B}}_e, \nabla \mathbf{u}, (\nabla \mathbf{u})^T)|^{n-1} \right) \Delta t. \quad (3.12)$$

## 3.4 Case study

In Baaijens [8] flow-induced stresses were computed in an injection molded polycarbonate (PC) plate. In order to test our model and study the effect of GAIM on flow-induced stresses, we use the same material, processing conditions and geometry as the ones reported in [8]. We approximate the original 3-D geometry to a 2-D problem, by depicting a cross-section along the channel's length, see fig. 3.1. The gate occupies the total height of the channel.

The properties of PC are given in Table 3.1. We assume the material's viscoelastic behavior to be thermorheologically simple, implying that the relaxation times and viscosities are shifted from a reference temperature  $T_0$  to the current temperature  $T$ , by a shift factor  $a_T$ :

$$\eta_j = a_T(T) \eta_{j0}, \quad \tau_j = a_T(T) \tau_{j0}, \quad (3.13)$$

with  $\eta_{j0}$  and  $\tau_{j0}$  denoting the viscosity and relaxation time at a reference temperature,  $T_0$ . Only for  $T > T_g$  is the shift factor is determined by the WLF equation, for  $T \leq T_g$

the relaxation times become so large that we set  $T_g$  as the lower bound limit for the time temperature superposition. Hence for  $T \leq T_g$ ,  $a_T = a_T(T_g)$ . The WLF equation is given by:

$$\log a_T(T) = \frac{-C_1(T - T_0)}{C_2 + T - T_0}. \quad (3.14)$$

To estimate the Rouse time, additional information is needed, namely the weight-averaged molecular weight  $M_w$ , and the averaged molar mass between entanglements  $\langle M_e \rangle$  of PC. Since in [8] there is no specification of the material grade used, we took the value of  $M_w$  and  $M_e$  from literature. In [111], the averaged molar mass between entanglements  $\langle M_e \rangle$  of PC was determined, and a value equal to  $1.790 \text{ g mol}^{-1}$  was found. In [66] the  $M_w$  of an injection molding PC grade is given, and equals  $25.8 \text{ kg mol}^{-1}$ . Inserting these values in Equations (3.4) and (3.5), a value for the Rouse time  $\tau_R$  equal to  $2.22 \cdot 10^{-3} \text{ s}$  is found for the highest relaxation mode. For the other relaxation modes the values of the corresponding stretching relaxation times are found to be too small, and therefore irrelevant for the strain-rates involved in the process. Thus, with the exception of the highest relaxation mode, stretching can be neglected and a non-stretch form of the Rolie-Poly equation can be adopted instead:

$$\overset{\nabla}{\bar{\mathbf{B}}}_e + \frac{1}{\lambda_d}(\bar{\mathbf{B}}_e - \mathbf{I}) + \frac{2}{3}\text{tr}(\mathbf{L}\bar{\mathbf{B}}_e)(\bar{\mathbf{B}}_e + \beta(\bar{\mathbf{B}}_e - \mathbf{I})) = \mathbf{0}. \quad (3.15)$$

To describe changes in specific volume we use the so-called Tait model, see Zooler [135], which has been used vastly for amorphous polymers. The model equation reads:

$$v(p, T) = (a_0 + a_1(T - T_g)) \times \left(1 - 0.0894 \ln\left(1 + \frac{p}{B}\right)\right), \quad (3.16)$$

in which  $T_g$  is the glass transition temperature, given by  $T_g(p) = T_g(0) + sp$ , and the parameter  $B(T)$  by  $B(T) = B_0 \exp(-B_1 T)$ . The equation parameters  $a_0$ ,  $a_1$ ,  $B_0$  and  $B_1$  are different for the melt ( $T > T_g$ , indexed with  $m$ ) and the solid state ( $T < T_g$ , indexed with  $s$ ). The total set of parameters are fitted on PVT experiments that are run at quasi equilibrium conditions, under which  $v$  is measured at varying pressure and temperature. History effects are therefore not taken into account. For a detailed explanation on the model parameters the reader is referred to Zooler [135].

### 3.4.1 Processing conditions

#### Conventional case

The polymer is injected at an average velocity of  $120 \text{ mm s}^{-1}$  at  $320 \text{ }^\circ\text{C}$ . After filling,  $t_f = 0.67 \text{ s}$ , a short packing stage,  $t_p = 0.71 \text{ s}$ , follows until an injection pressure of  $50 \text{ MPa}$  is reached. This pressure is then maintained during a holding stage of  $4 \text{ s}$ . After this time the gate is assumed to freeze off instantaneously. The temperature at



**Table 3.1:** Material parameters for PC.

Parameters WLF equation:			
$T_0 = 200$	[°C]		
$C_1 = -4.217$	[-]		
$C_2 = 94.95$	[°C]		
Thermal properties:			
$c_p = 1500$	[J kg <sup>-1</sup> ]		
$\lambda = 0.27 \cdot 10^{-3}$	[J s <sup>-1</sup> mm <sup>-1</sup> K <sup>-1</sup> ]		
Viscoelastic properties:			
$\eta' = 3000\bar{\eta}$	[Pa s]		
$\tau_1 = 10^{-1}$	[s]	$\eta_1 = 9.74 \cdot 10^3$	[Pa s]
$\tau_2 = 10^{-2}$	[s]	$\eta_1 = 6.75 \cdot 10^3$	[Pa s]
$\tau_3 = 10^{-3}$	[s]	$\eta_1 = 1.25 \cdot 10^3$	[Pa s]
$M_w = 28.5$	[kg mol <sup>-1</sup> ]		
$M_e = 1.790$	[g mol <sup>-1</sup> ]		
$\tau_R = 2.22 \cdot 10^{-3}$	[s]		
Tait parameters:			
$s = 0.51 \cdot 10^6$	[°C Pa <sup>-1</sup> ]		
solid		melt	
$a_0 = 868 \cdot 10^{-6}$	$868 \cdot 10^{-6}$	$[m^3 \text{ kg}^{-1}]$	
$a_1 = 0.22 \cdot 10^{-6}$	$0.577 \cdot 10^{-6}$	$[m^3 \text{ kg}^{-1} \text{ K}^{-1}]$	
$B_0 = 395.4 \cdot 10^6$	$316.1 \cdot 10^6$	[Pa]	
$B_1 = 2.609 \cdot 10^{-3}$	$4.078 \cdot 10^{-3}$	[°C <sup>-1</sup> ]	

the mold walls is set to 80 °C. In Table 3.2 the processing conditions are summarized.

## GAIM

The conditions used for GAIM, in terms of injection temperature and speed are equal to those used in the conventional case apart from the injection time that is set to 0.44 s. The gas is injected over a limited height of the inlet (1 mm) and its injection speed is set to a value slightly higher than to that of the polymer. The gas is injected immediately after the polymer injection, thus there is no delay time between the polymer and the gas injection. The remaining processing conditions are listed in Table 3.2.

**Table 3.2:** Characteristic values of injection molding process variables for thermoplastics.

	Packing pressure [MPa]	Holding time [s]	Average velocity [ $\text{mm s}^{-1}$ ]	
			polymer	gas
Conventional	50.0	4	120	-
GAIM	0.145	2	120	130

### 3.4.2 Results & discussion

In Figure 3.2, we show first normal stress difference (N1) results, with  $N1 = \tau_{11} - \tau_{22}$ , computed in the end of the filling stage. The results obtained by Baaijens [8] are also shown.

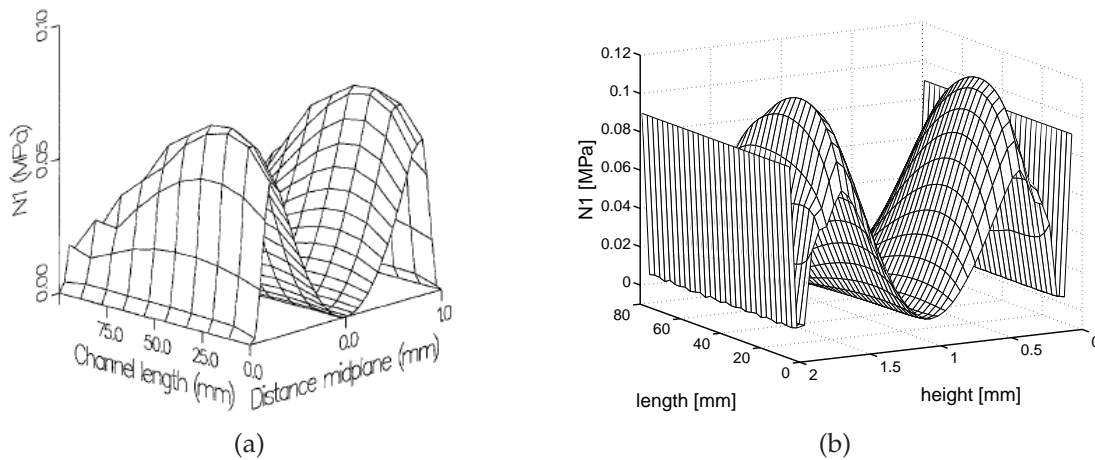


**Figure 3.2:** (a) Baaijens results [8] for N1 in the end of filling and (b) results from our simulation.

The most important difference is the high value of N1 close to the mold wall, which results from the contribution of the fountain flow. Baaijens [8] used a Hele-Shaw-based injection model that only takes into account shear contributions and, consequently, the N1 profile evidences a single peak half way in between the part mid-plane and the mold wall, where shear rates attain their maximum. Such profile is not in agreement with experimental observations, see Kamal and Tan [57], in terms of measured flow-induced birefringence, since it fails to predict the highly oriented skin layer which is believed, see e.g. Tadmor [116], to be induced by the steady elongational flow in the advancing flow front. The material that is deposited at the skin layers travels through the center region of the flow, where shear rates have their minimum, before it is stretched at the flow front and subsequently quenched at the

walls. Our model fully captures the spacious inhomogeneity of the flow field and thus, both shear and extensional components contribute to the final N1 profile. The influence of fountain flow on the flow kinematics is illustrated in Figure 3.3 where time labels are plotted.

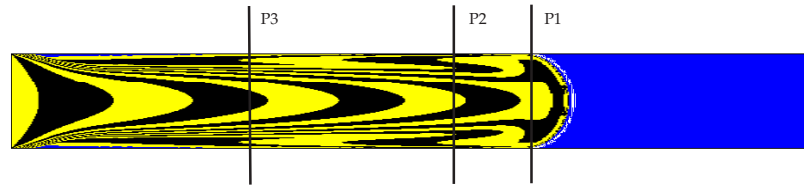


**Figure 3.3:** Plot with time labels denoting the contribution of fountain flow to the flow kinematics.

Figure 3.4 shows the first normal stress difference profiles at increasing upstream distances from the flow front. The effect of fountain flow on flow-induced stresses is depicted by a negative N1 value in the center line, resulting from the compression the material undergoes as it approaches the flow front, and large and positive N1 values close to the wall, denoting the extension of the fluid elements that are deposited in the skin layer. In regions where there is no influence of the fountain flow, here designated as fully developed-flow regions, N1 values are zero at the center line. The large stress

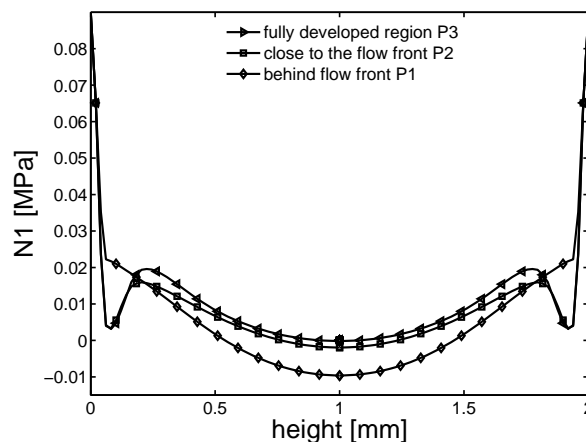


**Figure 3.4:** First normal stress difference plots across the channel height in the vicinity of the flow front and at increasing upstream distances from the flow front, positions 1, 2 and 3 according to Figure 3.3.

values at the walls result also from the contribution of the singularity at the contact point between the polymer interface and the wall. The effect of this singularity on the stress values increases upon mesh refinement, resulting on unrealistically large

stress values at the walls. Similar observations were reported by Mavridis et al. [82]. A way to exclude the effect of the contact-point singularity from the overall stress computations would be to set  $\bar{\mathbf{B}}_e = \mathbf{I} \quad \forall c < 1$ , implying that stresses could only develop behind the flow front. However, such an approach would exclude the local phenomena occurring at the flow front,  $0.5 < c < 1.0$ , and lead to zero stress values at the walls, which are not meaningful. The stress values at the walls here reported are thus only indicative, but since they qualitatively agree with the experimentally observed trends we include them in our results.

Regarding the shear-induced peaks in Figure 3.2, it can be seen that we predict higher values than Baaijens' results, although the magnitude of the stresses is similar. The fact that we solve the 3-D problem without using the Hele-Shaw assumptions will to a certain degree contribute to this effect. Though the Hele-Shaw model accurately predicts pressure fields for thin-walled parts, as it is the case of the simulation here, the temperature predicted field can be erroneous, due to the absence of the fountain flow, causing the heat convected from the core to the walls in the flow front not to be taken into account. In the case of our simulations this could cause a faster decrease in the cross-sectional height, caused by thicker solidified layer, which might be responsible for higher shear rates, therefore inducing higher values of N1. Additionally, one might expect the choice of the viscoelastic model to influence the stress results. We use a compressible version of the Rolie-Poly model instead of the compressible Leonov model employed in the study of Baaijens [8]. Figure 3.5 shows the values of N1 at different locations along the mold cavity at the end of the filling phase. It

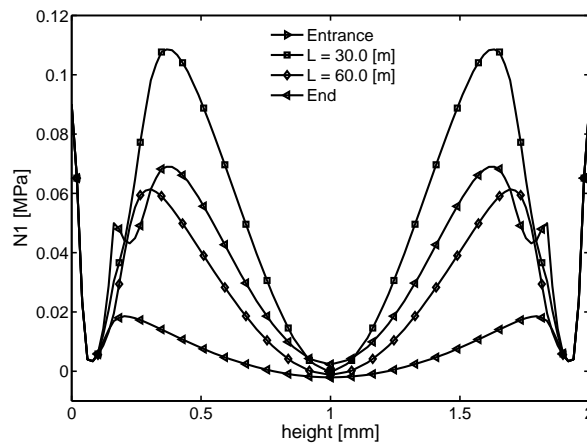


**Figure 3.5:** Normal stress difference profiles along the cavity length.

clearly shows that N1 is maximum close to the middle of the cavity and decreases to zero towards the end of the cavity, due to the small deformation history the material experiences there. Figure 3.6 shows the evolution of N1 during the total injection molding cycle. After filling the residual stresses are drastically reduced by fast relaxation of these, generally low molecular weight, polymers at the characteristic high

melt temperature, and only at the walls, where stress is frozen during filling, their value remains. Upon packing a third peak in between the shear-induced peak, developed during filling, and the center line develops. Although the strain-rates are low during packing and holding, the relaxation times increase due to cooling. They are clearly responsible for the development of significant orientation in these phases of the process, since a prerequisite for molecular orientation is sufficient strain rate:  $\dot{\epsilon} > 1/(\tau(T, M_w))$ , with  $\tau(T, M_w)$  the temperature and molecular weight dependent relaxation time, and sufficient strain  $\epsilon = \dot{\epsilon}t \gg 1$ .

### Gas-assisted injection molding

Figure 3.7 shows the evolution of N1 during the GAIM cycle. The transition from polymer filling to gas filling is marked by a sudden decrease in N1. The transition is illustrated in Figure 3.8 where normal stress differences are plotted over the height of the channel for different times at a position close to the gate corresponding to  $x_1 = 0.02$  m. At  $t = 0.42$  s gas is injected and between  $t = 0.52$  s and  $t = 0.58$  s the gas front passes through  $x_1 = 0.02$  m. Since the gas is only injected through the core of the part, significant relaxation occurs in the region of the shear-induced peaks. Only the molten material located in the core region is displaced. Thus, the deformation rates are drastically decreased and since temperatures are still well above the glass transition temperature the flow-induced stresses are allowed to relax until a new N1 profile is achieved, see Figure 3.8(a) for  $t = 0.58$  s. Nevertheless, at the flow front deformation of the material takes place as the molten polymer is pushed forward by the gas pressure. This is shown in Figure 3.8(b), in which normal stress differences, plotted in the end of the polymer filling phase for different positions along the cavity length, close to the mold wall remain unchanged throughout the channel. When compared with the N1 results obtained with conventional injection molding, Figure 3.5, there is an impressive reduction in flow-induced stresses. It can be seen that the height and width of the shear-induced peaks is significantly decreased by gas injection. Moreover, the packing and holding stages do not induce further orientation. This is due to the lower pressure level inside the cavity (and the fact that no further material is pushed into the cavity). Since the gas is able to exert pressure everywhere inside the cavity, the pressure level needed is lower (in this example two orders of magnitude) than in the conventional case. As a consequence, in GAIM, the resulting frozen-in orientation and related flow-induced stresses are solely determined during the filling stage.

## 3.5 Conclusions

A numerical study to assess the effect of GAIM on the evolution of flow-induced stresses was conducted. A compressible-version of the Rolie-Poly model was proposed and applied for the computation of flow-induced stresses. Computational results show a significant decrease in the stress magnitude during the gas filling stage.

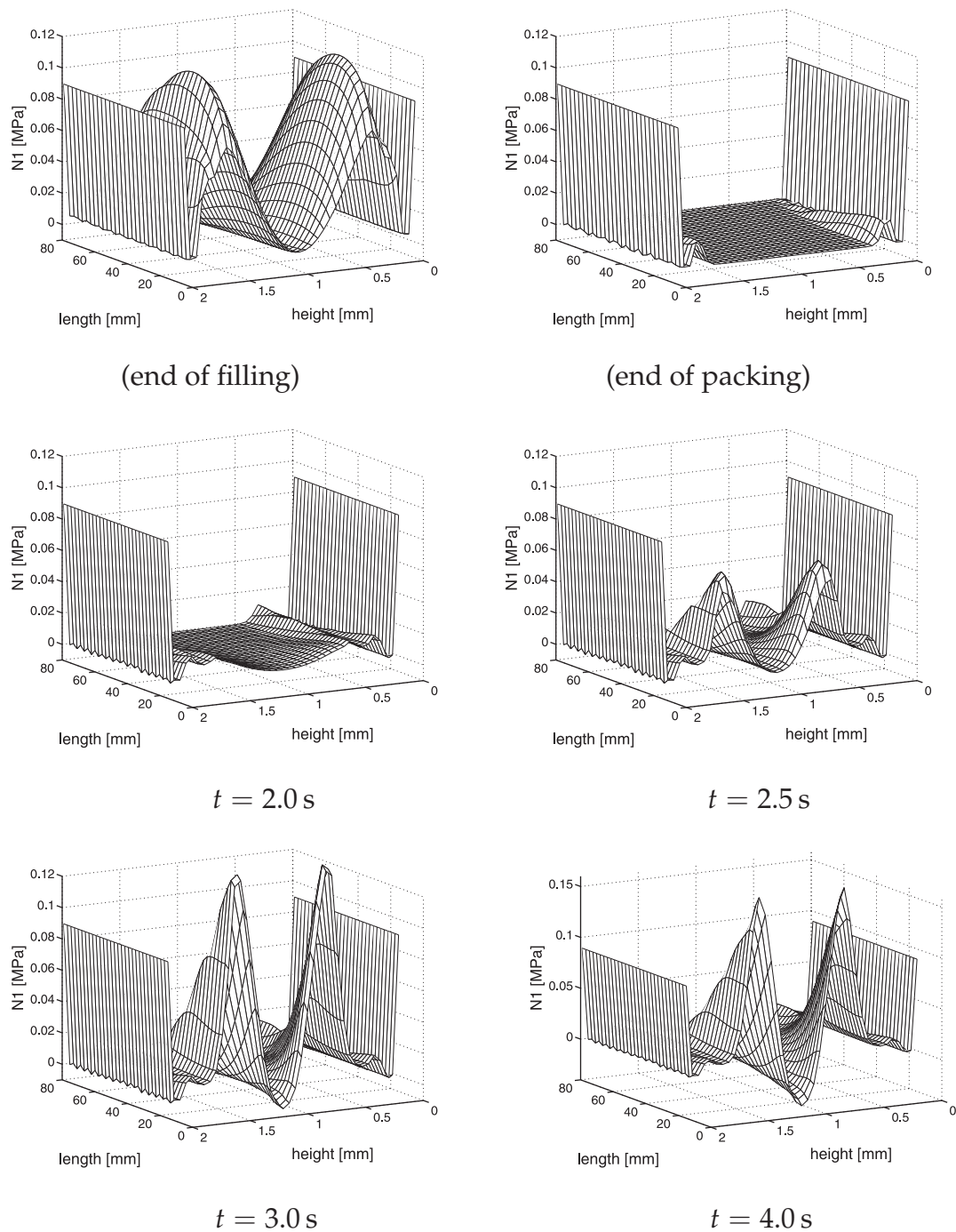


**Figure 3.6:** Time evolution of  $N_1$  in the convention injection molding case.

Furthermore, it was found that the stress level did not evolve during the packing and holding stages. Hence, flow-induced orientation and related stresses in GAIM are mostly dictated by the filling stage. Our study supports that GAIM has a strong effect on the behavior of injection molding parts and their properties. More specifically, by reducing the level of frozen-in orientation, it can minimize the part's long-term dimensional changes and the anisotropy in physical properties. Analyzes to assess the

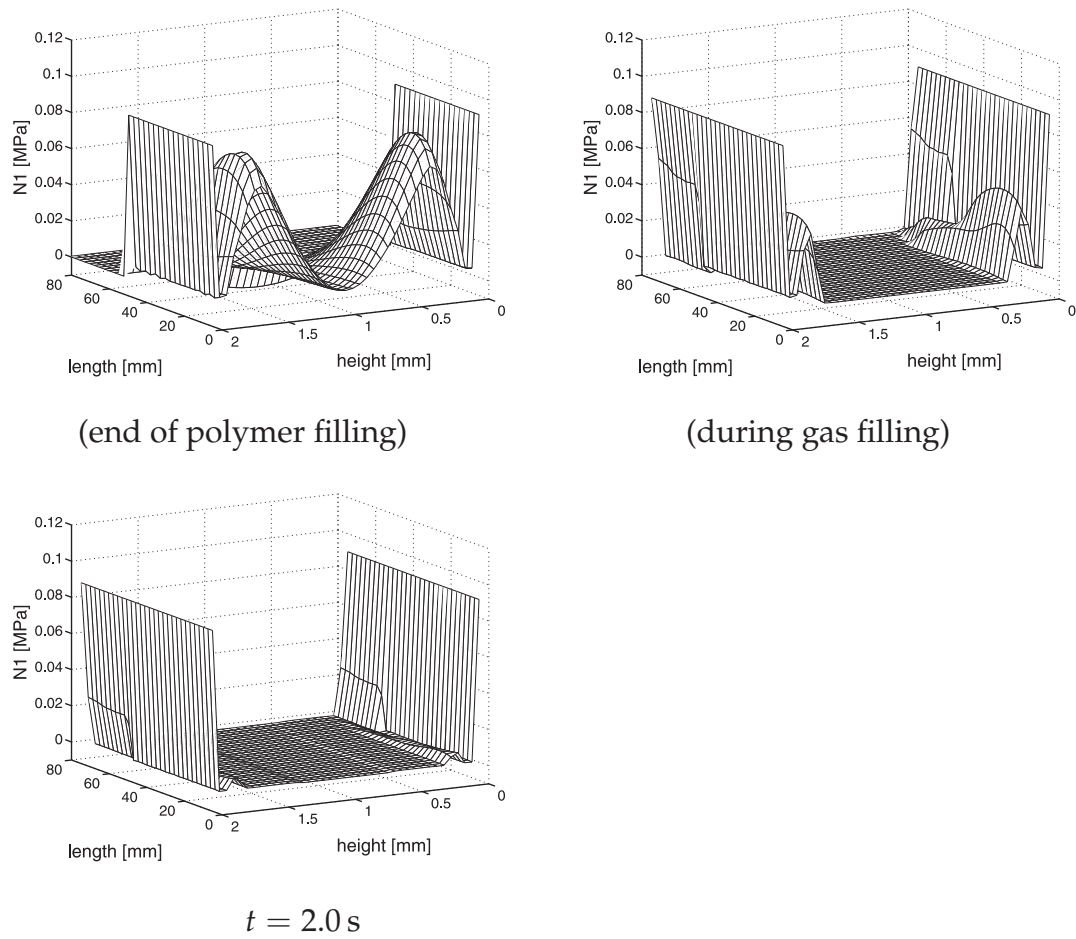


Figure 3.7: Time evolution of  $N1$  in the GAIM case.

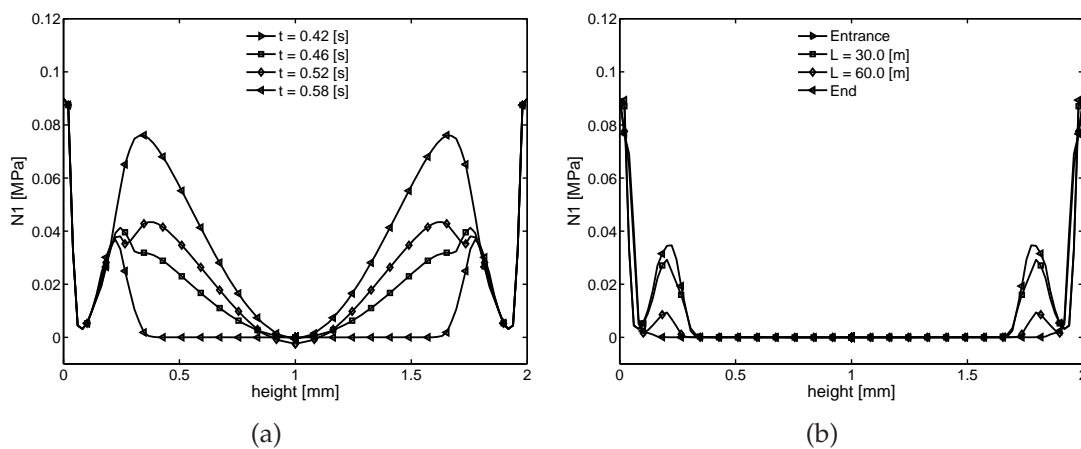


Figure 3.8: (a) Normal stress difference profiles at  $x = 0.02$  m, depicting the transition from polymer filling to gas filling. (b) Normal stress difference profiles along the cavity length after the completion of gas filling.

---

influence of processing conditions and of the part's geometry on computed stresses, which were beyond the scope of our study, are of interest to further exploit the GAIM characteristics, to arrive at superior products with enhanced dimensional stability.





## CHAPTER FOUR

# Thermally and pressure-induced stresses in gas-assisted injection molding

---

### Abstract

Residual stresses are a major issue in the mechanical and optical behavior of injection-molded parts. In this study we analyze the development of thermally and pressure-induced stresses in gas-assisted injection molding (GAIM) of amorphous polymers. A linear viscoelastic model is used for the computation of residual stresses during the filling, packing and holding stages. The model is implemented in a finite-element injection molding code which was developed to deal with three-dimensional flows under non-isothermal conditions. A front-capturing technique is employed to capture the interfaces between the polymer and air/gas. The polymer melt is modeled as a generalized Newtonian fluid, while the air at the downstream of the flow front and the gas are modeled as fictitious Newtonian fluids. The model is tested in a two-dimensional approximated test-geometry, and the differences between conventional injection and GAIM, in terms of predicted residual stresses, are assessed. Results show a significant influence of GAIM decreasing the development of thermally and pressure-induced stresses considerably.

### 4.1 Introduction

Residual stresses in injection molding parts are responsible for post-molding dimensional changes which, depending on the magnitude of the stresses and on the geom-

entry of the part, can induce warpage and negatively influence the product's dimensional stability. They also largely affect the properties of injection molded parts, e.g. mechanical and optical. Its development is associated with two different physical processes: molecular orientation and differential shrinkage. The first is responsible for the development of the so-called flow-induced stresses, which were discussed in the previous chapter, and the second for the development of thermally and pressure-induced stresses.

Differential shrinkage in injection molded parts results from the combined effect of inhomogeneous cooling and pressure. To understand how both mechanisms contribute to the final residual stresses, it is worth to first consider the case of free quenching, in which only thermal stresses develop. Upon quenching a flat sheet of an amorphous polymer, cooling becomes inhomogeneous since material near the surface cools first and faster. Hence, each material point across the sheet thickness solidifies at a different time. As the material layers near the surface solidify and stiffen, they shrink due to thermal contraction, imposing a compressive stress on the molten material in the core region that relaxes fast by viscous deformation. Later, when the core region starts to solidify, shrinkage thereof is prevented by layers previously solidified at the surface. As a consequence, the outer layers are put under compression while the core puts itself under tension upon shrinkage during cooling. Obviously, the residual stress profile depends on the combined effect of inhomogeneous cooling and changes in the elastic properties, in particular the modulus, with temperature and time. For injection-molding parts, which is the case of interest in the present study, the situation is more complex since solidification occurs in the presence of pressure that is only released upon opening of the mold. Due to differences in compressibility between the solidified layers close to the mold walls and the material which is undergoing vitrification, a variation of the pressure level upon cooling leads to differences in residual stresses. Hence, the changes in density of each material point are locally defined by the respective cooling and pressure history. Hastenberg et al. [34] measured the residual stress profile of amorphous polymers in injection-molded flat plates using a removal modified layer technique. In contrast to free-quenching conditions, the authors measured significant tensile stresses near the surface, followed by a compressive transition region and a core under tensile stresses. Such a profile, and remarkably the presence of tensile stresses at the surface, is believed to be responsible for mechanical failure phenomena referred to as environmental stress cracking, see Mandell et al. [80]. Following the conclusions of Zoetelief et al. [134], the residual stress profile in injection molding products is mostly determined by pressure, and not by differences in time of thermal contraction across the part's thickness. In Figure 4.1, residual stress profiles measured on a freely quenched plate and on an injection molded plate, both made of polystyrene (PS), are given. The figures were taken from Hastenberg et al. [34].

The situation for semi-crystalline materials is somewhat different. As was shown by Kamal et al. [58], the residual stress profiles for high density polyethylene (HDPE) are different from those of PS and polycarbonate (PC). More specifically, compressive stresses were found to develop in the core region that increase to tensile stresses

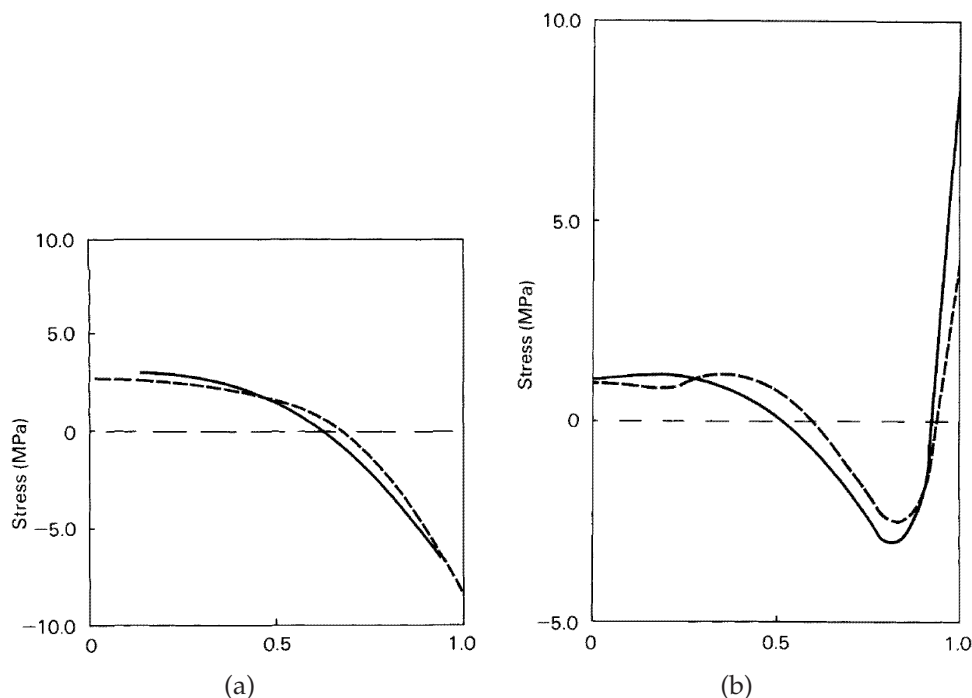


**Figure 4.1:** (a) Stress distributions of free-quenched compression molded PS plates. Solid line measurement results of Hastenberg et al. [34]; dashed line results obtained by Isayev et al. [50]. (b) Stress distribution of injection molded polystyrene samples; solid line: the mold temperature was set to 25 °C, dashed line: the mold wall was set to 50 °C, Hastenberg et al. [34].

towards the walls.

It was found by Baaijens [8], Douven [22], Zoetelief et al. [134] and Kamal et al. [58] that the magnitude of flow-induced stresses is about one to two orders lower than the magnitude of thermally and pressure-induced stresses. However, the ratio between these two contributions to the final residual stresses depends on the polymer. Wimberger-Friedl et al. [132] compared residual stresses, and the relative importance of the underlying mechanisms involved in their development, in injection molded PS and PC parts. The authors justify the lower magnitude of flow-induced stresses in PC, in relation to PS, based on the lower molecular weight and lower relaxation times of PC chains. As chains are more flexible and their relaxation mechanisms faster, they become harder to orient with the flow. However, the contribution of thermally and pressure-induced stresses is supposed to be higher for PC instead, since these stresses scale with the material's modulus.

Even though some research was devoted to the computation of residual stresses in injection molding, there has not been yet a study devoted to understand how residual stresses, i.e. thermally and pressure-induced, develop in gas-assisted injection molding. Given the vast use of GAIM in polymer injection, the need for such type of studies motivates our investigation. The GAIM technology is mostly used to produce parts with hollow sections, structural ribs, bosses or parts with regions with

significant changes in thickness. Even though there are some variants, typically the GAIM process evolves with the following steps: first polymer is injected until the mold cavity becomes partly filled, next (or during the polymer injection) the gas injection stage takes place, which is done in two phases: a gas penetration phase, during which the cavity walls are wet by the polymer melt, and a secondary penetration phase in which gas, under pressure control, holds the polymer part under pressure while cooling takes place. In the end, the gas is vented and the part ejected. Some of the advantages of this technology are the decrease of part's weight, cycle time, injection pressure, clamping force, shrinkage and warpage. Until nowadays, the numerical studies reported on GAIM have mainly focused on the prediction of the gas bubble shape and thickness of the residual polymer layer as a function of process variables, i.e. shot weight, gas pressure, etc, see Li et al. [73], Parvez et al. [89], Polynkin et al. [91]. Given the vast industrial application and high potential of GAIM, it is essential to also focus numerical studies on the prediction of properties. This demands a complete simulation of the gas-assisted injection molding process, involving primary and secondary gas penetration. Our first computational study was on flow-induced stresses in GAIM, here we focus on the influence of applying GAIM on the development of thermally and pressure-induced stresses.

### **An industrial case**

The use of gas-assisted injection molding has been exploited to improve the mechanical behavior of injection-molded parts. Since gas-injection replaces the injection of polymer, notably during the packing and holding stages, the level of pressure required inside the molding cavity to compensate for volumetric shrinkage is considerably decreased, since the gas bubble is able to reach out to the whole part through the polymer molten core. However, in conventional injection molding during the packing phase the pressure inside the cavity has to be such that the material far from the gate can be kept under some pressure. As a consequence, overpacking occurs in the regions close to the gate. Thus, the use of GAIM can significantly decrease and homogenize the level of pressure-induced stresses, having a stronger effect for thin-walled parts with relatively long flow-paths. Figure 4.2 shows an industrial example of a computer CD tray produced via gas-assisted injection molding. The flow-length of the part and the relative low wall thickness would require, when using conventional injection molding, very large pressures to properly pack the molten material inside the cavity. Such high packing pressures would induce very large residual stresses, that could lead to significant warpage. To avoid this, the developers of the part have used gas-assisted injection molding. The cross-section of the part is visualized in Figure 4.2, in which the gas channel is clearly depicted. The gas was injected via gas-needles positioned at several points in the cavity indicated in Figure 4.2.

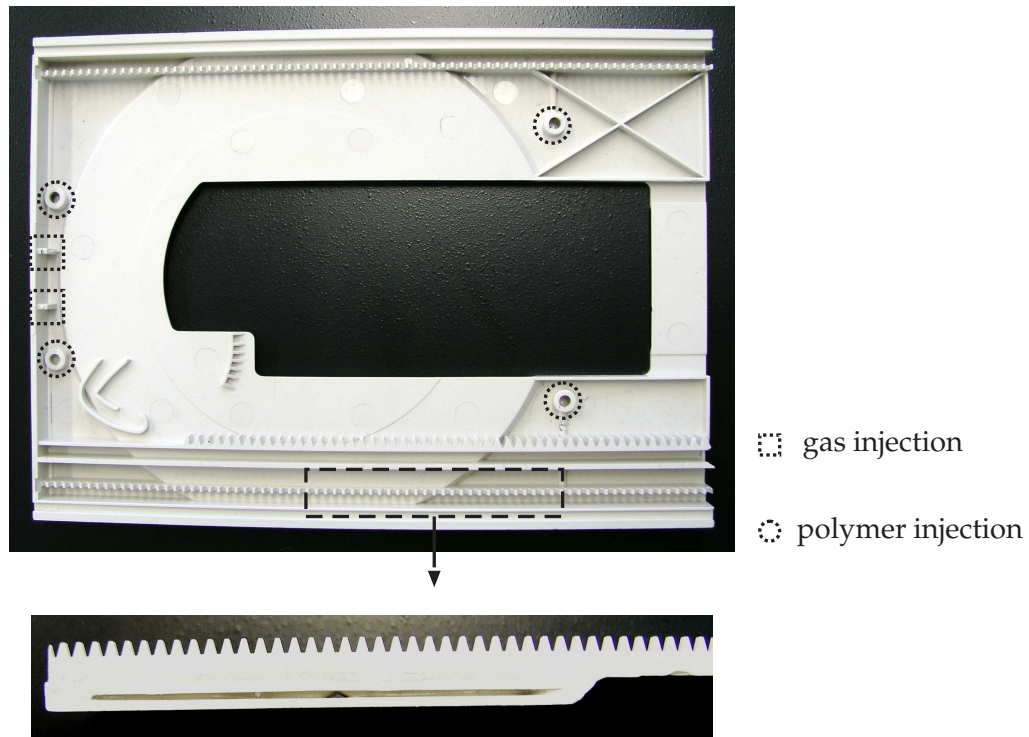


**Figure 4.2:** Gas-assisted injection molded part, with two injection points and four gas-injection points.

### Problem definition

The same injection molding case studied in the previous chapter, in which a polycarbonate is injection molded into a rectangular cavity, is used to investigate the development of thermally and pressure-induced stresses in gas-assisted injection molding. Like in the previous chapter, we investigate a 2-D problem, taking a cross section of the original 3-D geometry of 80x2 mm (length, height), see Figure 3.1. In order to assess the effect of GAIM, simulations are conducted using both conventional and gas-assisted injection molding.

## 4.2 Thermally and pressure-induced stresses

### 4.2.1 Linear thermo-viscoelastic model

Thermally and pressure-induced stresses develop in the solidified layers and are originated by relatively small deformations. In contrast to the melt phase, in which amorphous polymers exhibit a weak liquid-like response, in the solid phase a rigid glass-like response dominates the mechanical behavior. During the packing and holding phases, compressibility becomes the key phenomenon that drives the de-

velopment of residual stresses. As shown by Jansen [51], the change from filling to packing is also marked by a change in relevant mechanisms in the energy balance. Convection and viscous dissipation contributions become negligibly small, when compared with the filling phase, and heat conduction becomes the dominant thermal transport process. The post-filling phases are characterized by a drastic increase in relaxation times and are, consequently, despite the characteristic slow flows through the still molten core, that compensate for shrinkage, capable of inducing still significant molecular orientation. For this we need a nonlinear viscoelastic model, like the compressible Leonov model or the compressible Rolie-Poly model as used in Chapter 3. For the computation of thermally and pressure-induced stresses we simply can employ a linear viscoelastic model, see Baaijens [8]. A viscous-elastic approach has been adopted by others, however such models over predict stress and deformation values, since relaxation effects are neglected. Kamal et al. [58], Zoetelief et al. [134] have shown that a viscoelastic approach leads to a more correct position of the compressive peak and more realistic tensile values in subsurface region and at the wall.

We now present only the final model equations of the linear thermo-viscoelastic model, for a full derivation of the model the reader is referred to Douven et al. [23]. The total Cauchy stress consists of a volumetric part, which accounts for the material elastic response to changes in volume, and a deviatoric contribution which accounts for conformation changes. It reads,

$$\boldsymbol{\sigma} = -p^h \mathbf{I} + \boldsymbol{\tau}_e. \quad (4.1)$$

When linearizing  $\dot{\rho} = \rho \text{tr}(\mathbf{D})$ , and assuming that no relevant pressure and temperature effects exist for  $t \leq 0$ , an explicit relation for the hydrostatic pressure,  $p^h$ , in the solid state is found:

$$p^h = \int_0^t \left( \frac{\alpha}{\kappa} \dot{T} - \frac{1}{\kappa} \text{tr}(\mathbf{D}) \right) dt, \quad (4.2)$$

where  $\alpha$  is the thermal expansion coefficient and  $\kappa$  the isothermal compressibility coefficient, which are defined in Equations (2.11) and (2.12), respectively.

The dependence of the material's viscoelastic behavior on temperature is described using the time-temperature superposition. Thermorheologically simple behavior is assumed, implying that a change in the relaxation times corresponds to a shift on a logarithm time scale. The relaxation times,  $\tau_j$ , and viscosities,  $\eta_j$ , are shifted from a reference temperature  $T_0$  to a current temperature  $T$  by  $a_T$  according to:

$$\eta_j = a_T(T) \eta_{j0}, \quad \tau_j = a_T(T) \tau_{j0}, \quad (4.3)$$

where  $\eta_{j0}$  and  $\tau_{j0}$  are the viscosity and the relaxation time at a reference temperature  $T_0$ . The shift factor  $a_T$  is determined using the WLF equation, Equation (3.14), when  $T \geq T_g$ . Below  $T_g$  the relaxation times become so large that relaxation processes are extremely slow and it is common to set  $T_g$  as the lower bound limit for the time

temperature superposition, implying that:

$$a_T(T) = a_T(T_g) \quad \text{for } T < T_g. \quad (4.4)$$

When no deformations effects before  $t = 0$  exist and assuming the material is thermorheologically simple, the deviatoric part  $\sigma^d$  of the Cauchy stress tensor can be written as:

$$\sigma^d = \sum_{j=1}^m \sigma_j^d, \quad \sigma_j^d = 2 \int_0^t G_{j0} e^{-(\xi_{tj} - \xi_{sj})} \mathbf{D}^d(s) ds, \quad G_{j0} = \frac{\eta_{j0}}{\tau_{j0}}, \quad (4.5)$$

where  $\xi_{qj}$  is the reduced relaxation modulus, which according to the linear Maxwell model is defined as:

$$\xi_{qj} = \int_0^q \frac{1}{a_T(s) \tau_j} ds, \quad q = t, s. \quad (4.6)$$

The thermo-linear viscoelastic model is only solved for  $T \geq T_g$ . Above the glass transition temperature the residual stresses are isotropic and equal to minus the pressure in the melt. The computation of thermally and pressure-induced stresses can be substantially simplified by considering a series of assumptions commonly employed:

1. The material is assumed to stick to the mold for as long the pressure in the symmetry line remains positive.
2. Continuity of stress and strain at the solid melt interface.
3. The normal stress  $\sigma_{22}$  is constant across the part thickness and equals minus the pressure in the melt as long as the temperature at the symmetry line in the mold,  $T^*$ , is larger than the glass transition temperature  $T_g$ .
4. In a coordinate system with the  $22$  direction perpendicular to the filling direction  $11$ , the shear strain component  $\varepsilon_{12}$  is disregarded.
5. As long as pressure remains above zero, at the the symmetry line, the only non-zero strain component is  $\varepsilon_{22}$ .
6. Solidification takes place when the no-flow temperature is reached.
7. Mold elasticity is disregarded.
8. Frozen in or flow-induced stresses can be neglected.

Regarding assumption 8 it was shown by Baaijens [8] and Zoetelief et al. [134] that the order of magnitude of flow-induced stresses is about  $10^2$  lower than the thermally and pressure-induced stresses. Moreover, the addition of flow-induced stresses to the total residual stresses is still matter of some debate. Zoetelief et al. [134] used



the layer removal technique to measure residual stresses parallel and perpendicular to flow direction. They found a difference of less than 20%, suggesting that the influence of flow-induced stresses was small.

## 4.2.2 Incremental formulation

We will now discretize the linear thermo-viscoelastic model expressing it in an incremental formulation. At time  $t = t_n$  the model, given by Equation (4.2) and Equation (4.5), reads:

$$\boldsymbol{\sigma}_n = -p_n^h \mathbf{I} + \sum_{j=1}^m \boldsymbol{\tau}_{j_n}^d, \quad (4.7)$$

$$p_n^h = \int_0^{t_n} \left( \frac{\alpha}{\kappa} \dot{T} - \frac{1}{\kappa} \text{tr}(\mathbf{D}) \right) ds, \quad (4.8)$$

$$\boldsymbol{\sigma}_{j_n}^d = 2 \int_0^{t_n} G_j e^{-(\zeta_n - \zeta(s))/\tau_{i0}} \dot{\boldsymbol{\epsilon}}^d ds. \quad (4.9)$$

The subscript  $n$  indicates the evaluation at time  $t_n$ , at which the model variables are fully determined. For the evaluation of the stress at the next step,  $t_{n+1}$ , it is required to know the temperature and strain fields. We introduce the following incremental variables for  $T$  and  $\zeta$ :

$$\Delta \tilde{\zeta}_{n+1} = \zeta_{n+1} - \zeta_n, \quad \Delta T_{n+1} = T_{n+1} - T_n. \quad (4.10)$$

It is assumed that  $\zeta$  and  $T$  vary linearly between two discrete time steps, implying that  $\dot{\boldsymbol{\epsilon}}$  and  $\dot{T}$  are constant over each time increment. It yields,

$$\dot{T} = \frac{\Delta T_{n+1}}{\Delta t_{n+1}}, \quad \boldsymbol{\varepsilon} = \mathbf{D} \Delta t, \quad \text{for } t \in [t_n, t_{n+1}], \quad (4.11)$$

Next we discretize Equation (4.2), and evaluate the integrals using the trapezium rule:

$$p_{n+1} = p_n + \tilde{\beta} \Delta T_{n+1} - \tilde{K} \text{tr}(\mathbf{D}), \quad (4.12)$$

$$\tilde{\beta} = \frac{1}{\Delta t_{n+1}} \int_{t_n}^{t_{n+1}} \frac{\alpha}{\kappa} ds, \quad (4.13)$$

$$\tilde{K} = \frac{1}{\Delta t_{n+1}} \int_{t_n}^{t_{n+1}} \frac{1}{\kappa} ds. \quad (4.14)$$

The discretization of Equation (4.5) in combination with the trapezium rule, leads to:

$$\sum_{j=1}^m \boldsymbol{\sigma}_{j_{n+1}}^d = \sum_{j=1}^m \zeta_{j_{n+1}} \boldsymbol{\sigma}_{j_n}^d + 2\tilde{G}\Delta\boldsymbol{\varepsilon}_{n+1}^d, \quad (4.15)$$

$$\tilde{G} = \sum_{j=1}^m \frac{G_{j0}}{2} (1 + \zeta_{j_{n+1}}), \quad (4.16)$$

$$\zeta_{j_{n+1}} = \exp \left[ -\frac{\Delta t_{n+1}}{2\tau_{j0}} \left( \frac{1}{a_{T_{n+1}}} + \frac{1}{a_{T_n}} \right) \right]. \quad (4.17)$$

After extensive rewriting of Equation (4.7) for  $t = t_{n+1}$ , the following discretized form for  $\boldsymbol{\sigma}$  is found:

$$\boldsymbol{\sigma}_{n+1} = \tilde{\boldsymbol{\sigma}} + \tilde{K} \text{tr}(\Delta\boldsymbol{\varepsilon}_{n+1})\mathbf{I} + 2\tilde{G}\Delta\boldsymbol{\varepsilon}_{n+1}^n, \quad (4.18)$$

where

$$\tilde{\boldsymbol{\sigma}} = -(p_n + \tilde{\beta}\Delta T_{n+1})\mathbf{I} + \sum_{j=1}^m \zeta_{j_{n+1}} \boldsymbol{\sigma}_{j_n}^d. \quad (4.19)$$

The quantities  $\tilde{\boldsymbol{\sigma}}$ ,  $\tilde{K}$  and  $\tilde{\beta}$  are evaluated when the state at  $t_n$  is determined and the temperature history known up until  $t_{n+1}$ . The stress components of the linear thermo-viscoelastic model are written with respect to the local base  $O_1$ , defined in Figure 3.1. Due to assumption 5 and the knowledge of  $\sigma_{22}$ , the incremental strain component  $\Delta\varepsilon_{22}$  can be eliminated from Equation (4.18):

$$\Delta\varepsilon_{22} = \frac{\sigma_{22} - \tilde{\sigma}_{22}}{a}, \quad a = \frac{3\tilde{K} + 4\tilde{G}}{3}. \quad (4.20)$$

The final form of discretized model reads:

$$\sigma^{n+1} = \bar{a}\Delta\varepsilon_{11} + g, \quad (4.21)$$

where

$$\bar{a} = a - \frac{b^2}{a} \quad \text{and} \quad g = \tilde{\sigma}_{11} + b/a(\sigma_{22} - \tilde{\sigma}_{22}), \quad (4.22)$$

with

$$a = \frac{4\tilde{G} + 3\tilde{K}}{3}, \quad b = \frac{-2\tilde{G} + 3\tilde{K}}{3}. \quad (4.23)$$

## Boundary conditions

In our study we only focus at the development of residual stresses inside the mold while the molded part is still kept under some pressure. Thus, we disregard the situation when, due to the absence of pressure, the part is allowed to move and consequently shrink inside the mold. The ejection stage, in which the part is ejected from the mold cavity and allowed to shrink and deform accordingly to the residual stress field resulting in warpage, is dealt in a separate structural analysis. We follow the so-called residual-stress methods, in which computed residual stresses are used as loading conditions in a structural analysis, to find the equilibrated residual stress profile and corresponding displacement field. In a different approach Baaijens [8] and Douven et al. [23] computed displacements using shell type of elements. More recently, Kennedy [62] proposed a hybrid model in which shrinkage data measured on injection molded specimens are used to calibrate computed residual stresses.

We separate the necessary boundary conditions between those employed inside the mold, during filling, packing and holding phases, and those after the ejection stage employed in the structural analysis, which we will address in a separate section. For the injection phases, filling, packing and holding, we distinguish two situations; for each adequate boundary conditions have to be prescribed:

- *Constrained quench with molten core* - The pressure inside the cavity is positive and the temperature in the nodes located at the symmetry line of the part,  $T^*$ , is still above the glass transition temperature  $T_g$ .

$$p \geq 0, \quad T^* \geq T_g(p). \quad (4.24)$$

All strain components are zero except for  $\varepsilon_{22}$  which must obey  $\int_{h/2}^{h/2} \varepsilon_{22} dx_2 = 0$ . With respect to the local coordinate system the Cauchy stress components read:

$$\sigma_{22} = -p, \quad \sigma_{11} = \tilde{\sigma}_{11} + \frac{b}{a}(-p - \tilde{\sigma}_{22}). \quad (4.25)$$

- *Constrained quench with solid core* - The pressure inside the cavity is positive but the temperature in the nodes located at the symmetry line of the part,  $T^*$ , is below the glass transition temperature  $T_g$ :

$$p \geq 0, \quad T^* < T_g(p). \quad (4.26)$$

The material still contacts with the wall, the only difference with the previous situation is that  $\sigma_{22}$  is prescribed according to Equation (4.27), which is derived from Equation (4.20) and assuming  $\int_{h/2}^{h/2} \varepsilon_{22} dx_2 = 0$ . The Cauchy stress compo-

nents read:

$$\sigma_{22} = \frac{\int_{-h/2}^{h/2} \tilde{\sigma}_{22}/a \, dx_2}{\int_{-h/2}^{h/2} 1/a \, dx_2}. \quad (4.27)$$

$$\sigma_{11} = \tilde{\sigma}_{11} + \frac{b}{a}(\sigma_{22} - \tilde{\sigma}_{22}). \quad (4.28)$$

### 4.2.3 Post-ejection structural analysis

In order to find the equilibrated residual stress profile after ejection, we perform a geometrically non-linear analysis using a finite element package. Residual stress values obtained during the filing, packing and holding phases are interpolated to Gaussian points, imposing on the part a non-equilibrium stress state. The domain is spatially discretized with 4-noded bilinear quadrilateral elements, and the material behavior is described by a linear-elastic constitutive equation. The Poisson ratio for PC  $\nu$  is taken to be 0.37 [123].

#### Boundary conditions

For the gas-assisted injection case, since after the gas injection no polymer is injected to seal the gate we cannot simply run a structural analysis on the entire domain. However, given the homogeneity of the stress field throughout the part's length, see Figure 4.7, we can assume it to be symmetric over the length. In Figure 4.3 we illustrate the computational domain with the proper boundary conditions to exclude rigid body motions. For the conventional injection case no symmetry assumption can be used over the length, since the residual stress profile changes through out the part's length. We therefore carry out a dynamic analysis, in which constraints of rigid body motions are not required. Since the acceleration values are very small, inertia forces negligibly affect the computed stress field. The part is mechanically supported according to Figure 4.4. As an output of the analysis, Cauchy stresses and logarithmic strains are obtained. The magnitude of the computed strains is of  $\mathcal{O} \sim 1^{-3}$ , thus validating the use of a linear-elastic approach. A viscoelastic approach would have been more consistent within the modeling framework here presented, however it was the scope of this study to analyze the development of residual stresses inside the mold during the filling, packing and holding injection phases. The structural analysis carried out upon ejection is only done so that an equilibrium stress state can be found.

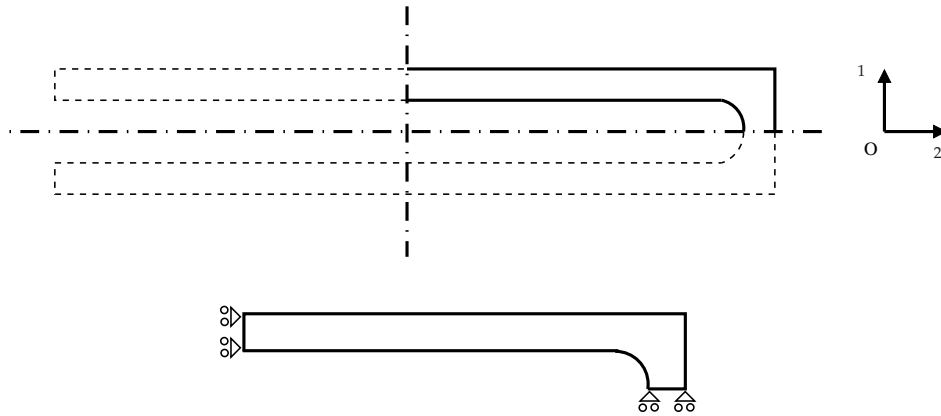


**Figure 4.3:** Boundary conditions employed in the non-linear geometrical analysis for the GAIM case.

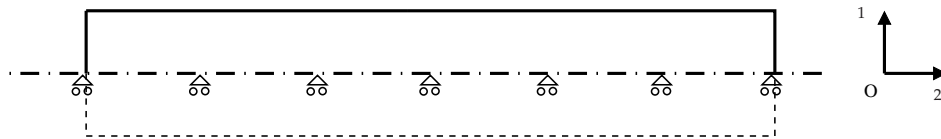


**Figure 4.4:** Boundary conditions employed in the non-linear geometrical analysis for the conventional injection case.

## 4.3 Case study

### 4.3.1 Processing conditions

#### Conventional case

The polymer is injected with an average velocity of  $120 \text{ mm}\cdot\text{s}^{-1}$  at  $320^\circ\text{C}$  during the filling stage. After filling,  $t_f = 0.67 \text{ s}$ , a short packing stage,  $t_p = 0.71 \text{ s}$ , follows until an injection pressure of  $50 \text{ MPa}$  is reached. Subsequently, the pressure level is maintained for  $4 \text{ s}$  during the holding stage before the gate is assumed to freeze off. In fact, during the holding stage in injection molding, the pressure at the inlet changes due to cooling of the gate and its transient effect on the pressure drop. However, for the sake of simplicity, we assume the gate to freeze off instantaneously. The mold wall temperature is set to  $80^\circ\text{C}$ .

#### GAIM case

The polymer is injected with the same conditions as the ones used in the conventional simulations for  $0.44 \text{ s}$ . Immediately after that, gas is injected through a limited height of the inlet with an average injection speed equal to  $200 \text{ m}\cdot\text{s}^{-1}$  until the cavity is fully filled,  $t_f = 0.9 \text{ s}$ . Next a gas pressure of  $0.15 \text{ MPa}$  is imposed for  $2 \text{ s}$ , which is

about 2 times higher than the inlet pressure just before filling. A higher pressure is unnecessary, since pressurized gas can reach the interior of the part everywhere, and is sufficient to pressurize the whole molded part.

### Material properties

The thermal and viscoelastic properties of PC are taken from Baaijens [8] and listed in Table 3.1, together with the parameters for the WLF and Tait equations. To describe changes in specific volume, we use the Tait model proposed by Zooler [135], which became standard for amorphous polymers. The model equation reads:

$$v(p, T) = (a_0 + a_1 (T - T_g)) \times \left(1 - 0.0894 \ln\left(1 + \frac{p}{B}\right)\right), \quad (4.29)$$

in which  $T_g$  is the glass transition temperature, given by  $T_g(p) = T_g(o) + sp$ , and the parameter  $B(T)$  by  $B(T) = B_0 \exp(-B_1 T)$ . The parameters  $a_0$ ,  $a_1$ ,  $B_0$  and  $B_1$  are different for the melt ( $T > T_g$ , indexed with  $m$ ) and the solid state ( $T < T_g$ , indexed with  $s$ ). The total set of parameters is fitted on PVT experiments that are run at quasi equilibrium conditions and measure  $v$  at varying pressures and temperatures. History effects are, therefore, not taken into account.

## 4.3.2 Results & discussion

### Conventional injection molding

Figure 4.5 shows the calculated pressure history inside the cavity in three different positions,  $x_1 = 0.008$  m,  $x_2 = 0.04$  m and  $x_3 = 0.075$  m. The pressure decay is mostly determined by  $\alpha$  and  $\kappa$ , and its evolution has a direct impact on the pressure-induced stresses. Also mold elasticity affects the pressure inside the cavity, by retarding its decay (change in slope), however such effect is neglected in our study, since we model the mold as a rigid body. After the filling stage,  $t_f = 0.67$  s, the change to packing is marked by a steep rise in pressure. Figure 4.6 shows the evolution of the thermally and pressure-induced stress components. At the end of filling only tensile stresses develop in the regions near to the mold walls, induced by the hampered thermal contraction while the pressure is maximum at the injection gate  $L = 0$  and zero at the end  $L = 0.08$  m. In the packing stage, the pressure increases to become uniform inside the mold cavity. Shrinkage upon cooling makes the pressure to lower during the holding stage, and upon further material solidification the pressure keeps on decaying. The pressure history is reflected in the stresses in the solidified layers compared to the bulk. Residual stresses become compressive in layers that solidify under a high pressure, and tensile in those solidified under a low pressure. In the end of the holding stage the stresses in the solidified layers increase proportionally with the pressure relief. If one would continue further the simulations, upon ejection the stresses in the core region would increase until equilibrium would be achieved, hence the integration

of the stress profile across the thickness would yield zero, i.e. tensile and compressive stresses balance each other.

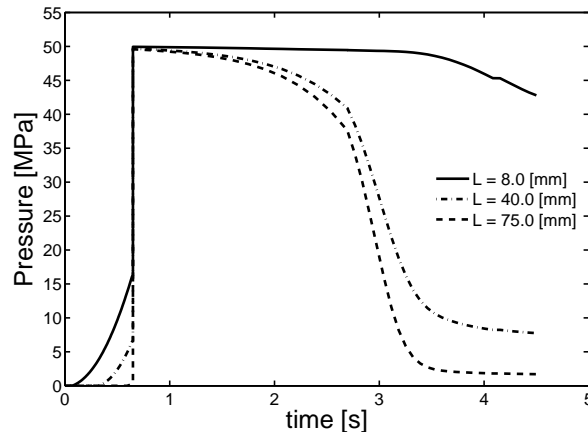


**Figure 4.5:** Pressure history inside the cavity at different locations for the standard injection molding case.

## GAIM

Figure 4.8 shows pressure traces at three different positions along the cavity's length,  $x_1 = 0.008$  mm,  $x_2 = 0.04$  mm and  $x_3 = 0.075$  mm. The transition from polymer to gas injection can be seen by a decay and a subsequently growth of the pressure traces at  $t_f = 0.3$  s at positions  $x_1$  and  $x_2$ . The difference between the computed pressure histories for the conventional and GAIM cases immediately suggests that the residual stresses in GAIM should differ substantially. In GAIM, the end of filling occurs at a decaying pressure, since only the molten-liquid material in the core region is displaced, and the packing, and subsequently holding, pressure are much lower. Also for the GAIM case, during the holding stage the pressure inside the cavity remains constant and therefore the polymer material solidifies at a constant pressure. Figure 4.7 shows the evolution of the thermally and pressure induced  $\sigma_{11}$  stress component. The profiles in the end of filling show a slightly higher tensile stress than in the conventional case. This can be related to the increased cooling in GAIM, which results from the absence of a molten core and a longer filling time. In Figure 4.9 temperature profiles are plotted in the middle of the part in the end of the respective filling stages for both conventional injection molding and GAIM. The increased cooling in the case of GAIM is clear. As a result of a shorter cooling time and a higher cooling rate, the thermal contraction prevented during filling is expected to be higher, thus inducing higher tensile stresses. As cooling proceeds, the tensile stresses propagate to reach the inner surface, resulting in a arc-type profile. Given the significant lower pressures, specially in the packing stage, the development of a compressive peak does not occur inside the mold. Figures 4.10(a) and 4.10(b) give the evolution of the resid-

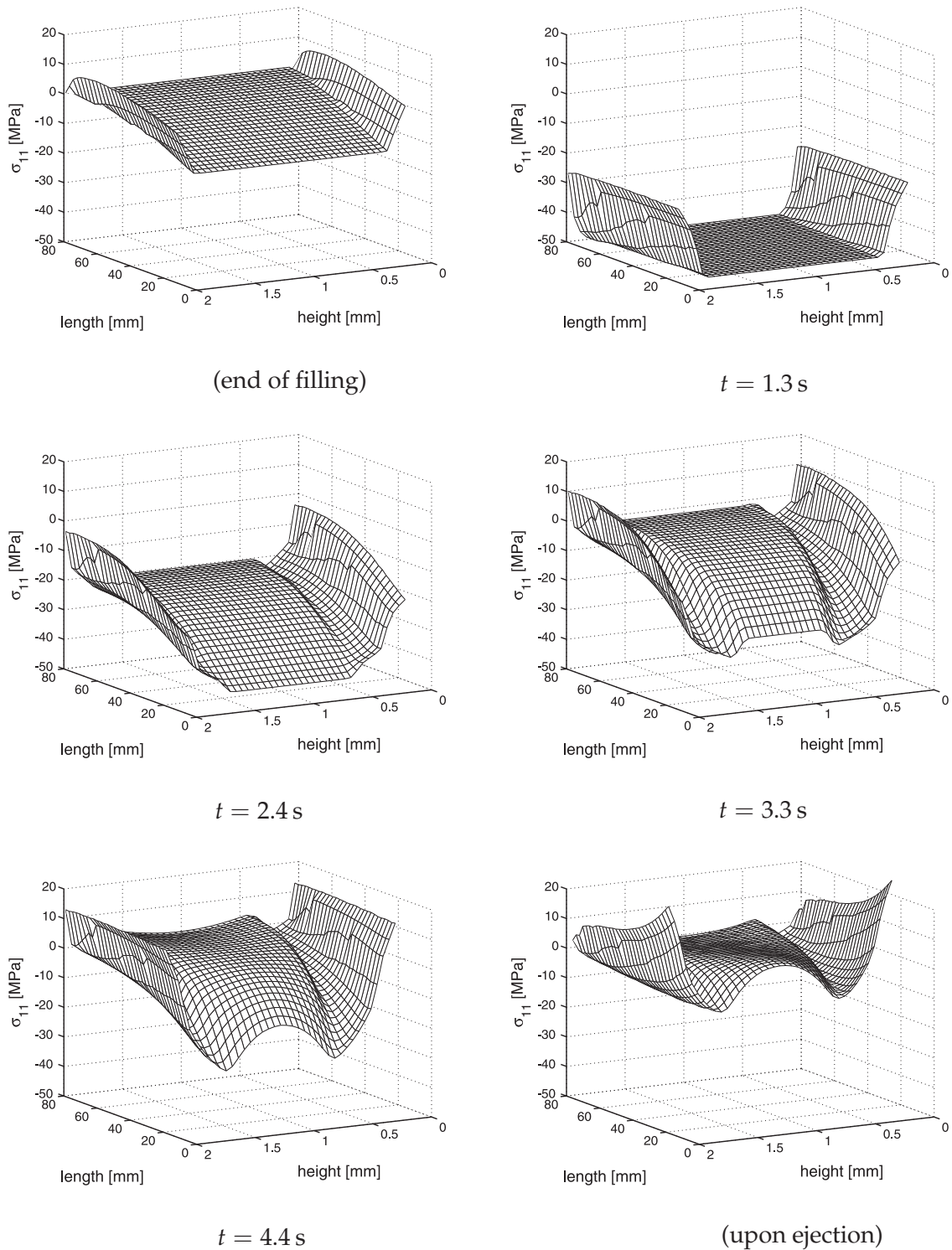


**Figure 4.6:** Time evolution of thermally and pressured-induced stresses in the convention injection molding case.



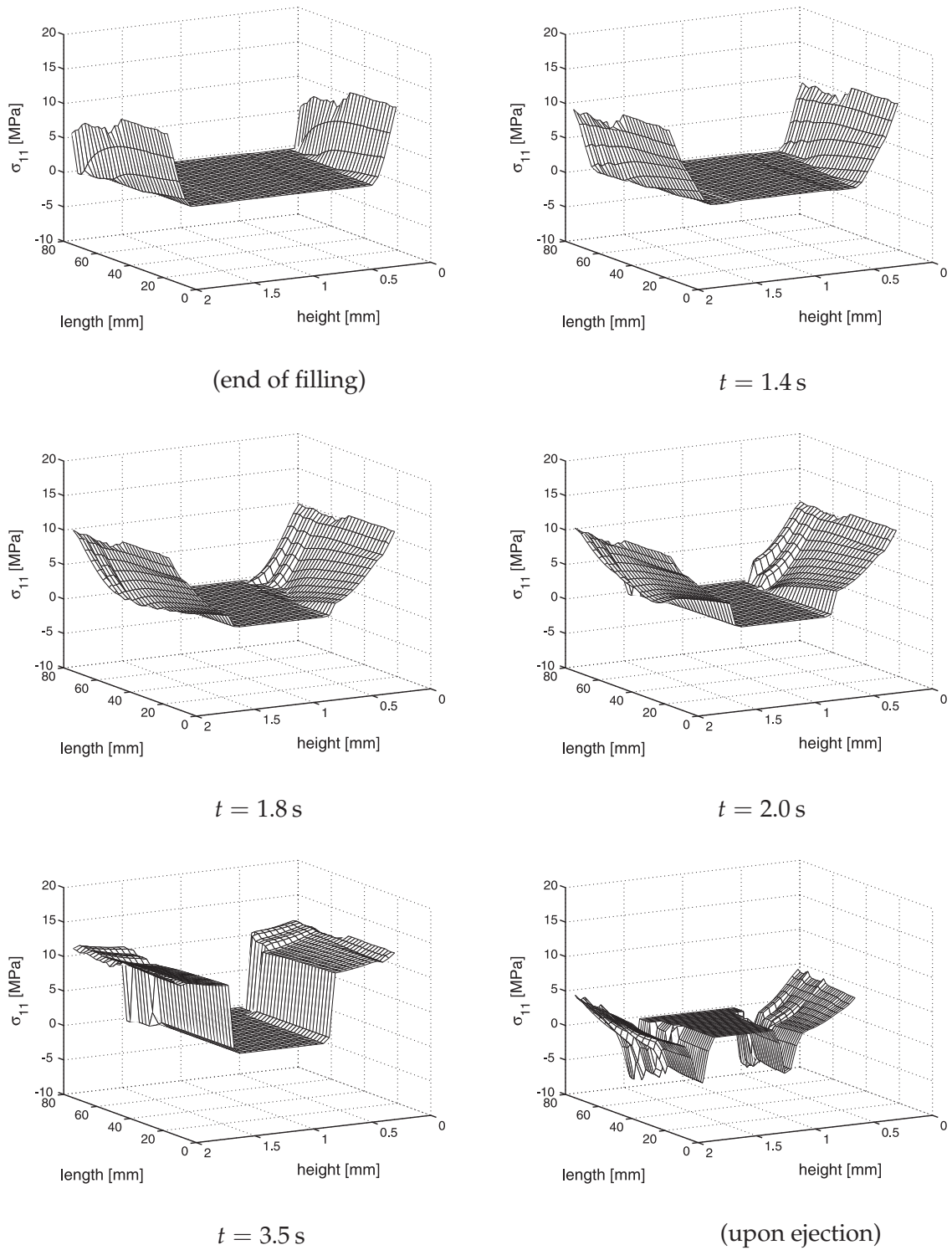
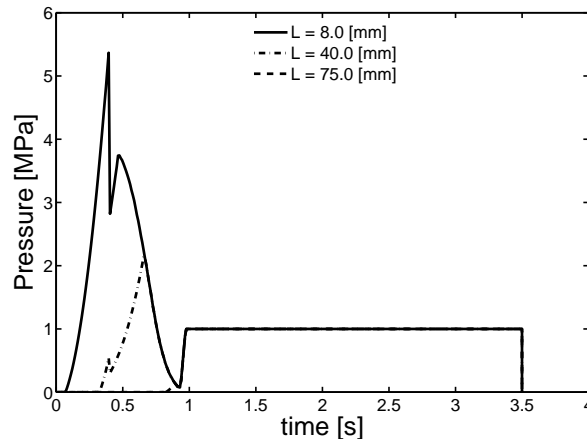
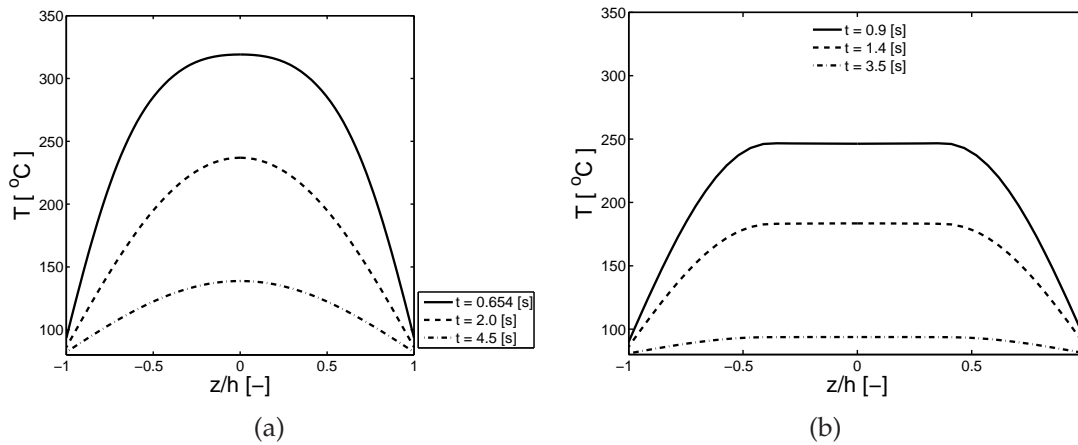


Figure 4.7: Time evolution of thermally and pressured-induced stresses in the GAIM case.

ual stress profiles in  $x_2$  in time, for conventional injection molding and GAIM. The final residual stress profiles obtained from the structural analysis are given in Figure 4.11.



**Figure 4.8:** Pressure history inside the cavity at different locations for the GAIM case.



**Figure 4.9:** Temperature history at  $x_2 = 0.04$  m for: (a) conventional injection molding; (b) GAIM.

### A note on material data assumptions

In injection molding the high cooling rates and pressures inside the mold cavity pose considerable challenges if one aims to characterize the material under such conditions. Measuring limits in current devices make it difficult to probe material data under such severe experimental conditions. We will next enumerate some of the

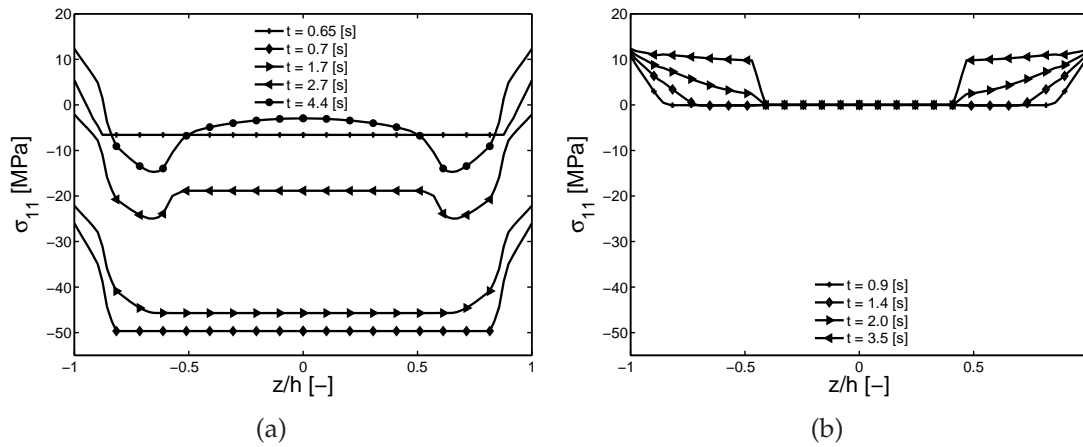


**Figure 4.10:** Thermally and pressured-induced stresses at  $x_2 = 0.04$ : (a) conventional injection molding; (b) GAIM.

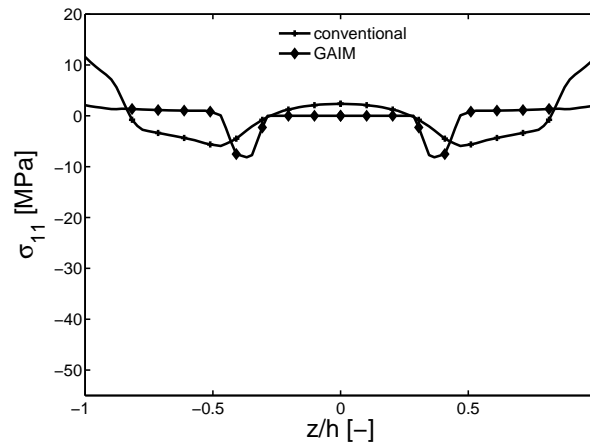


**Figure 4.11:** Thermally and pressured-induced stresses at  $x_2 = 0.04$  m upon ejection.

shortcomings that result from experimental difficulties related to property characterization.

1. The thermal conductivity of polymers mostly depends on both temperature and molecular orientation. It is known that upon processing the thermal conductivity of polymers is increased in the flow direction and decreased in the direction normal to the flow. Such observations were reported by, e.g, Hansen and Bernier [32] and van den Brule and O'Brien [120] and explained on the basis that the heat conductance is much higher along covalent bonds than throughout weak secondary bonds. Furthermore, the anisotropy resulting from the frozen-in molecular orientation can differ substantially according to the molecular structure of the polymer, being favored by linear compact polymers, and for polymers with higher relaxation times and molecular weight. Hansen

and Ho [33] and van den Brule and O'Brien [120] give a theoretical treatment that relates the anisotropy of thermal conductivity with the viscoelastic molecular deformation. All this is not taken into account and thus errors are introduced in the simulations.

2. Thermal capacity, like the thermal conductivity, is also influenced by cooling history and is also currently measured at too low cooling rates. Thus measured data are not accurate at the transition from melt to solid.
3. The PVT data available for most materials are measured under relatively low cooling rates, mostly due to the high thermal inertia of existent measuring devices, and without considering the influence of flow. As a consequence, most injection molding simulations use models in which the specific volume,  $\nu$ , is measured under varying temperatures and pressures measured in quasi-equilibrium conditions, hence neglecting history effects. Recently Van der Beek [121] proposed a new PVT apparatus, a confined fluid dilatometer, which can measure PVT data in ring-type samples at high cooling rates ( $100\text{ }^\circ\text{C s}^{-1}$ ) under high pressures (up to 100 MPa). Additionally, the device allows to generate flow prior to cooling with shear rates of  $\mathcal{O}(10^2 - 10^4\text{ s}^{-1})$ . This is of special importance to study semi-crystalline polymers, due to the well know effect of flow on crystallization kinetics.
4. The thermal expansion coefficient is affected by frozen-in orientation. As it was mentioned by Struik [114], such phenomenon can be observed in experiments like thermal twisting. When a bar of an amorphous polymer is twisted above  $T_g$  and subsequently cooled down below  $T_g$ , the angle of twist will reversibly increase upon cooling and decrease upon heating. This is a consequence of the expansion the material undergoes on cooling and the contraction it undergoes on heating. The author explains that such phenomena are due to the fact that entropic stresses (flow-induced stresses) will vary reversibly with temperature, increasing upon heating and decreasing upon cooling.

In our computations we use a constant and isotropic thermal conductivity as well as a constant heat capacity. We justify such an option based on the fact that the aim of this study is to assess the influence of GAIM on the development of residual stresses and not to analyze the influence of material data on residual stress profiles.

## 4.4 Conclusions

A method is proposed for the computation of residual stresses in gas-assisted injection molding, in which a thermo-viscoelastic model is used to compute thermally and pressure-induced stresses. Residual stresses are computed for a polycarbonate injection molded plate processed via conventional injection molding and via GAIM. Computed stress profiles for GAIM exhibit slightly higher tensile stresses at the surface, however the most noticeable difference is the absence of a compressive region,

which is typical for conventional injection molded parts. This can be explained by the fact that the pressures for GAIM are much lower than those of conventional injection molding during the packing and holding stages. Knowing that in injection molding pressure-induced stresses overrule the contribution for the total residual stresses it has been show that GAIM can drastically change the residual stresses in injection molded parts. The simulations can be improved with constitutive models for density and heat conduction with better characterized material data. In the future, the effects of processing conditions and of the geometry of the part are of interest to assess. The numerical model presented here is capable of performing residual stress computations on full 3-D problems of complex geometries.

# Crystallization in injection molding prototype flows

---

### Abstract

Injection molding of semi-crystalline  $\alpha$ -olefin polymers is a frequently applied production method. Solid-state properties, e.g. mechanical and optical, are related to the underlying material microstructure, which is largely determined by the processing conditions. During injection, the molten material is submitted to a complex thermal-mechanical history in which phase-changes occur in conditions far beyond equilibrium. This complex problem is coupled; the processing conditions determine the evolving morphology and type of crystalline structure, which, in turn, affect the melt rheology. To control the final properties of products, an accurate prediction of the material microstructure developed upon processing is required. To address this problem we model the experiments reported in [39, 40], in which the morphology development of an isotactic polypropylene (iPP) resin was studied using experimental setups specially designed to generate flows with fully controlled initial and boundary conditions. A model for flow-enhanced nucleation is proposed within the framework of molecular-based rheological modeling, which relates molecular deformation with the enhancement of crystallization. The model is implemented in a finite-element injection molding code in which flow-kinematics are computed. In a decoupled fashion, flow-kinematics are used to solve a coupled viscoelastic stress - crystallization problem. A morphological description concerning the number, size and shape of crystalline structures is predicted and a comparison between computational and experimental results is made.

## 5.1 Introduction

The microstructure of semi-crystalline polymers results from a variety of physical changes that occur during processing. Notably, in injection molding such changes take place under extreme conditions characterized by high shear rates, high-pressure levels, high cooling rates and steep temperature gradients. The morphology of the material develops accordingly to these conditions and the part geometry. An important physical process during processing is crystallization, which is coupled to the flow history: flow induces crystallization, crystallization changes the rheological behavior, and thus the flow. Furthermore, crystallization plays a dominant role in the final properties of injection molding parts. However, the effect of crystallization on macroscopic properties is difficult to predict and, therefore, also difficult to control. Typically the microstructure of an injection molded part, when visualized under polarized optical light microscopy, consists of different layers: a highly oriented layer close to the surface, a second oriented shear layer, a fine-grained layer and a spherulitic core [24]. This layer-type morphology introduces a high degree of anisotropy in physical properties [27, 97]. The effect of processing conditions on the morphology of the microstructure of injection molded parts has been extensively investigated. For example, Viana et al. [128] found the oriented-layer/core ratio to vary most strongly with varying injection speed and injection temperature.

In order to unravel the intrinsic relation between product properties and the underlying crystalline morphology, research effort has been devoted to predict the microstructure of injection-molded parts of semi-crystalline materials. Most of the studies focused on isotactic polypropylene (iPP), due to its high potential for property tuning and its vast use in applications where crystallinity determines the mechanical and optical properties. Pantani et al. [86] gives an extensive review on available models and experimental techniques to predict and characterize the morphology of injection-molded parts. The authors propose a model to predict the morphology of injection-molded iPP, in which flow kinematics are computed using a lubrication approximation. Polymorphism was accounted for, using the Avrami-Evans-Nakamura equation to describe the crystallization kinetics of the mesomorphic phase, while the evolution of the  $\alpha$  phase was modeled using Kolmogoroffs model [67]. The growth-rate of spherulites was described by the Hoffman-Lauritzen expression [37]. Smirnova et al. [108] used a differential set of Avrami equations to predict crystallinity and the average size of spherulites in injection molding, but in their study only temperature effects were taken into account. In a different study, Pantani et al. [87] investigated the effect of varying the packing pressure on the morphology of injection molding samples. The effect of pressure on crystallization kinetics was also assessed in a study by Watanabe et al. [131], in which the authors measured the half time,  $t_{1/2}$ , for crystallization (defined as the time at which the volume fraction of crystallized material reaches 50% ) and verified that pressure indeed simply acts as to increase undercooling. Van der Beek [121] experimentally studied the combined effect of pressure, cooling rates and shear deformation on the specific volume of iPP, in a new PVT apparatus which allows PVT measurements at high cooling rates (100

$^{\circ}\text{C s}^{-1}$ ) and pressures (up to 100 MPa). Additionally, the device makes it possible to generate flows prior to cooling with shear rates in the order of  $10^2 - 10^4 \text{ s}^{-1}$ . Experiments like these, will certainly provide the input for further improvement and validation of the theoretical models.

Flow effects on crystallization in injection molding simulations are often taken into account by adopting a modified version of the Nakamura equation [84]. Within this approach, Hieber [35] defined a characteristic time for crystallization that was made dependent on temperature, pressure and the absolute value of the shear stress. Kim et al. [64] modified the crystallization rate constant in the Nakamura model, making it dependent on the shear rate. The authors tried to predict the thickness of the oriented shear-induced layer using a thermodynamic approach, in which viscoelastic stresses were computed to find changes in entropy associated with the flow. Making use of Flory's expression [25] that relates the equilibrium melting temperature,  $T_m$ , with changes in entropy, the authors could determine a new elevated nominal melting temperature resulting from the entropy decrease imposed by the flow. The transition from spherulitical core to oriented shear layer was assumed to take place when the local temperature would equal the calculated  $T_m$ . Even though their results qualitatively describe the experimental data, they still fall short from providing morphological detail.

Summarizing, most of the numerical studies on injection molding of semi-crystalline materials give few insight in the morphology developed, failing to provide information about the shape and dimensions of oriented crystalline structures. Also, the crystallization models employed lack molecular understanding, and they do not couple flow-induced crystallization with melt rheology. Furthermore, often similar growth mechanisms for non-oriented and oriented crystals are assumed, which is in clear contradiction with experimental evidence that shows the growth kinetics of a spherulite to be profoundly different from that of a shish [65].

Advances in the physical understanding of flow-associated effects on crystallization have been recently reviewed by Somani et al. [110] and Kumaraswamy [68]. It has been experimentally observed that long chains, the high end tail of the molecular weight distribution, play a dominant and decisive role accelerating the kinetics of flow-induced crystallization [53, 99, 109, 129]. Seki et al. [99] showed that with the addition of just 1% of chains with a number average molecular weight  $M_w$  five times larger than that of the matrix resin, crystallization kinetics are profoundly changed. Special experimental setups have been developed to perform short-term shear experiments in semi-crystalline polymer melts at strain-rate levels close to real processing conditions [52, 53, 69, 74, 75]. In these experiments a polymer melt is held above its equilibrium melting temperature for some time, such that any residual ordering or structure becomes erased, and subsequently cooled to a desired crystallization temperature at which the material is subjected to a brief shear deformation. The crystallization temperature is chosen such that quiescent crystallization takes place over a time scale much larger than those being investigated. The changes in microstructure are monitored during and after the flow. These studies provide insight into the ki-



netics of flow-induced nucleation and its dependence on flow conditions, as well as morphological detail of oriented crystals. Mechanical deformation of the melt (shear or extension) was found to significantly enhance nucleation, and the increase of deformation rate to be more effective than that of deformation time. In their early work on dilute solutions under elongational flows, Keller and Kolnaar [61] could already identify that upon a critical strain-rate an abrupt change in birefringence, that was associated by the authors to a coil-stretch transition of the chains conformation, occurs. Keller reasoned that such change in chains conformation could also occur in entangled polymer melts beyond a critical strain rate, and lead to the formation of oriented crystals (row nucleation). More recently, Seki et al. [99] used short-term shear experiments on iPP melts at constant wall shear stress, and identified a critical shear stress that is needed to induce the transition from spherulitical to oriented crystal growth, which was found to decrease with the addition of long chains. The authors explain that a critical stress threshold has to be surpassed to generate threadlike precursors that template row-nucleated structures (shish).

In an attempt to unify all these findings, Van Meerveld et al. [125] classified different flow regimes according to the Deborah number, defined as the product between strain-rate (in shear or elongation) and a characteristic relaxation time of the melt. Two time scales were considered: the disengagement time,  $\tau_d$ , associated with the reptation process and the Rouse time,  $\tau_R$ , associated with the fast chain retraction mechanism. For each time scale a corresponding Deborah number was calculated considering only the longest relaxation times associated with the longest chains, namely: a Deborah number based on the disengagement time  $De_d$ , and a Deborah number based on the Rouse time  $De_R$ . It was found that when  $De_d > 1$  and  $De_R < 1$ , an increase of orientational order occurs leading to an enhancement of point-like nucleation. For  $De_d > 1$  and  $De_R > 1$ , the onset of chain stretching occurs leading to the growth of oriented crystals (fibrillar regime). The latter regime was associated with changes in molecular conformation due to rotational isomerization.

### Flow-regimes based models

From short-term experiments in a duct, Jerschow and Janeschitz-Kriegl [53] could relate the size of the oriented shear and fine-grained layers with the shear rate and shear time. It was found that at the boundary between the fine-grained layer and core  $\dot{\gamma}_c^2 t_s$  was constant, with  $\dot{\gamma}_c$  defined as a critical shear rate, and  $t_s$  the shear time. In the same way the transition to the highly oriented shear layer was characterized by a constant  $\dot{\gamma}_c^4 t_s$ . Based on these findings Eder and Janeschitz-Kriegl [24] proposed a model for flow-induced crystallization in which a critical shear-rate acts as a threshold to generate oriented crystalline morphologies. The model consists of a set of differential equations from which the number of flow induced nuclei, the total shish length per unit volume and the total volume of oriented crystals can be obtained. Later, Zuidema et al. [137] proposed a modified version of the Eder model, the  $S_{j2}$  model, in which molecular orientation and stretch, computed from the second invariant of the deviatoric part of the elastic Finger tensor (also called recoverable

strain tensor),  $J_2(\mathbf{B}_e^d)$ , drives flow-induced crystallization. The non-linear increase in nucleation density as a function of the deformation applied is explained as the result of a self-enhancing process: *flow induces nucleation and nucleation strengthens the flow*. Zuidema assumed that flow-induced nuclei act locally as physical crosslinks increasing the relaxation time of the longest molecules. Thus, enhancing the molecular deformation and increasing the number of oriented chain segments, which are envisioned as precursors for new nuclei. Zuidema tested his model on the experiments of Jerschow and Janeschitz-Kriegl [53] and found that the  $J_2(\mathbf{B}_e^d)$  of the highest relaxation mode remains constant at the transition from spherulitical core to oriented shear layer, corroborating experimental evidences of the dominant role of long chains on flow-induced crystallization in polydispersed melts.

## Motivation

Most of the studies that deal with morphology development of semi-crystalline polymers upon processing, generally follow an approach that combines experiments with numerical simulations. However, most of the correlations drawn between processing conditions and morphology, e.g. skin layer thickness, are still based on models that lack physical detail, and on experiments performed in injection molding machines. The modeling of such experiments is over simplified by neglecting the flow history inside the machine during plastification. Recent findings suggest that even at high temperatures substantial order can be formed or remain in the melt. Azzurri and Alfonso [7] measured the relaxation of shear-induced nucleation precursors in melts at temperatures slightly above the equilibrium melting temperature and found flow to affect the kinetics of crystallization, even when allowing the melt to relax for considerable times before cooling it down to crystallization temperature. Furthermore, upon increasing the concentration of long chains in the melt the relaxation times of the nucleation precursors were found to increase. Similar results were found by Vleeshouwers and Meijer [129]. They reported that after short term shearing of iPP at 200°C, followed by a waiting period of 30 minutes at 200°C, the influence of the flow-induced precursors on crystallization was still measurable. Regarding injection molding the implication of these studies is obvious: the complex deformation the material experiences inside the machine before injection is unlikely to be fully erased and therefore its effect on the developed morphology cannot be neglected. This strongly supports that morphological studies of semi-crystalline materials, in first instance should be carried out under conditions in which the initial state of the material is known.

In the present study we make use of experimental results obtained using two experimental tools, a multipass rheometer and a capillary rheometer. Both allow to study crystallization phenomena at high shear-rates, but under controlled deformation and thermal histories, which, in contrast to the situation in real injection molding machines, are known *a priori*. Hence, the influence of flow on crystallization kinetics and developing morphology can be quantified and experimental conditions can be accurately translated into boundary conditions for numerical simulations. We de-

velop a model for flow-induced crystallization, which revises the underlying model-ideas of the  $S_{J2}$  model [137] and the recently proposed model by Steenbakkers and Peters [113], to predict the morphology of the oriented crystalline phase. Summarizing, we see the present study as a necessary step to validate kinetic models for flow-induced crystallization and to understand the morphological development of crystalline structures in flow conditions close to injection molding conditions.

## 5.2 Injection molding prototype flows

### 5.2.1 Material selection

The research conducted on flow-induced crystallization in our group has been restricted to a small number of different materials, such that extensive material data, obtained from rheological measurements and crystallization studies, could be collected. Obviously, for modeling purposes in studies that aim at morphology prediction, the availability of extensive material data is crucial. In this study we restrict ourselves to a pure linear isotactic polypropylene (grade HD120MO, Borealis) which was studied previously [39–42, 113, 121, 127], yielding molecular weight-related properties and DSC-measured melting temperature, see Table 5.1.

**Table 5.1:** Physical properties of iPP HD120MO.

Grade	$M_w$ [kg mol <sup>-1</sup> ]	$M_w/M_n$	$T_m$ [°C]
HD120MO	365	5.4	163

The rheological properties at a temperature of 190 °C are given in Table 5.2. The relaxation spectrum of the material was obtained using a discrete Maxwell relaxation time spectrum, satisfying [78]:

$$G'(\omega) = \sum_i g_i \frac{\omega^2 \tau_i^2}{1 + \omega^2 \tau_i^2} \quad (5.1)$$

$$G''(\omega) = \sum_i g_i \frac{\omega \tau_i^2}{1 + \omega^2 \tau_i^2} \quad (5.2)$$

where  $G'$  and  $G''$  are the storage and the loss modulus, respectively. The set of relaxation moduli,  $g_i$ , and times,  $\tau_i$ , were determined elsewhere [127]. The temperature dependence of the horizontal ( $a_T$ ) and vertical ( $b_T$ ) shift factors is described using the

WLF equation, Equation (3.14). A Cross model [78] is used to describe the temperature and shear rate dependence of the viscosity.

**Table 5.2:** Rheological parameters at 190 °C for iPP HD190MO: time-temperature shift factors,  $a_T$  and  $b_T$ , Maxwell relaxation spectrum,  $g_i$  and  $\tau_i$ , and generalized Newtonian viscosity Cross model parameters.

Shift factors	$T$ [°C]	$a_T$	$b_T$
	135	4.944	1.065
	145	3.579	1.045
	155	2.557	1.036
	165	1.894	1.088
	175	1.328	0.974
	190	1.000	1.000
	205	0.760	1.007
	220	0.584	1.035
	235	0.472	0.949
	250	0.358	0.974
WLF	$C_1$	$C_2$ [°C]	—
	2.149	225.8	—
Maxwell	Mode	$g_i$ [Pa]	$\tau_i$ [s]
	1	9.0200	0.002
	2	4.2100	0.010
	3	1.8200	0.051
	4	0.5620	0.258
	5	0.0878	1.300
	6	0.0109	6.580
	7	0.0075	33.200
Cross	$\eta_0$ [Pa s <sup>-1</sup> ]	$K$ [s]	$n$ [-]
	$4.8489 \cdot 10^3$	0.2674	0.3878

The thermal properties of iPP HD120MO as taken from Moldflow material database, are assumed to be constants, and are listed in Table 5.3.

**Table 5.3:** Thermal properties of iPP HD120MO.

$c_p$	3175.3	[J kg <sup>-1</sup> K <sup>-1</sup> ]
$\lambda$	0.11	[W m <sup>-1</sup> K <sup>-1</sup> ]

## 5.2.2 The multipass rheometer - morphology development under quasi-isothermal conditions

Recently a modified multipass rheometer (MPR) based on the original device developed in the group of prof. Malcolm Mackley, UK, [77] was proposed by Housmans et al. [39]. In Figure 5.1(a) a schematic representation of the multipass rheometer is given. The pistons 'A' are driven by means of hydraulics which is not shown here. The MPR can incorporate different flow geometries and allows in-situ studies on the kinetics of flow-induced crystallization and its relation to the crystalline morphology, under a controlled thermal-mechanical history. Both steady and small and large amplitude oscillatory shear flows can be generated. Additionally, the double-piston configuration allows to study advanced injection molding processes, such as Push-Pull [60] and Scorim [56], in which by reversing the flow inside the mold cavity during cooling, material solidification takes place under a continuous shear field.

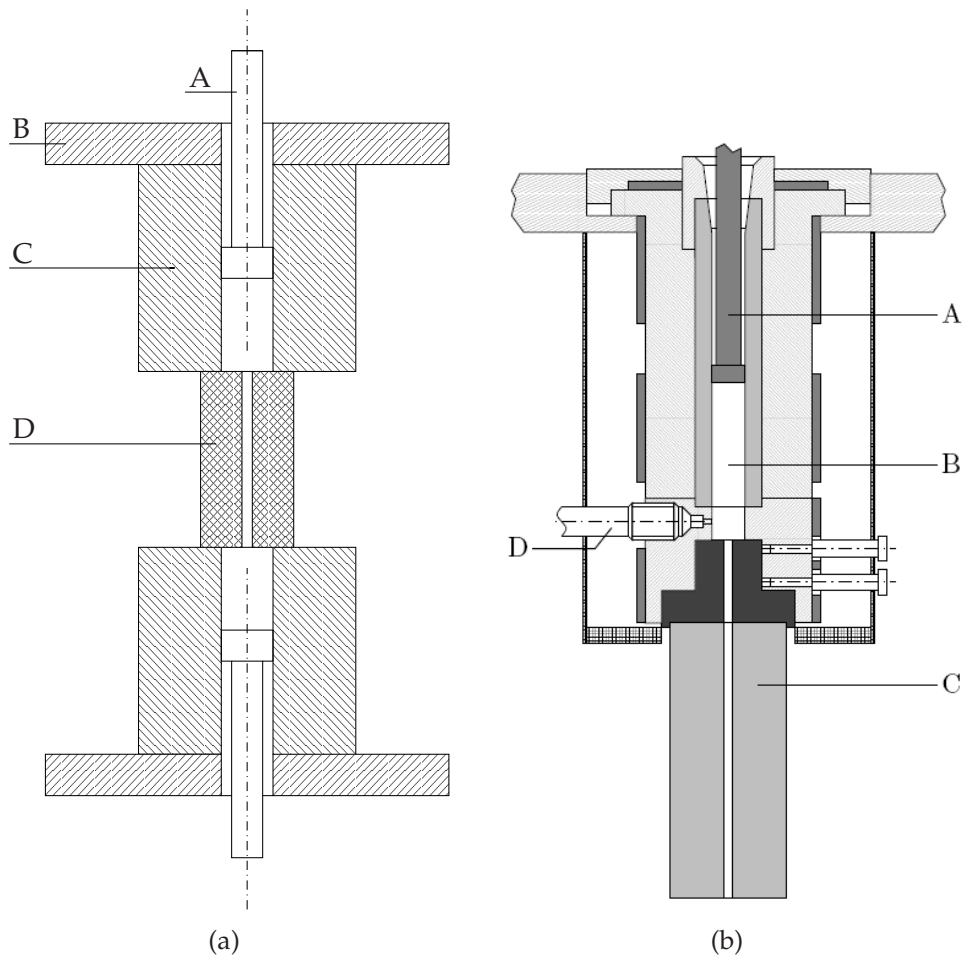


**Figure 5.1:** (a) The multipass rheometer: A) piston; B) moving platen; C) heating/cooling barrel; D) slit-flow geometry. (b) The capillary rheometer: A) Piston; B) Material reservoir; C) Rectangular shaped mold; D) Pressure transducer.

In this study we focus on the experiments reported in [39], in which the MPR is equipped with a slit geometry of dimensions (120x6x1.5 mm). The material is held above its equilibrium melting temperature at 220 °C for 10 minutes, and subsequently cooled down to the desired temperature at which flow is applied. Such protocol has the purpose of erasing any deformation history prior to the flow. The flow time,  $t_f$ , is restricted to prevent material that passed through the contraction region between the cylinder and the slit from reaching the view point. Thus, entrance effects are excluded from the analysis. The flow time is determined by:

$$t_f = \frac{0.5.L}{v_{\max}}, \quad (5.3)$$

in which  $L$  is the slit length, and  $v_{\max}$  the maximum velocity inside the slit, which, for a Newtonian-fluid behavior, is estimated by  $v_{\max} = 1.5.v_{\text{avg}}$ , in which the average velocity is prescribed for each experiment. The different flow conditions used are listed in Table 5.4.

**Table 5.4:** Flow conditions for the MPR experiments.

conditions	$t_{\text{flow}}$ [s]	$v_{\text{avg}}$ [ $\text{m s}^{-1}$ ]	$T_{\text{flow}}$ [°C]
MPR1	0.1875	0.2	165
MPR2	0.375	0.1	145
MPR3	0.375	0.1	165
MPR4	3.0	0.0125	145

### 5.2.3 The capillary rheometer - morphology development under non-isothermal conditions

A capillary rheometer resembles early injection molding machines that employed, instead of a reciprocating screw, a plunger to pressurize and push the melt into a mold. Capillary rheometers are designed to measure the rheological properties of polymer melts at high shear rates, forcing the melt to flow into a capillary or a slit geometry. Since the material is homogeneously molten inside a cylinder under no-flow conditions, a uniform thermal-mechanical history is attained before injection. Housmans et al. [40] adapted a capillary rheometer (Rheograph 6000, Göttfert Werkstoff-Prüfmachinen GmbH, Germany) to make it perform as an injection molding machine, by adding a rectangular cavity of dimensions 2x12x135 mm, see Figure 5.1(b). A cooling clamp is used to thermostatically cool the mold walls. In this study we consider modeling of experiments using the capillary rheometer as a necessary

step in between the MPR and an injection molding machine, since the experiments are conducted under non-isothermal conditions and the developed flow field is, like in injection molding, spatially inhomogeneous: behind the flow front, kinematics are shear dominated but near the flow front, due to the fountain flow, significant extension takes place. The post-filling stages of injection molding, in which pressure levels are high and the fluid velocity inside the cavity is low, cannot be mimicked yet by the capillary mold and thus their effect on the morphological development is here disregarded. The effect of varying injection speed is assessed using the different flow speeds summarized in Table 5.5. For all conditions the injection temperature and the temperature at the slit walls are set to 220 °C and 80 °C, respectively.

**Table 5.5:** Flow conditions for the capillary rheometer experiments.

conditions	$t_{\text{flow}}$ [s]	$v_{\text{avg}}$ [ $\text{m s}^{-1}$ ]
CA1	2	0.126
CA2	4	0.0662
CA3	8	0.03758

## 5.3 Morphological characterization by polarized optical light microscopy

### 5.3.1 MPR experiments

The morphology of the MPR samples is characterized ex-situ via polarized optical light microscopy (POLM). Micrographs are taken from thin cross-sections of 3-7  $\mu\text{m}$ , microtomed at -130 °C on the flow-thickness direction, under cross polarizers rotated +/- 45° with respect to the flow direction. The cross sections are taken from the center of the slit, see Figure 5.2. Only the samples processed at the highest flow speed conditions, MPR1 and MPR2, develop an oriented shear layer followed by a fine-grained layer, see Figure 5.3. Furthermore, the lower flow temperature of condition MPR2, significantly increases the thickness of the oriented layer. For the conditions MPR3 and MPR4 there is no development of oriented layers, only a fine-grained layer is found. For the condition MPR4 the morphological gradient across the thickness is very smooth, denoting a linear decrease in the size of spherulites towards the walls and a pronounced effect of transcrystallinity. The thickness of the oriented and fine-grained layers are for all the conditions given in Table 5.6.

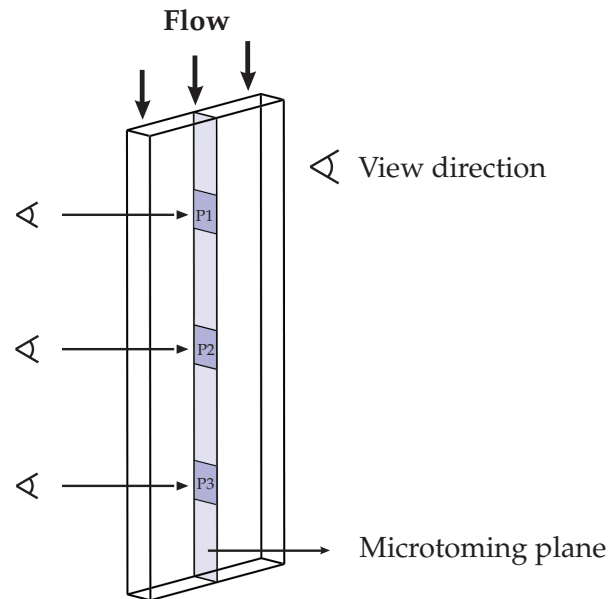


**Figure 5.2:** Layout procedure to microtome samples for optical light microscopy.

**Table 5.6:** Thickness of the oriented layers for the MPR experiments.

conditions	oriented layer [mm]	fine-grained layer [mm]
MPR1	0.07	0.20
MPR2	0.16	0.25
MPR3	-	0.20
MPR4	-	0.10

### 5.3.2 Capillary rheometer experiments

Samples are microtomed according to the same procedure explained for the MPR at three different positions along the length of the slit: close to the gate, at the middle and close to the end of the slit, see Figure 5.2. The samples are taken from the width mid-plane. For all flow-conditions the morphology is inhomogeneous exhibiting a layer type of structure with a highly oriented crystalline region. Three different layers are identified from the edge to the spherulitical core: a thin *skin* layer, a *transition* layer, and a *shear* layer that is followed by an isotropic core, see Figure 5.5.

For all flow conditions the thickness of the oriented region, composed by the skin, transition and shear layers, increases towards the middle of the slit and decreases again towards the end of the slit. Such variation is explained by the thermal and mechanical deformation experienced by the material. The skin layer, which origi-



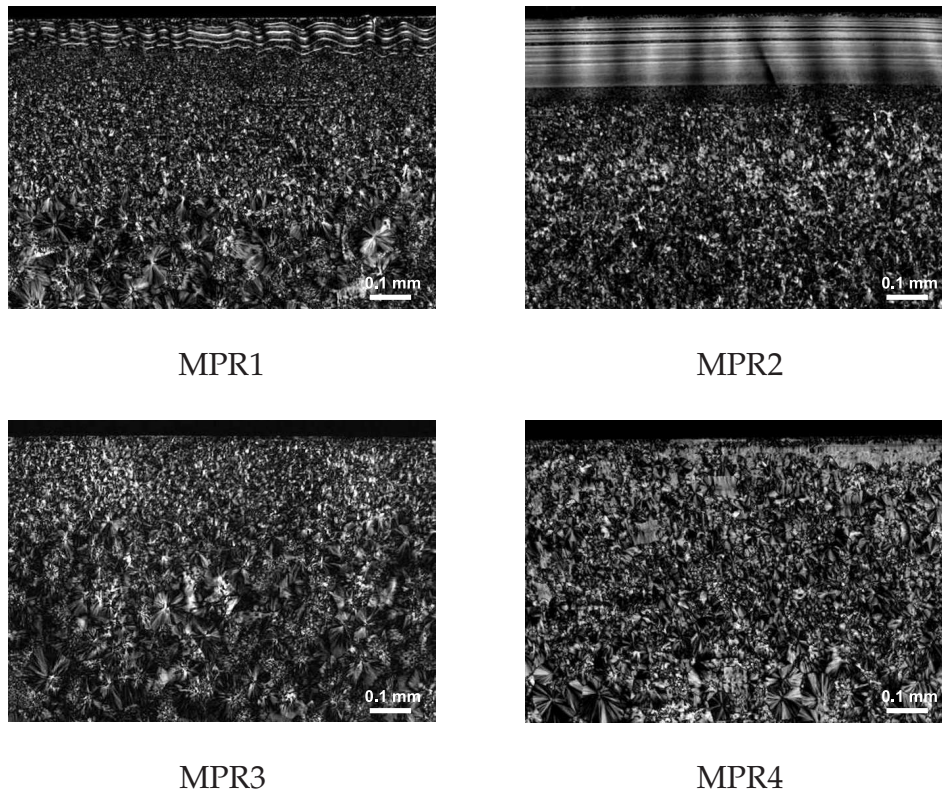


**Figure 5.3:** Polarized optical micrographs for multipass flow conditions at the center of the slit, see also Table 5.4.

nates from the deposition of stretched material in the flow front (fountain flow) that is subsequently quenched at the walls, remains constant along the slit length. However, thickness of the transition and shear layers result from the combined effect of cooling and shear deformation. Close to the gate the injection of molten material keeps the temperature relatively high, favoring the relaxation of orientation. At the middle of the slit, the material experiences a longer thermal and shear deformation history, which is reflected in the thicker oriented layers. The material that fills the end of the slit channel travels through the core region at low shear rates experiencing a short cooling and mechanical history, thus the thickness of the oriented layers decreases towards the end of the slit. The increase of injection speed results in thinner oriented layers due to the larger amount of heat transported inside the slit per unit time as well as the higher contribution from viscous dissipation, which, combined, cause a lower cooling rate. Therefore the transition from oriented crystalline layers to spherulitical is shifted towards the walls. Moreover, the cooling time during filling is also obviously decreased. Hence, at higher injection speeds the shorter relaxation times that result from lower cooling rates and shorter cooling times during filling, explain the decrease in thickness of the oriented crystalline layers.

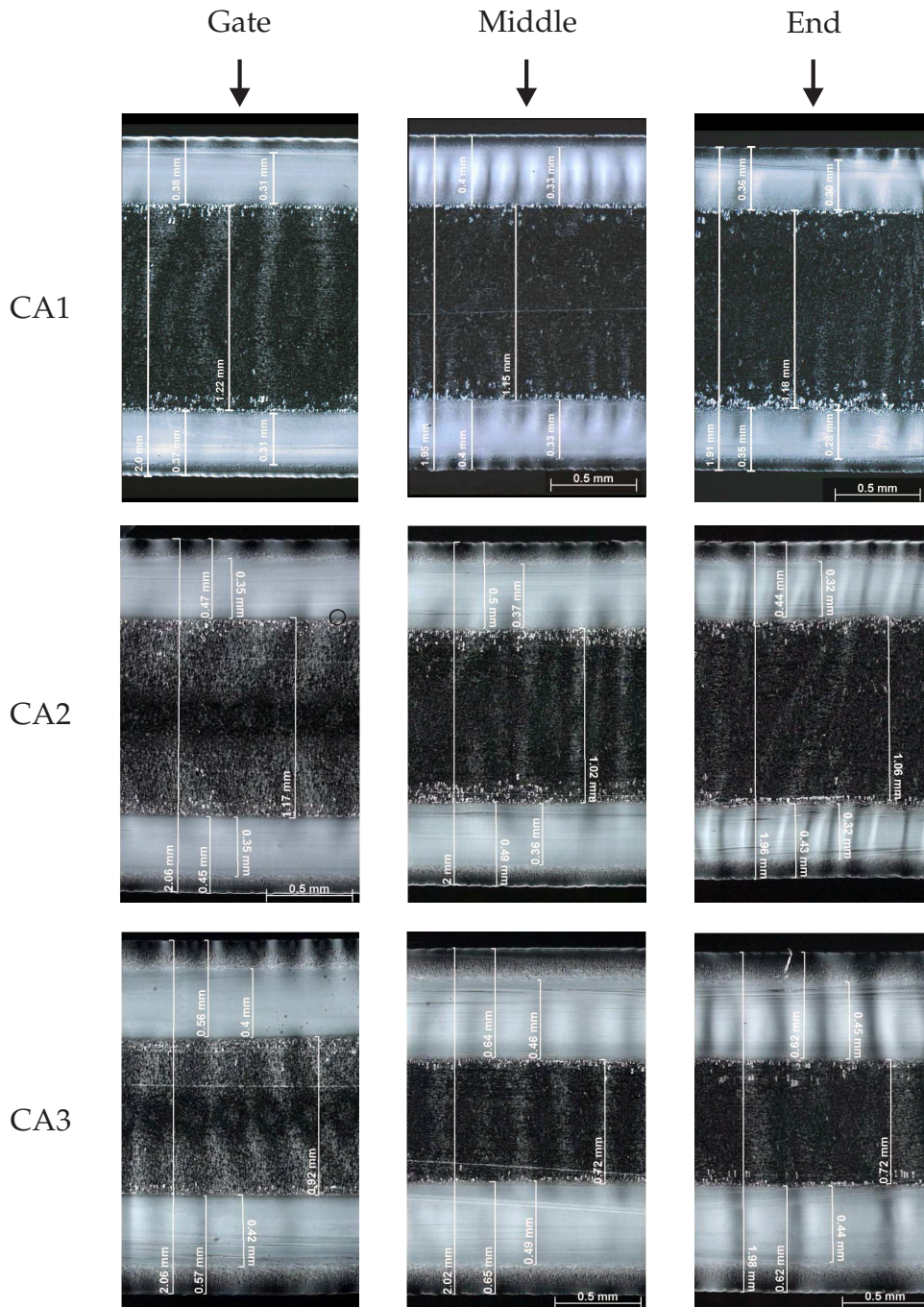
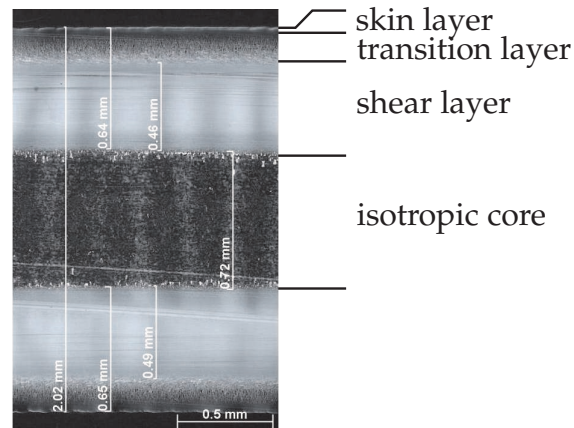


Figure 5.4: Polarized optical micrographs for capillary rheometer flow conditions at three locations along the flow slit-channel length, see also Table 5.5.

## 5.4 Computation of the flow kinematics

### 5.4.1 Viscous flow problem

In order to model the experiments of the MPR and capillary rheometer the governing equations presented in Chapter 2, Equations (2.21), (2.22) and (2.29) are solved.



**Figure 5.5:** Identification of morphological layers over a cross section. Polarized optical micrograph corresponds to flow-condition 2CA at the middle of the slit.

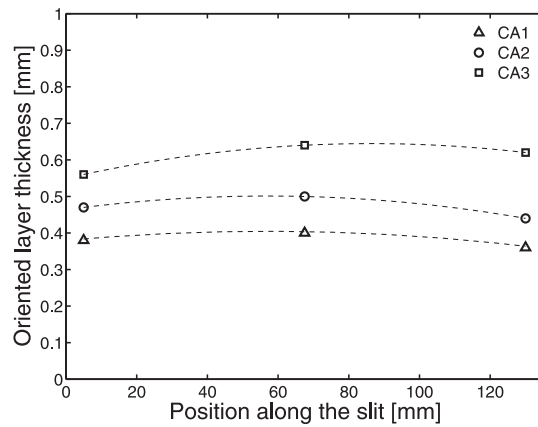


**Figure 5.6:** Symbols: thickness of the oriented layer for the capillary-flow conditions at three positions along the slit length. Lines are shown to guide the eye.

The flow kinematics are thus assumed to be determined by the kinematic boundary conditions and a generalized Newtonian description is adopted. Since we take into account the hardening effect of the crystalline structures on the viscosity, viscosity is here made dependent on temperature, the deviatoric part of the rate of deformation tensor  $\mathbf{D}$  and space filling  $\zeta_g$ :

$$\eta = \eta(T, \mathbf{D}^d, \zeta_g). \quad (5.4)$$

According to the generalized Newtonian flow description, the extra stress tensor  $\boldsymbol{\tau}$  reads:

$$\boldsymbol{\tau} = 2\eta(T, \mathbf{D}^d, \zeta_g)\mathbf{D}. \quad (5.5)$$

The viscosity dependence on temperature and shear rate is described by a Cross model:

$$\eta = \frac{\eta_0(a_T)}{1 + (K(a_T)\dot{\gamma})^{(1-n)}}, \quad (5.6)$$

with the shift factor  $a_T$  given by the WLF equation (3.14). The values of the model parameters and the WLF constants are listed in Table 5.2.

### Crystallization effects on the flow

The growth of crystalline structures increases the melt viscosity (hardening), and during the filling stage this effect can become important. Lamberti et al. [71] give a review on experimental studies concerning the viscosity hardening of polymer melts during crystallization. A list of available models to describe changes in rheology with the increase of crystallinity was given, distinguishing suspension-based from empirical models. The numerous different models illustrate the lack of understanding how crystallization kinetics and structural changes determine the viscosity hardening evolution. The authors proposed a new experimental method that combines differential scanning calorimetry, DSC, and rheometry, to determine the change in viscosity induced by the degree of space filling  $\xi_g$ . They found that the influence of crystallinity on viscosity can be described by a shift factor,  $a_{\xi}(\xi_g)$ , which is equivalent to adopt a time-hardening superposition. Hence, the viscosity is shifted according to the temperature and degree of space filling.

The effect of shear flow on the rheology of viscoelastic suspensions filled with rigid particles was analyzed by Hwang et al. [45] using advanced finite-element methods, however their method was limited to 2-D flows. Even though the usefulness of such analysis in providing a more comprehensive insight of the rheological phenomena involved, they are computationally very expensive. This is certainly true when going to 3-D simulations, see Hwang et al. [46]. Thus, simple suspension models that can relate rheological properties of melts with the underlying crystalline morphology are more attractive to implement in injection molding codes. In a recent publication Steenbakkens and Peters [112] reviewed early work on suspension modeling and applied a generalized self-consistent method [17] to describe the evolution of linear viscoelastic properties of crystallizing melts during crystallization and its completion. Their model allows to incorporate particles with different shapes, discriminating oriented from nonoriented crystals. Spherulites are represented by spheres and shish-kebabs by cylinders. Additionally, the mechanical properties of the particles and the matrix are transient and dependent on the ongoing microstructural changes. The approach of Lamberti et al. [71] is a special case; crystalline particles are rigid and only space filling is accounted for, i.e. no influence of oriented structures.

Here, we follow the model proposed by Lamberti et al. [71], in which viscosity is shifted according to the computed degree of space filling  $\xi_g$ . The generalized New-

tonian viscosity then becomes:

$$\eta = \eta(T, \dot{\gamma}, \xi_g) = \eta_0(\dot{\gamma} \cdot a_T \cdot a_\xi) \cdot a_T \cdot a_\xi, \quad (5.7)$$

with the shift factor  $a_\xi$  given by:

$$a_\xi(\xi_g) = 10^{a \cdot \xi_g^b}, \quad (5.8)$$

where  $a$  and  $b$  are defined as hardening parameters. The authors used their model to describe experiments conducted with an iPP, ( $M_w = 350 \text{ kg mol}^{-1}$ ,  $M_w/M_n = 5.3$ ), very similar to iPP HD120MO, see Table 5.1, and found  $a = 3.875$  and  $b = 1.236$ . The evolution of the viscosity hardening shift factor  $a_\xi$  with the degree of space filling is shown in Figure 5.7.

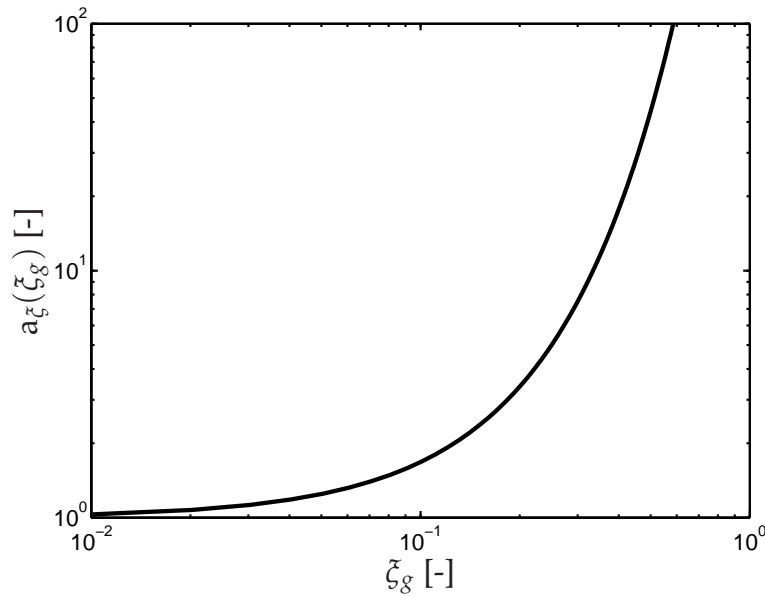


**Figure 5.7:** Hardening shift factor  $a_\xi(\xi_g)$  versus degree of space filling  $\xi_g$ .

## Heat of crystallization

The latent heat of crystallization is incorporated as a source term,  $\rho H \dot{\xi}$ , in the energy equation, with  $H$  the heat of crystallization and  $\dot{\xi}$  the rate of change of the degree of crystallinity. Heat conduction is described by Fourier's law with an isotropic heat conduction coefficient. Neglecting thermal radiation and assuming compression effects to be negligible (see Chapter 2, the energy balance reads:

$$\rho c_p \dot{T} = 2\eta \mathbf{D} : \mathbf{D} + \nabla \cdot (\lambda \nabla T) + \rho H \dot{\xi}. \quad (5.9)$$

## 5.4.2 Boundary conditions

### MPR

To make the problem computationally less expensive we approximate the MPR geometry by a 2-D problem in which the vorticity plane is depicted. A periodic channel is defined, see Figure 5.8, and a mass flux is prescribed at the inflow boundary  $\Gamma_p$ . Dirichlet boundary conditions are used to impose a no-slip condition at the walls,  $\Gamma_w$ :

$$\mathbf{u} = \mathbf{0} \quad \forall \mathbf{x} \in \Gamma_w. \quad (5.10)$$

The wall temperature is set equal to the injection temperature, thus:

$$T = T_p(\mathbf{x}, t) \quad \in \Gamma_p \cup \Gamma_w, \quad t > 0. \quad (5.11)$$

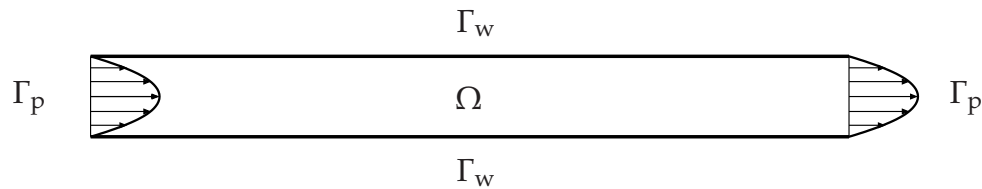


Figure 5.8: Periodic computational domain for the MPR flow simulations.

### Capillary rheometer

We adopt a 2-D approximation of the original problem in which the flow history is only computed inside the slit. Such an approach avoids the solid-fluid interaction problem of the moving piston, considerably simplifying the numerical methods required to compute the flow kinematics. Local extensional effects at the contraction region are thus assumed negligible.

The position of the flow front is determined from the solution of the melt velocity field. To capture the polymer/air interface we employ the front capturing method introduced in Chapter 2, in which the convection equation, Equation (2.41), gives the evolution of the material label distribution. As initial condition the material label field,  $c$ , is set to zero over the entire domain  $\Omega$ , and at the inlet  $\Gamma_e$  the following boundary conditions are assigned:

$$c(\mathbf{x}, t = 0) = 0, \quad \mathbf{x} \in \Omega, \quad (5.12)$$

$$c(\mathbf{x}, 0 < t < t_{\text{fill}}) = 1, \quad \mathbf{x} \in \Gamma_e. \quad (5.13)$$

The boundary conditions in the computational domain  $\Omega$ , Figure 5.9, are specified

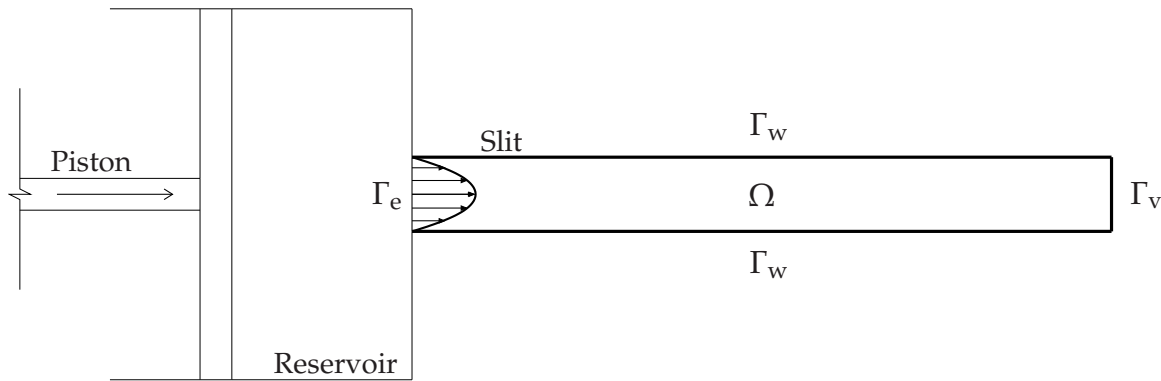


**Figure 5.9:** Computational domain for the capillary rheometer flow simulations.

at  $\Gamma_e$ ,  $\Gamma_w$  and  $\Gamma_v$ , designating the mold entrance, mold walls, and the air vents respectively. A fully developed velocity profile at the slit inlet  $\Gamma_e$  is assumed. At the mold walls we employ dynamic boundary conditions to change from slip to no-slip condition depending on the material label  $c$  at the wall, see Section 2.1.4. The thermal boundary conditions are specified also according to Section 2.1.4. Dirichlet boundary conditions Equation (2.49) are prescribed at the walls.

## 5.5 Modeling crystallization

Under the combined effect of cooling and flow-induced molecular deformation, the resulting material morphology upon crystallization combines both spherulitical and fibrillar oriented structures. Both have to be taken into account if a realistic description of the final morphology is envisaged.

### 5.5.1 Quiescent crystallization

Spherulitical structures develop under quiescent conditions, their number and size depend on the cooling history and on the concentration of nucleating agents. To model this we use the Schneider rate equations [24], which are based on the Kolmogoroff-Avrami equation [5, 6]. They provide a complete picture of the morphology, in terms of number of spherulites, their radius, surface and volume, and

consist of a set of nested differential equations that reads:

$$\dot{\phi}_3 = 8\pi\alpha \quad (\phi_3 = 8\pi N), \quad (5.14)$$

$$\dot{\phi}_2 = G\phi_3 \quad (\phi_2 = 4\pi R_{\text{tot}}), \quad (5.15)$$

$$\dot{\phi}_1 = G\phi_2 \quad (\phi_1 = S_{\text{tot}}), \quad (5.16)$$

$$\dot{\phi}_0 = G\phi_1 \quad (\phi_0 = V_{\text{tot}}), \quad (5.17)$$

in which  $\phi_0$  is the undisturbed total volume  $V_{\text{tot}}$  of the spherulites per unit volume,  $\phi_1$  is the total surface  $S_{\text{tot}}$  of the spherulites per unit volume,  $\phi_2$  is  $4\pi$  times the sum of the radii  $R_{\text{tot}}$  of the spherulites per unit volume,  $\phi_3$  is  $8\pi$  times the number of the spherulites  $N$  per unit volume,  $\alpha = \alpha(T, p)$  is the nucleation rate and  $G = G(T, p)$  the crystal growth rate. In order to correct for impingement, two different models can be employed, the Avrami model [5, 6],

$$-\ln(1 - \bar{\zeta}_g) = \phi_0, \quad (5.18)$$

or the Tobin model [118],

$$\frac{\bar{\zeta}_g}{1 - \bar{\zeta}_g} = \phi_0. \quad (5.19)$$

The degree of crystallinity  $\bar{\zeta}$  can be obtained by multiplying the degree of space filling  $\bar{\zeta}_g$  with the degree of crystallinity within each spherulite (maximum amount of crystallized material). Expressions for the nucleation density  $N(T, p)$  and growth  $G(T, p)$ , should accurately describe the kinetics of quiescent crystallization dependence on both temperature and pressure.

### Implementation and validation

In [95] the rate equations are validated on experimental results obtained by Malkin et al. [79], in which a polyamide 6 plate of 20 mm was quenched from 478 K to 453 K. During the experiment the temperature distribution over the thickness of the sample was monitored until completion of crystallization. Throughout the crystallization process the new calculated degree of space filling was used to update the source term of the energy equation  $\rho\dot{\zeta}H$ . The calculated temperature over the plate thickness, notably its increase due to the heat released during crystallization, was correctly predicted in [95]. The number of spherulites was taken constant;  $N = 6.10^{11} \text{ m}^{-3}$ , and the crystal growth rate described by:

$$G = \frac{G_0}{L} \exp\left[-\frac{c_d}{T-T_g} - \frac{CT_m}{T(T_m-T)}\right], \quad (5.20)$$

in which  $T$  is the temperature,  $T_m$  the melting temperature and  $T_g$  the glass transition temperature. The values used in formula (5.20) are listed in Table 5.7 and the material properties are given in Table 5.8. The heat of crystallization  $H$  and the maximum



**Table 5.7:** Parameters of the crystal growth rate model for polyamide 6.

$G_0$	$10^{-2}$	$[\text{m s}^{-1}]$
$C_d$	2070	$[\text{K}]$
$C$	265	$[\text{K}]$
$L$	$2.85 \cdot 10^{-5}$	$[-]$

**Table 5.8:** Material properties of polyamide 6.

$c_p$	2136.9	$[\text{K kg}^{-1} \text{K}^{-1}]$
$\lambda$	0.21	$[\text{W m}^{-1} \text{K}^{-1}]$
$T_g$	330	$[\text{K}]$
$T_m$	506	$[\text{K}]$
$H$	192474	$[\text{J kg}^{-1}]$
$V_\infty$	0.35	$[-]$

degree of crystallinity  $V_\infty$  are taken from Zuidema [136]. We use the Tobin model Equation (5.19) to correct the computed undisturbed spherulitical volume and find the corresponding degree of space filling. Figure 5.10(a) shows the prescribed temperature profile at the wall, and Figure 5.10(b) the temperature values at the center of the sample as measured by Malkin et al. [79]. The predicted results are in very good agreement with the experimental ones. Figures 5.10(c) and 5.10(d), compare the degree of space filling at the surface and at the center of the slab with predictions by Schneider et al. [95]. The results are in good agreement.

### Quiescent crystallization kinetics in iPP HD120MO

Van der Beek [121] performed quiescent crystallization experiments in a dilatometer, measuring the specific volume of iPP HD120MO for different cooling rates at a pressure of 40 MPa. He could predict the evolution of the specific volume measured during cooling, using the Schneider rate equations and a state equation in which the dependence of density on the volume fraction of crystalline and amorphous material was taken into account. The spherulitical growth rate  $G(T)$  and the number of nuclei per unit volume  $N(T)$  were determined from polarized optical microscopy experiments. To describe specific volume at elevated pressures, both  $G(T)$  and  $N(T)$  were adapted in the following way:

$$G(T, p) = G_{\max} \exp[-b(T - T_{\text{ref}} - f_g(p))^2], \quad (5.21)$$

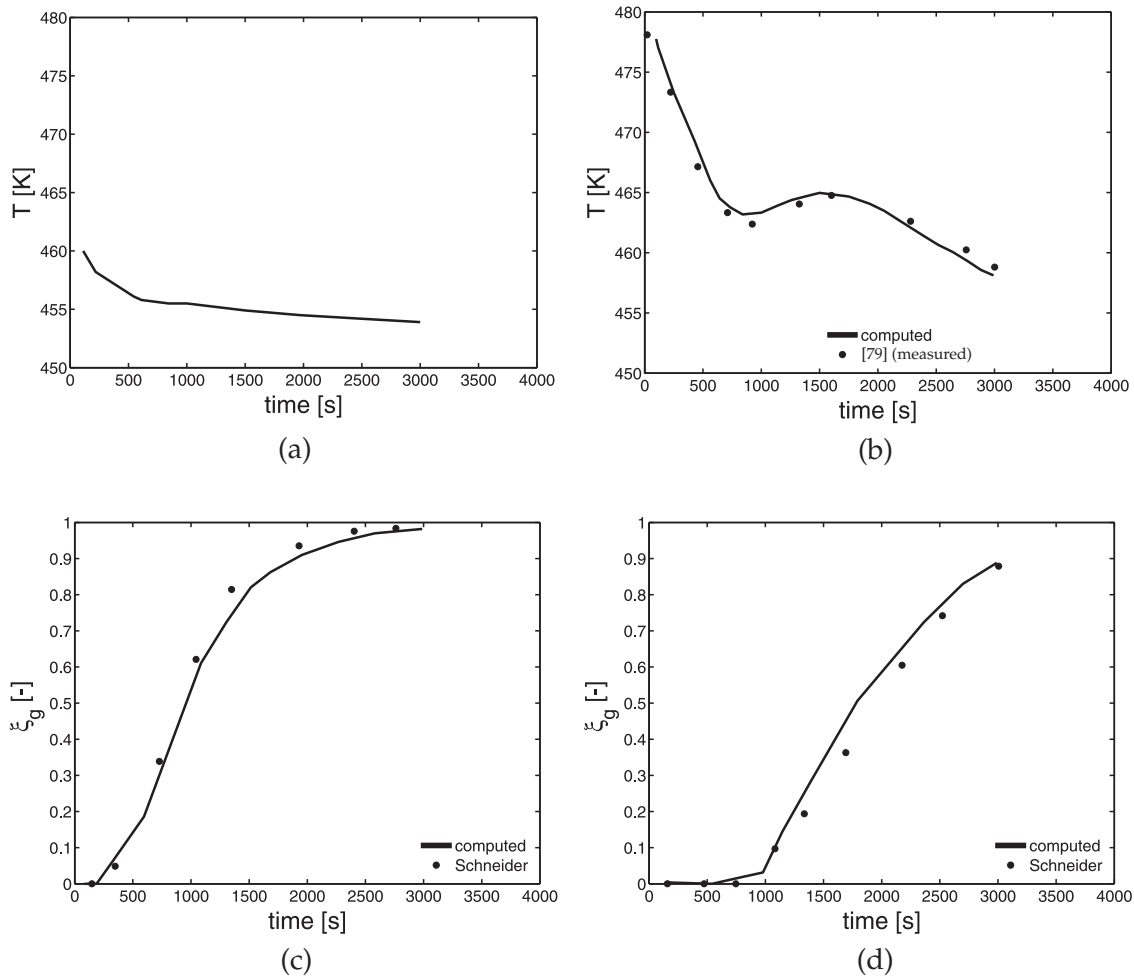


**Figure 5.10:** (a) Prescribed temperature at the wall according to Schneider et al. [95]. (b) Solid line: computed temperature at the center of the slab; dots: temperature values measure by Malkin et al. [79]. (c) Solid line: predicted  $\zeta_g$  at the wall of the slab; dots: computed results of Schneider et al. [95]. (d) Solid line: predicted degree of space filling  $\zeta_g$  at the center of the slab; dots: computed results by Schneider et al. [95].

$$N(T, p) = 10^{[n_0 + n_1(T - f_n(p))]}, \quad (5.22)$$

where

$$f_i = p_{i0}\Delta p + p_{i1}\Delta p^2 \quad i = g, n, \quad (5.23)$$

$$\Delta p = p - p_{\text{ref}}. \quad (5.24)$$

The parameters used in equations (5.21)-(5.23) are taken from Van der Beek [121] and given in Table 5.9. Only for the highest cooling rate used ( $32.5 \text{ }^\circ\text{C s}^{-1}$ ) the model gave a poor result. The nucleation curve and the growth rate curve at atmospheric pressure are given in Figures 5.11(a) and 5.11(b), respectively.

**Table 5.9:** Model parameters for the spherulitical growth rate  $G(T, p)$  and effective number of nuclei  $N(T, p)$  for iPP (HD120MO, Borealis).

$G_{\max}$	$2.9669 \cdot 10^{-6}$	$[\text{m s}^{-1}]$
$b$	$1.3000 \cdot 10^{-3}$	$[\text{°C}^{-1}]$
$T_{\text{ref}}$	$9.00 \cdot 10^1$	$[\text{°C}]$
$p_{g0}$	$7.0333 \cdot 10^{-8}$	$[\text{K Pa}^{-1}]$
$p_{g1}$	$-4.7000 \cdot 10^{-15}$	$[\text{K Pa}^{-2}]$
$p_{n0}$	$2.7000 \cdot 10^{-7}$	$[\text{K Pa}^{-1}]$
$p_{n1}$	0.0	$[\text{K Pa}^{-2}]$
$n_0$	$1.9067 \cdot 10^1$	$[\text{m}^{-3}]$
$n_1$	$-4.9800 \cdot 10^{-2}$	$[\text{m}^{-3} \text{K}^{-1}]$
$P_{\text{ref}}$	$1.0000 \cdot 10^5$	$[\text{Pa}]$

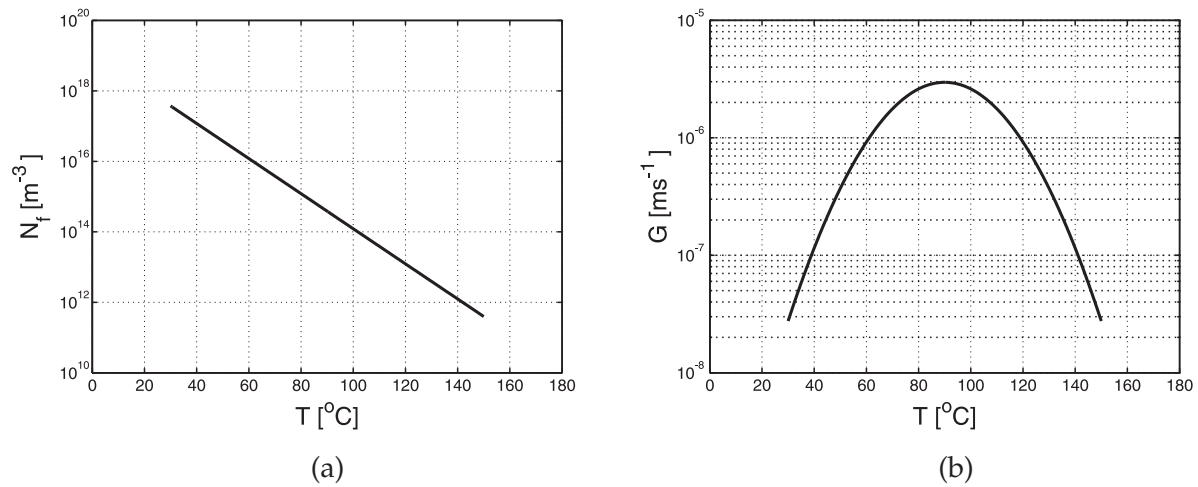


**Figure 5.11:** (a) Quiescent nucleation rate  $N_q(T, p)$  curve. (b) Spherulitical growth rate  $G(T, p)$  curve.

Regarding the heat of crystallization  $H$ , from literature it is known that for iPP the value lies between 170 up to 273  $\text{KJ kg}^{-1}$  for a pure crystal. In this study we take it to be 170  $\text{KJ kg}^{-1}$ . The degree of crystallinity  $\zeta$  is found by multiplying the degree of space filling  $\zeta_g$  with a factor indicating the maximum attainable degree of crystallinity  $V_{\infty}$ , which we take equal to 0.5.

### 5.5.2 Modeling flow effects on crystallization

The ideas contained in the model proposed by Zuidema et al. [137], and in the recent model developed by Steenbakkers and Peters [113], for flow-induced crystallization, are here combined and adapted in a model to describe the process of flow-induced nucleation and growth of flow-induced crystals.

We start by considering the total number of nuclei  $N_t$  to be the result of heterogeneous (thermally activated) nucleation  $N_q$  and homogeneous (flow-induced) nucleation  $N_f$ :

$$N_t = N_q + N_f, \quad (5.25)$$

The number of quiescent nuclei at a given temperature and pressure is found solving Equations (5.22) and (5.23). The flow-induced nucleation rate is assumed to be a function of the stretch of the longest chains present in the melt. This assumption has been validated by [113] and [125], who have shown that the stretch,  $\Lambda$ , of the high molecular weight chains drives flow-induced nucleation. It is envisioned that the stretch of the high end tail of the molecular weight distribution increases the number of aligned chain segments whose conformation is closer to the crystalline state. Furthermore, the growth of oriented crystals (shish-kebabs) was found to occur only when a critical molecular stretch was exceeded [125], implying that molecular orientation by itself does not suffice to induce shish growth. Following these ideas, the flow-enhanced nucleation rate was described, Steenbakkers and Peters [113], using a fourth-order dependence on the molecular stretch of the slowest relaxation mode only:

$$\dot{N}_f = g_n \left( \Lambda^4 - 1 \right), \quad (5.26)$$

in which  $g_n$  is a scaling parameter. Some experimental observations have been reported that a saturation limit exists beyond which the rate of flow-induced nucleation becomes zero [81]. Hristova and Peters [42] measured the number of flow-induced nuclei in iPP HD120MO as a function of shear rate in a Linkam shear cell. The authors identified different saturation levels of the total number of flow-induced nuclei created, depending on the shear rate applied. For the highest shear rate applied, a saturation value,  $N_{f,\max}$ , equal to  $3.1 \cdot 10^{14} \text{ m}^{-3}$  was measured. To include an asymptotic limit determined by  $N_{f,\max}$  in the expression for the rate of flow-induced nucleation we modify Equation (5.26), which becomes:

$$\dot{N}_f = g_n \left( \Lambda^4 - 1 \right) \left[ 1 - \frac{N_f}{N_{f,\max}} \right]. \quad (5.27)$$

Even though experiments do suggest the saturation level to be dependent on the shear rate  $N_{f,\max}(\dot{\gamma})$ , due to scarceness of experimental data, we take  $N_{f,\max}$  constant and equal to the value measured by Hristova at the highest shear rate.

Following the approach of Zuidema et al. [137] the number of flow-induced nuclei are assumed to act as physical cross links in the melt. Hence, the relaxation time of the high molecular weight (HMW) chains in the melt is made a linear function of the number of flow-induced nuclei:

$$\tau_j = a_T \tau_{j0} (1 + \alpha N_f), \quad (5.28)$$

in which  $\alpha$  is a coupling parameter, which expresses the addition of physical crosslinks to the melt. However, this coupling requires some caution, since the cross-linking effect of the flow-induced nuclei on the relaxation time of the HMW chains, makes it almost impossible to relax the orientation and stretch of these molecules, with the consequence of flow-induced crystallization proceeding up to unrealistic time scales. To circumvent this, we introduce a pre-factor  $\delta$  in Equation (5.27), which sets the rate of flow-induced nucleation to zero if the flow is stopped. Experimental evidences might support the use of such a pre-factor. It has been observed in short term shear flows under isothermal conditions, that all flow-induced crystals grown possess the same size, indicating that the onset of crystal growth is triggered when the flow is stopped. If flow-induced nucleation would continue after the flow, one would expect a distribution in size of flow-induced crystals. Thus, the final equation for flow-induced nucleation reads:

$$\dot{N}_f = \delta g_n (\Lambda^4 - 1) \left[ 1 - \frac{N_f}{N_{f,\max}} \right], \quad (5.29)$$

with

$$\delta = 1 \quad \text{if} \quad \dot{\gamma} > 0, \quad (5.30)$$

$$\delta = 0 \quad \text{if} \quad \dot{\gamma} = 0. \quad (5.31)$$

Both quiescent and flow-induced nuclei are assumed to grow radially, and therefore the total number of nuclei  $N_t$  obtained from Equation (5.25) is given as input for the Schneider rate equations:

$$\dot{\phi}_3 = 8\pi\alpha \quad (\phi_3 = 8\pi N_t). \quad (5.32)$$

Based on the experimental evidence that a deformation threshold needs to be surpassed to change from the isotropic growth regime to the fibrillar-oriented regime, we expect that flow-induced nuclei can only grow out as cylinders (shish kebabs) once a critical threshold in terms of molecular stretch  $\Lambda_{\text{crit}}$  is overcome. Thus, at an early stage flow-induced nuclei are envisioned as spheres whose morphological evolution will depend on the flow conditions. In Figure 5.12, our model for the morphological development of flow-induced nuclei is illustrated. The nucleation process starts with a stretch-induced bundle of oriented chain segments which is assumed to be an embryonic form of a nucleus, see [113]. If a critical stretch is reached, a transition from isotropic to oriented (fibrillar) growth is assumed to occur, here denoted as regime I and II, respectively. Only nuclei created after the critical

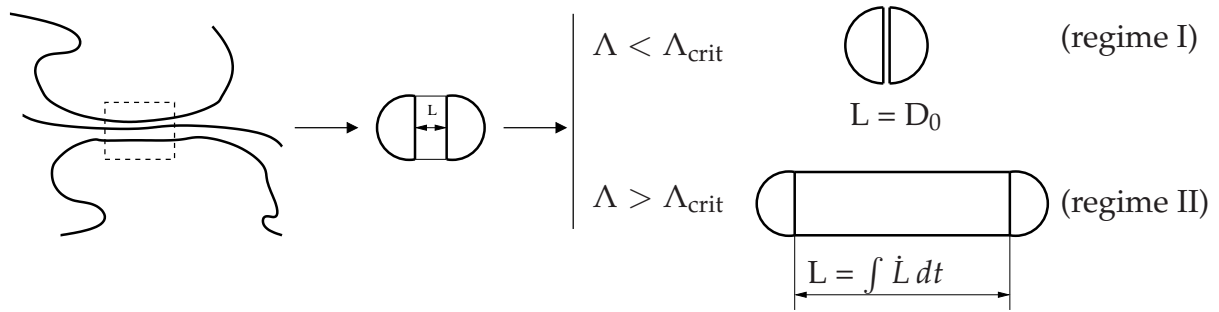


Figure 5.12: Model for the nuclei growth.

stretch is reached are assumed to grow into shish-kebabs. The growth mechanisms for isotropic (spherulites) and oriented (shish-kebabs) crystalline structures are illustrated in Figure 5.13.

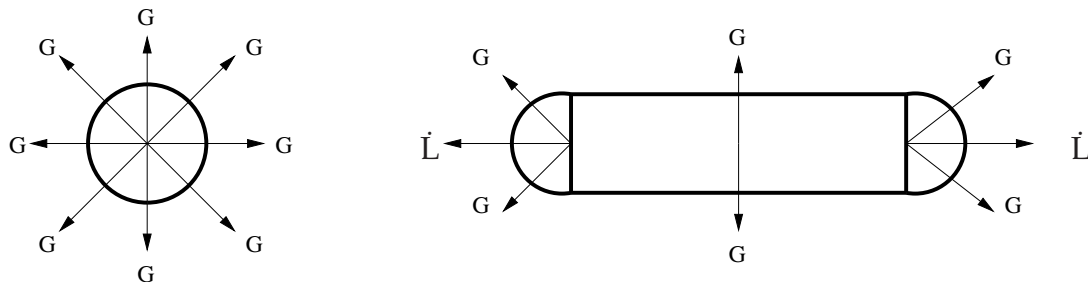


Figure 5.13: Growth of isotropic and oriented crystalline structures.

The radial growth  $G(T, p)$ , given by Equation (5.21), drives the growth of spherulitic crystalline structures and the growth of kebabs, which is depicted by the model as an increase in diameter of the shish (cylinder). The cylindrical representation of a shish-kebab is only valid if  $\dot{L} \gg G$ , which, at this moment, we state as an assumption. An equation for shish-growth (cylindrical length)  $\dot{L}$  is specified next.

The exact mechanisms involved in the growth of a shish are still unknown and a matter for debate, however recently new experimental findings [65] provide new insight. From elaborated experiments involving small-angle neutron scattering with deuterium labeling of specific chain lengths, Kimata et al. [65] could identify the role of long chains in the processes of shish formation and growth. It was observed that shish, as opposed to the established belief, are not dominated by long chains, but are instead made of a broad distribution of chain lengths. The authors propose a physical mechanism in which long chains play an important role in shish formation, but are not the dominant species in the shish growth. According to their explanation, the fast growth of a shish  $\mathcal{O}(\mu\text{s}^{-1})$  does not give time to segregate chains from the bulk into the shish: *‘long chains greatly enhance the propagation velocity of a shish, with the kinetic*

consequence that all lengths of chains become incorporated as the shish advances'. Following their observations we assume the growth of a shish to be a non-selective process, in which all chains in the melt, regardless of their molecular weight, can participate. The average conformation of the chains, in terms of orientation and stretch is here assumed to influence the growth rate. Accordingly, we write the shish-growth rate equation  $\dot{L}$  as:

$$\dot{L} = g_1 J_2(\mathbf{B}_{e,\text{avg}}^d); \quad \text{for } \Lambda > \Lambda_{\text{crit}}, \quad (5.33)$$

in which  $J_2(\mathbf{B}_{e,\text{avg}}^d)$  is the second invariant of the deviatoric elastic Finger tensor of a mode, representative of the whole molecular weight distribution, which is added to the slow Rolie-Poly mode. The relaxation time of this mode is calculated by

$$\tau_{d,\text{avg}} = \frac{\sum_{d,i} G_i \tau_{d,i}^2}{\sum_i G_i \tau_{d,i}}, \quad (5.34)$$

which is the viscosity-averaged relaxation time. Using the viscoelastic data listed in Table 5.2 we find the viscosity-averaged relaxation time  $\tau_{d,\text{avg}}$  equal to 12.2 s. Thus, a two-mode Rolie-Poly model is used, in which one mode represents the long chains and the other an average contribution of all chains. In Equation (5.33),  $g_1$  is a scaling parameter for the influence of  $J_2$  on the thread-like growth of the nuclei. By considering an average relaxation time of the melt relaxation spectrum, we assume the growth of a shish to be a process in which all molecular chains participate, favored by the combined effect of molecular stretch and orientation, which is conveniently expressed by  $J_2(\mathbf{B}_e^d)$ . From the growth rate of shish it is possible to calculate the total undisturbed length, surface and volume per unit volume, employing the rate equations of Eder [24], which read:

$$\dot{\psi}_2 = 4\pi N_f \dot{L} = 4\pi N_{f,\text{ori}} g_1 J_2(\mathbf{B}_e^d), \quad (5.35)$$

$$\dot{\psi}_1 = G \psi_2 \quad (\psi_1 = S_{\text{tot}}), \quad (5.36)$$

$$\dot{\psi}_0 = G \psi_1 \quad (\psi_0 = V_{\text{tot}}), \quad (5.37)$$

in which  $\psi_0$  is the total volume of shish-kebabs per unit volume,  $\psi_1$  the total surface  $S_{\text{tot}}$  of the shish-kebabs per unit volume and  $\psi_2$  is  $4\pi$  times the total length  $L_{\text{tot}}$  of the shish per unit of volume times the number of flow-induced nuclei created with  $\Lambda > \Lambda_{\text{crit}}$ , which we denote as  $N_{f,\text{ori}}$ . Since the model gives the undisturbed spherulitical and oriented crystalline volume,  $\phi_0$  and  $\psi_0$ , respectively, we need to correct for impingement. We adopt the Avrami and Tobin model Equations (5.18) and (5.19) to take into account the contribution of both spherulitical and oriented crystalline structures. The modified models read:

$$-\ln(1 - \zeta_g) = \phi_0 + \psi_0; \quad \frac{\zeta_g}{1 - \zeta_g} = \phi_0 + \psi_0. \quad (5.38)$$

The scaling parameters  $g_n$  and  $g_1$ , are made temperature dependent according to time

temperature superposition. Hence, at a certain temperature they are shifted with  $a_T$  to a reference temperature:

$$g_n(T) = g_{n0}(a_T), \quad (5.39)$$

$$g_l(T) = g_{l0}(a_T). \quad (5.40)$$

The real total shish length per unit volume, taking into account impingement, and the real number of flow-induced nuclei per unit volume, taking into account impingement, can be directly found by solving the following equations:

$$\dot{N}_{f,\text{real}} = \delta g_n \left( \Lambda^4 - 1 \right) \left[ 1 - \frac{N_f}{N_{f,\text{max}}} \right] (1 - \zeta_g), \quad (5.41)$$

and

$$\dot{L}_{\text{tot,real}} = N_{f,\text{real}} g_l J_2(B_{e,\text{avg}}^d) (1 - \zeta_g), \quad (5.42)$$

in which  $N_{f,\text{real}}$  denotes the real number of flow-induced nuclei per unit volume and  $L_{\text{tot,real}}$  the real total shish length per unit volume.

### Flow-induced crystallization parameters

The creation of point-like nuclei during flow is governed by the three parameters:  $g_n$  and  $N_{f,\text{max}}$  in Equation (5.29) and  $\alpha$  in Equation (5.28). Using a model in which inactive nuclei (precursors) are created during flow, and activated after the flow is stopped, where the molecular conformation relaxes, [113] obtained  $g_{n0} = 6.04 \times 10^5 \text{m}^{-3} \text{s}^{-1}$ ,  $N_{f,\text{max}} = 3.1 \times 10^{14} \text{m}^{-3}$ , and  $\alpha = 3.98 \times 10^{-8} \text{m}^3$  by fitting flow-enhanced nucleation densities in short-term shear experiments, which were determined by optical microscopy. In the simulations discussed here, the distinction between precursors and nuclei is not convenient. However, with the addition of the pre-factor  $\delta$  to Equation (5.27) the current model mimics the model of Steenbakkers and Peters and therefore their parameters are used.

To determine the shish growth parameter  $g_{l0}$ , the flow-induced crystallization model is combined with a suspension model, Steenbakkers and Peters [112], and applied to the rheological measurements reported in [41], after short-term shear flow. Figure 5.14 shows that for  $g_{l0} = 1.0 \times 10^{-7} \text{ms}^{-1}$ , the onset time of the increase of  $G'(t)$  is captured for two of the four shear times, but is overpredicted for the shortest and underpredicted for the longest shear time. The shape of  $G'(t)$  corresponds reasonably well with the experimental curves. The best agreement between model results and the experimental curves was found by setting the critical molecular stretch  $\Lambda_{\text{crit}} = 40 [-]$ , beyond which the onset of the oriented growth regime occurs (regime II), see Figure 5.12.



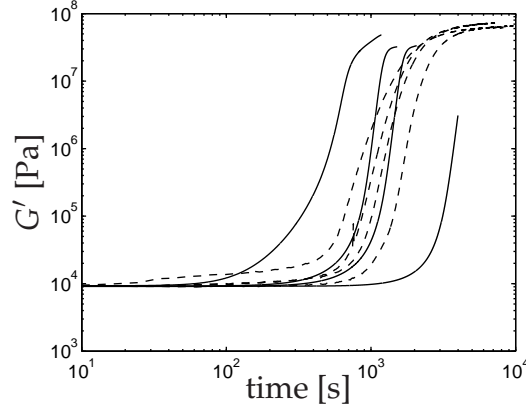


**Figure 5.14:** Calculated (solid lines) and measured (dashed lines) storage modulus after different shear flows ( $\dot{\gamma} = 30 \text{ s}^{-1}$  and  $t_s = 2, 5, 6$  and  $7 \text{ s}$ ) at  $138 \text{ }^\circ\text{C}$ , in [41].

### Stress problem

The linear viscoelastic behavior of the material is described by a seven-mode Maxwell model, see Table 5.2. The Rolie-Poly model [76] is used to calculate the part of the nonlinear viscoelastic response, necessary to solve the flow-induced crystallization problem. Namely, the stretch of the longest chains in the melt  $\Lambda_{\text{HMW}}$  and the second invariant of the deviatoric part of the elastic Finger tensor of the viscosity-averaged mode  $J_2(\mathbf{B}_{e,\text{avg}}^d)$ . The Rolie-Poly model was developed for the rheology of linear polymers and results of the model show a good agreement with rheological measurements in steady and transient regimes in both shear and extension flows. The model is of the differential type and its single-mode version was already given by Equation (3.3) in Chapter 3. The deviatoric part of the elastic Finger tensor follows from:

$$\mathbf{B}_e^d = \mathbf{B}_e - \frac{1}{3} \text{tr}(\mathbf{B}_e) \mathbf{I}. \quad (5.43)$$

The molecular stretch  $\Lambda$  follows from:

$$\Lambda = \sqrt{\frac{\text{tr}(\mathbf{B}_e)}{3}}. \quad (5.44)$$

Each term of Equation (3.3) addresses a specific molecular mechanism, such as chain reptation, chain stretch and convective constraint release, which makes this model particularly physically intuitive [76]. In the model two time scales are of importance:  $\tau_{d,i}$  the disengagement (reptation) times, and the Rouse (stretching) times  $\tau_{R,i}$ . The disengagement times are obtained from oscillatory shear measurements and listed in Table 5.2. Besides the Rouse times  $\tau_{R,i}$ , this model contains two nonlinear parameters, governing the stretch dependence of relaxation via convective constraint release, a pre-factor  $\beta \in [0, 1]$  and an exponent  $\delta < 0$ ; see Equation (3.3). For higher strain rates

the Rolie-Poly model, in its single mode form, produces a faster stress growth when compared to the full theory [76]. The explanation given by the authors, is that the full theory contains a spectrum of stretch-relaxation times, reflecting different parts of the chain, where as the single mode equation assumes uniform stretch. To compensate for the over prediction of the steady-state stress at large rates, the authors advise to set  $\beta = 0$ . Uniaxial viscosity measurements, supplied by Borealis, are used to determine the Rouse times. The strain rates  $\dot{\epsilon} = 0.3 \text{ s}^{-1}$ ,  $\dot{\epsilon} = 1 \text{ s}^{-1}$ ,  $\dot{\epsilon} = 3 \text{ s}^{-1}$ , and  $\dot{\epsilon} = 10 \text{ s}^{-1}$  were applied at a constant temperature,  $T = 180 \text{ }^\circ\text{C}$ .

As stated before, flow-enhanced nucleation rates can be described well by a fourth-order dependence on the stretch of the slowest mode only, see (5.26). Since the molecular conformations of different modes in the Rolie-Poly model are not coupled, only the dynamics of the slowest mode itself contributes to flow-enhanced nucleation. Therefore, although the uniaxial viscosity data can be fitted by different sets of Rouse times, we are only interested in obtaining a unique value for the longest Rouse time,  $\tau_R$ . This is accomplished by using the non-stretching Rolie-Poly equation for all modes except for the slowest. The only remaining free parameter is then found by fitting the model to the data for the two lowest strain rates:  $\tau_R = 2.49 \text{ s}$ . Its uniqueness is confirmed by starting from different initial values in the fitting routine. The shorter Rouse times can be found by adding stretching modes and including the uniaxial viscosity data for higher strain rates.

The Rouse time of the viscosity-averaged relaxation mode  $\tau_{R,\text{avg}}$  can be estimated with the expression proposed by Doi and Edwards [20], Equation (3.4) for monodisperse melts, which in the case of the average mode reads:

$$\tau_{R,\text{avg}} = \frac{\tau_{d,\text{avg}}}{3Z}, \quad (5.45)$$

in which  $Z$ , the number of entanglements per chain, can be calculated from the weight averaged molecular weight  $M_w$  and the averaged molar mass between entanglements  $\langle M_e \rangle$  with Equation (3.5). From [125] we took  $\langle M_e \rangle = 5.5 \text{ kg mol}^{-1}$  and find  $\tau_{R,\text{avg}} = 6.1 \cdot 10^{-2} \text{ s}$ .

As an initial condition for the MPR-flow computations, the melt is in an undeformed state:

$$\mathbf{B}_e = \mathbf{I} \quad \forall \mathbf{x} \in \Omega, t = 0. \quad (5.46)$$

For both capillary and MPR computations the following boundary condition is prescribed at the inlet  $\Gamma_e$ :

$$\mathbf{B}_e = \mathbf{I} \quad \forall \mathbf{x} \in \Gamma_e, t \geq 0. \quad (5.47)$$

To perform the numerical integration of the Rolie-Poly equation, Equation (3.3), we use a second order Adams-Bashford explicit scheme, see Section 3.3.3. For the first two time steps, the numerical integration follows a first order *forward Euler* method,

see Equations (3.11) and (3.12).

### Computational procedure: decoupled approach

In our computations we adopt a decoupled approach in which the flow kinematics are assumed to be dominated by viscous forces. Every time step the rate of deformation tensor,  $D$ , and the temperature field,  $T$ , are used to solve the viscoelastic Rolie-Poly equation, Equation (3.3), to compute the stretch of the high molecular weight chains in the melt  $\Lambda_{\text{HMW}}$  and the elastic Finger (conformation) tensor of the averaged relaxation times of the melt  $J_2(\mathbf{B}_{e,\text{avg}}^d)$ . The rate equations for crystallization are subsequently solved and the resulting degree of space filling used to update the viscosity via the hardening shift factor Equation (5.8). The decoupled procedure is illustrated in Figure 5.15 for the capillary-flow problem, which requires interface tracking between the polymer melt and air. For the multipass case the problem is simpler, since no interface has to be tracked.

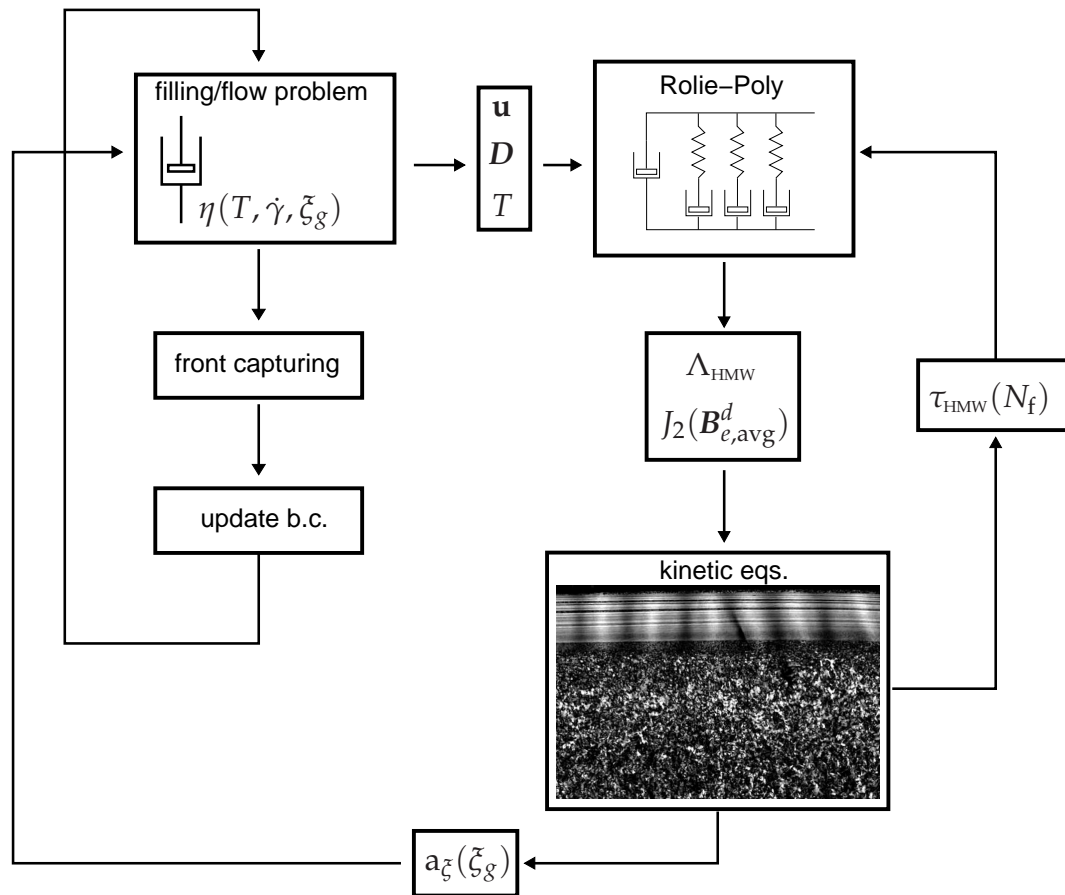


**Figure 5.15:** Decoupled computational procedure: the kinematics of a viscous flow problem are used to solve a coupled stress-crystallization problem. The computed degree of space filling is used to update the viscosity.

## 5.6 Modeling results & discussion

### 5.6.1 MPR

The micrographs of microtomed injection molding samples, as the ones shown in Figure 5.3 for the MPR experiments, denote in many cases sharp transitions between morphological layers, i.e. oriented layer, fine-grained layer, and spherulitical core. The transitions between these layers should most probably be related to critical values of the model parameters that drive flow-induced nucleation and growth,  $\Lambda_{\text{HMW}}$  and  $J_2(\mathbf{B}_{e,\text{avg}}^d)$ , respectively, and the morphological predicted parameters. Hence, we first look at the evolution of these parameters at the transition from the oriented shear layer to the fine-grained layer for flow conditions MPR1 and MPR2, whose optical micrographs clearly exhibit an oriented shear layer, see Figure 5.3. The time scale of the flow analysis is limited to the influence of flow on crystallization, which is determined by the relaxation of  $J_2(\mathbf{B}_{e,\text{avg}}^d)$ , since the flow-induced nucleation rate  $\dot{N}_f$ , given by Equation (5.29), becomes zero when the flow is stopped. After an elapsed time of  $t = 1.5$  s,  $J_2(\mathbf{B}_{e,\text{avg}}^d)$  becomes of  $\mathcal{O}(1)$  at the slit walls for conditions MPR1 and MPR2, thus the time scale of the flow analysis is limited to 1.5 s, after which the wall temperature is set to room temperature  $T = 23^\circ\text{C}$ . The crystallization kinetics are calculated until the degree of space filling  $\zeta_g$  is 1 everywhere. To better compare all the flow conditions, we list in Table 5.10 the Deborah numbers of each condition, based on the disengagement and Rouse times of the longest molecules, with  $De_{\text{d,R}} = \dot{\gamma}_{\text{wall}} \cdot \tau_{\text{d,R}}$ .

**Table 5.10:** Computed Deborah numbers based on disengagement  $De_{\text{d}}$  and Rouse  $De_{\text{R}}$  times, for the highest relaxation mode.

conditions	$De_{\text{d}}$ [-]	$De_{\text{R}}$ [-]
MPR1	$7.4 \cdot 10^4$	$4.4 \cdot 10^3$
MPR2	$6.7 \cdot 10^4$	$4.0 \cdot 10^3$
MPR3	$3.5 \cdot 10^4$	$2.1 \cdot 10^3$
MPR4	$0.8 \cdot 10^4$	$0.5 \cdot 10^3$

In Figure 5.16(a) we plot the time evolution of the molecular stretch ( $\Lambda_{\text{HMW}}$ ) at the positions of the transition between the oriented shear and the fine-grained layers. Once the critical stretch,  $\Lambda_{\text{crit}} = 40$ , is reached the transition from regime I to regime II, see Figure 5.13, takes place, and shish start to grow on a rate, according to Equation (5.33), that is dependent on  $J_2(\mathbf{B}_{e,\text{avg}}^d)$ , see Figure 5.16(c). The critical stretch is reached first for condition MPR1  $\sim t = 0.08\text{s}$ , which is expected based on the

**Table 5.11:** Model parameters at the transition between the oriented and the fine-grained layers.

conditions	$\Lambda_{\text{HMW}}$ [-]	$N_{\text{f,real}}$ [-]	$L_{\text{tot,real}}$ [ $\text{m}^{-2}$ ]
MPR1	90	$10^{12}$	$0.9 \cdot 10^9$
MPR2	70	$0.35^{12}$	$0.3 \cdot 10^9$

higher Deborah numbers  $De_{\text{d,R}}$  for this condition, see Table 5.10. The final values of the molecular stretch computed for both conditions are remarkably very close to each other (MPR1  $\sim 90$  and MPR2  $\sim 70$ ). The time evolution of the total number of real flow-induced nuclei  $N_{\text{f,real}}$  at the transition between the oriented shear layer and fine-grained layer, calculated from Equation (5.41), is shown in Figure 5.16(b).  $N_{\text{f,real}}$  is found to be very similar between both conditions, just slightly lower for condition MPR2. Figure 5.16(d) shows the time evolution of the total real shish length per unit volume  $L_{\text{tot,real}}$ , calculated from Equation (5.42).  $L_{\text{tot,real}}$  is found to be approximately three times higher for condition MPR1 than for flow condition MPR2, in agreement with the larger area underneath the plot in Figure 5.16(c). The values of  $\Lambda_{\text{HMW}}$ ,  $N_{\text{f,real}}$  and  $L_{\text{tot,real}}$  for flow conditions MPR1 and MPR2, at the transition between the oriented shear layer and the fine-grained layer are listed in Table 5.11. The values are of the same order of magnitude for the two flow conditions. Based on the crystalline morphology shown by the optical micrographs, see Figure 5.3, one can expect the transition from the spherulitical core to the fine-grained layer to be defined by a characteristic total number of flow-induced nuclei  $N_{\text{f,fg}}$ . Likewise, the transition from the fine-grained layer to the shear-oriented layer should be identified by the properties of the shish, either or by a critical average shish length  $\langle L \rangle_{\text{crit}}$ , or more likely a critical total shish length per unit volume  $L_{\text{tot,crit}}$ , upon which an oriented crystalline morphology becomes noticeable at a micro scale. Therefore, we postulate that within the fine-grained layer either the kinetics of flow-induced crystallization take place within regime I, see Figure 5.13, and, in that case, only an increase in number of spherulitical structures occurs, or the growth rate of shish is too slow or takes place within a too small period of time, so the shish stay relatively short. Regarding the shear oriented layer, we expect flow to induce only fibrillar nucleation (regime II).

We proceed comparing the model predictions in terms of  $L_{\text{tot,real}}$ ,  $N_{\text{f,real}}$  and  $\langle L \rangle$ , at the transition between the different morphological layers for all flow conditions after no further morphological changes, due to flow-induced crystallization kinetics, take place. The average length of shish-kebabs  $\langle L \rangle$  can be calculated dividing the total shish length by the total number of flow-induced nuclei per unit volume:

$$\langle L \rangle = \frac{L_{\text{tot,real}}}{N_{\text{f,real}}}. \quad (5.48)$$

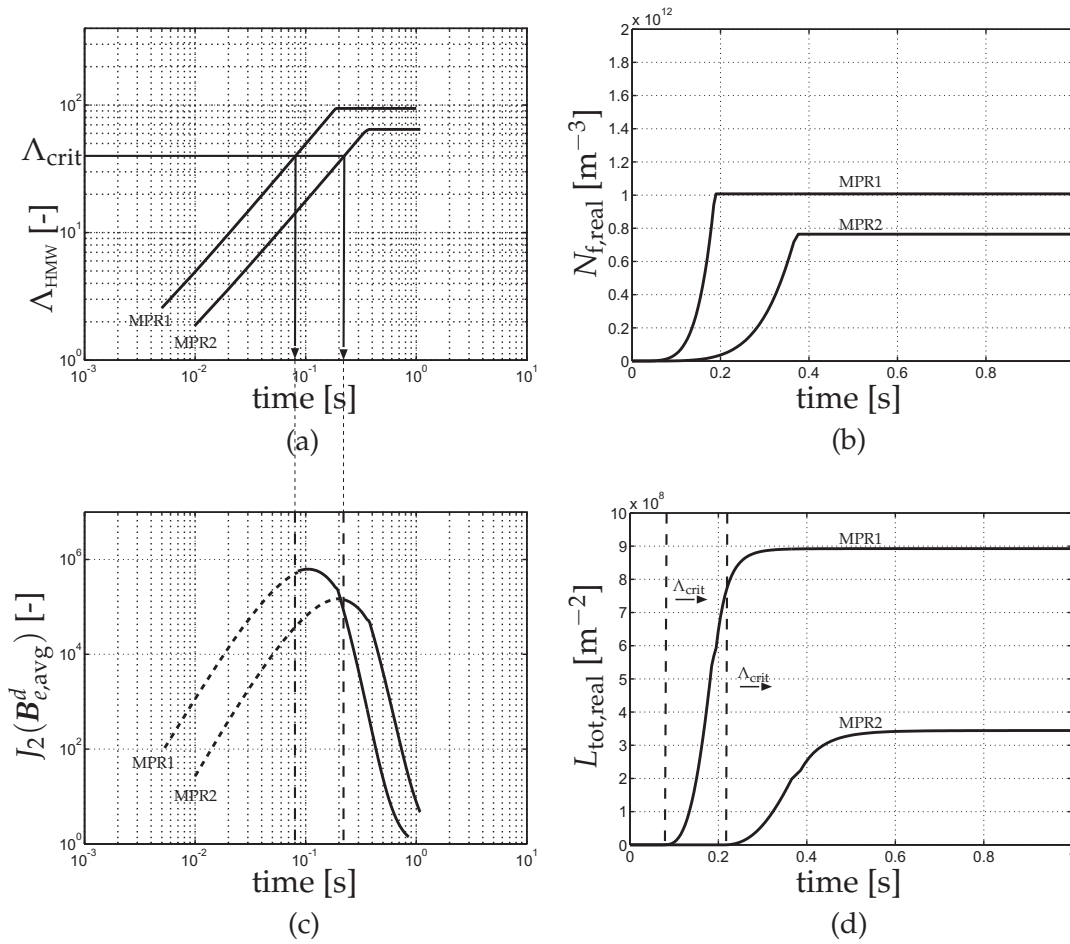


**Figure 5.16:** Model results for flow conditions MPR1 and MPR2, at the position of the transition from the oriented shear layer to the fine-grained layer obtained from the optical micrographs Figure 5.3: (a) molecular stretch  $\Delta_{\text{HMW}}$ ; (b) time evolution of the total number of flow-induced nuclei per unit volume; (c) evolution of the second invariant of the elastic Finger tensor of the averaged relaxation times  $J_2(\mathbf{B}_{e,\text{avg}}^d)$ ; (d) time evolution of the total shish length per unit volume  $L_{\text{tot,real}}$ .

In Figure 5.17 we plot  $L_{\text{tot,real}}$ ,  $\langle L \rangle$  and  $N_{f,\text{real}}$  over half of the normalized slit thickness, for flow conditions MPR1 and MPR2. The values predicted for condition MPR1 of  $L_{\text{tot,real}}$ ,  $N_{f,\text{real}}$  and  $\langle L \rangle$  at the transition of the shear oriented layer, are tested if they can be used as critical values that have to be surpassed for an oriented layer to become visible, see Figure 5.17.  $L_{\text{tot,crit}}$  denotes the critical value of  $L_{\text{tot,real}}$ ,  $\langle L \rangle_{\text{crit}}$  the critical average shish length,  $N_{f,\text{ori}}$  and  $N_{f,\text{fg}}$  the values of  $N_{f,\text{real}}$  found at the transition of the oriented shear layer and at the transition of the fine-grained layer to the spherulitic core, respectively. To assess the predictive capability of the model, the values  $L_{\text{tot,crit}}$ ,  $\langle L \rangle_{\text{crit}}$ ,  $N_{f,\text{ori}}$  and  $N_{f,\text{fg}}$ , taken from condition MPR1, are used as morphological criteria on the other flow conditions. The value predicted for a critical shish length  $\langle L \rangle_{\text{crit}}$  is around 1 mm, which obviously is too high, indicating that a further calibration for the values of the parameters is required. Typical shish lengths are

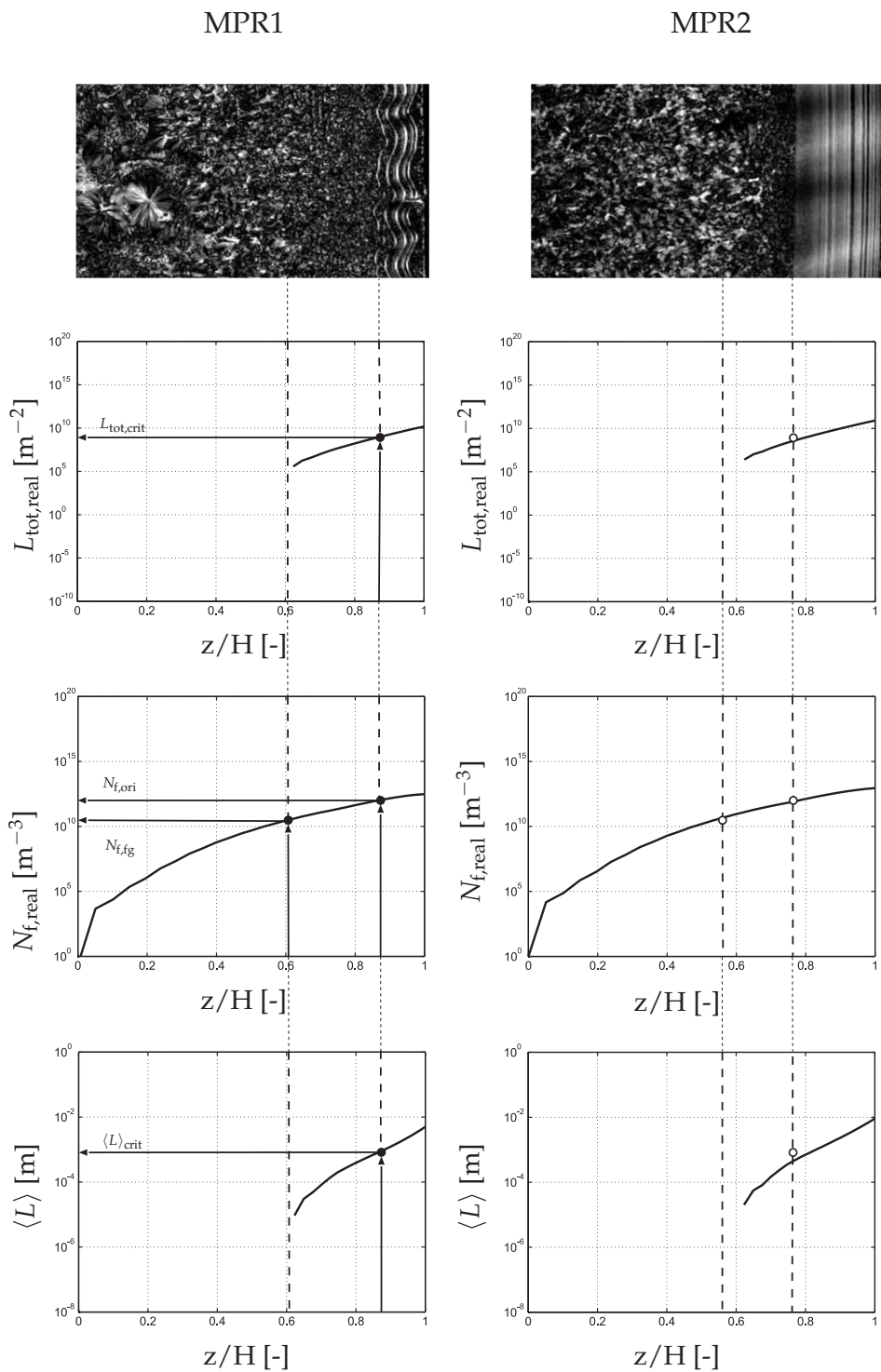


**Figure 5.17:** Distribution across half of the normalized slit thickness of the total shish length  $L_{\text{tot,real}}$ , the number of flow-induced nuclei per unit volume  $N_{f,\text{real}}$ , and the average shish length  $\langle L \rangle$ , after correcting for impingement, for flow conditions MPR1 and MPR2.

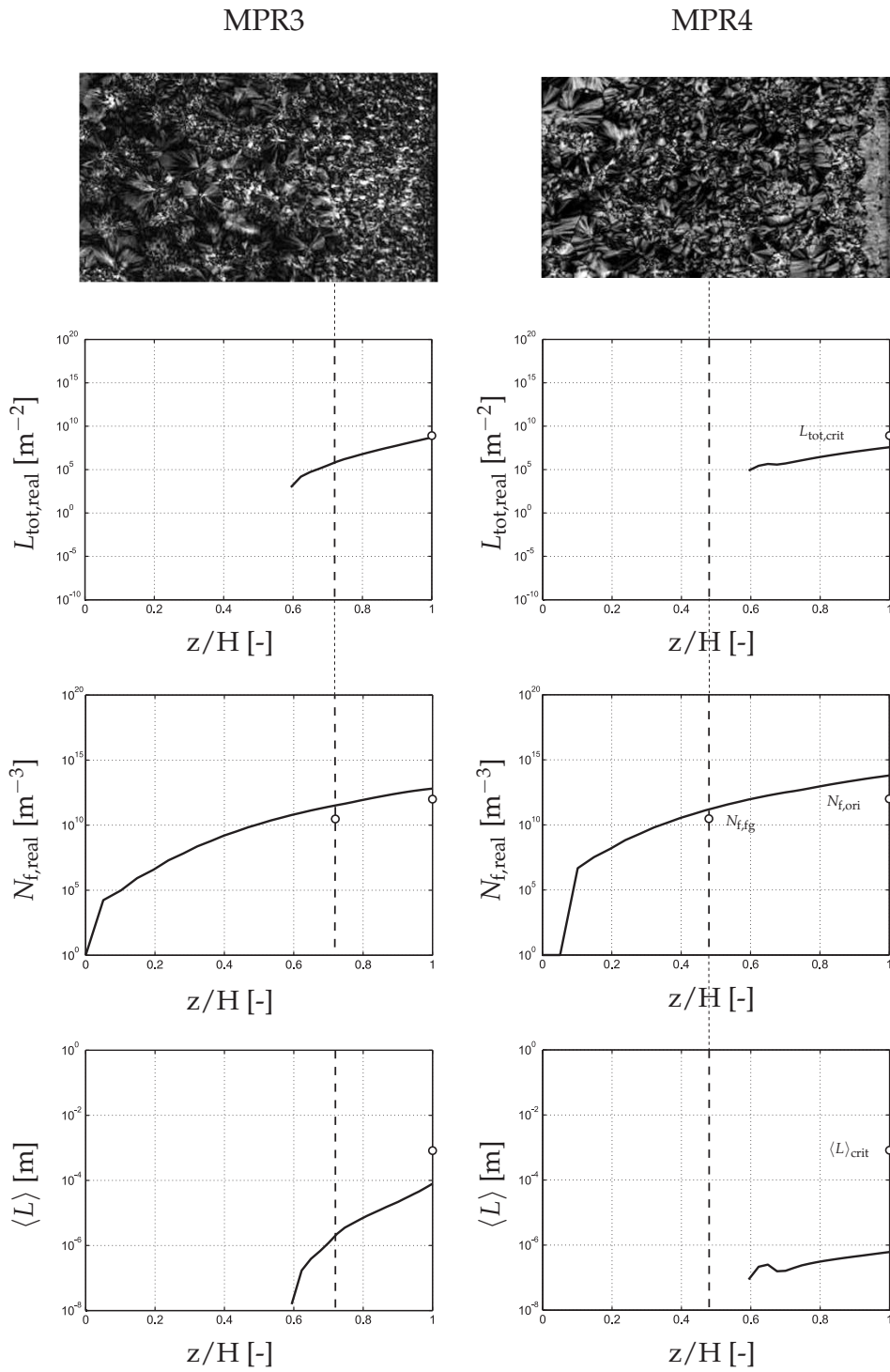


**Figure 5.18:** Distribution across half of the normalized slit thickness of the total shish length  $L_{\text{tot,real}}$ , the number of flow-induced nuclei per unit volume  $N_{f,\text{real}}$ , and the average shish length  $\langle L \rangle$ , after correcting for impingement, for flow conditions MPR3 and MPR4.



in the order of microns. The computed  $L_{\text{tot,real}}$  and  $\langle L \rangle$  for condition MPR1 lie within the flow-induced crystallization region (did not cross the fine-grained layer to the spherulitical core), implying that the critical stretch  $\Lambda_{\text{crit}}$  was reached only within this region. In the plots corresponding to condition MPR2 the open circles denote the critical values computed for condition MPR1. The circles fall almost on top of the curves, indicating that the different morphological criteria agree between these two conditions. However, the criterion based on total shish length  $L_{\text{tot,real}}$ , seems to be in better agreement between the conditions than the one based on the average shish length  $\langle L \rangle$ . The total number of flow-induced nuclei  $N_{\text{f,real}}$  at the transition between the different layers is also in good agreement between both conditions. Also for condition MPR2 the critical stretch, required for oriented crystals to grow (regime II), was reached only within the observed flow-induced crystallization region. Next, the flow conditions under which no oriented shear layer developed, namely MPR3 and MPR4, are considered. In Figure 5.18 we plot  $L_{\text{tot,real}}$ ,  $N_{\text{f,real}}$  and  $\langle L \rangle$  for conditions MPR3 and MPR4. The model-predicted number of flow-induced nuclei at the transition between the fine-grained layer and spherulitical core for conditions MPR3 and MPR4 is relatively higher than the one predicted for condition MPR1 (open circles). The value predicted at the transition of the oriented shear layer  $N_{\text{f,ori}}$  for condition MPR1 is also given as a reference at the wall, since there no oriented layer developed from conditions MPR3 and MPR4. The computed values for  $L_{\text{tot,real}}$  and  $\langle L \rangle$  are everywhere across the thickness smaller than  $L_{\text{tot,crit}}$  and  $\langle L \rangle_{\text{crit}}$ , respectively, with the exception of  $L_{\text{tot,real}}$  for condition MPR3 which equals  $L_{\text{tot,crit}}$  at the wall. Such results are obviously important, since they imply that a critical, total or average, shish length, required for an observable oriented shear layer, was not reached. However, the computed local shish length,  $L_{\text{tot,real}}$  and  $\langle L \rangle$  for condition MPR3, went beyond the flow-induced crystallization region, implying that the critical stretch  $\Lambda_{\text{crit}}$  was reached within the spherulitical core. This suggests that shish-kebabs might develop in the spherulitical region, however their size or volume fraction is too small.

Notice that these analysis, based on a coarse characterization done by means of optical light microscopy, can only be aimed at qualitatively agreements. The definition of a critical shish-length should therefore be based on more resolved analysis based on techniques that allow to assess more detailed morphological information, such as small angle X-ray scattering (SAXS).

### Oriented volume based criterion

As it was suggested in [136], the relative volume of oriented crystalline material, shish-kebabs volume over the total crystalline volume, could also be used as a criterion to define the transition between the oriented shear layer and the fine-grained layer. In Figures 5.19(a) to 5.19(d) we plot the relative undisturbed volume fraction of oriented crystals,  $V_{\text{ori}}$ , defined as  $\psi_0 / (\phi_0 + \psi_0)$ , after the completion of the crystallization process (after cooling to room temperature). The value of  $V_{\text{ori}}$  computed at the transition from the oriented shear layer to the fine-grained layer in conditions MPR1 and MPR2 is almost the same  $\sim 0.025$  [-]. For flow conditions MPR3 and MPR4

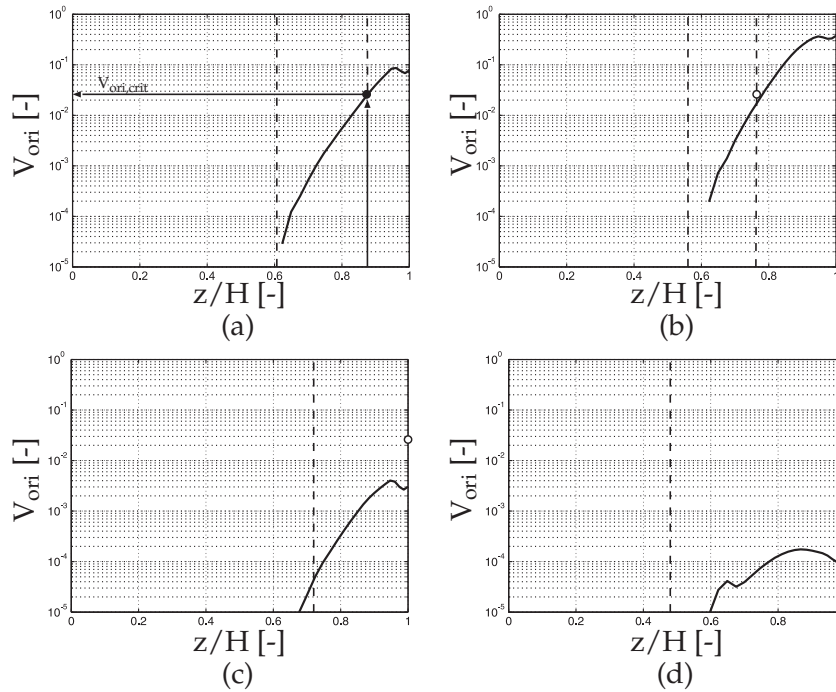


**Figure 5.19:** Distribution of the relative volume of oriented material,  $V_{\text{ori}} = \psi_0/(\phi_0 + \psi_0)$ , across half of the normalized slit thickness: (a) flow condition MPR1; (b) flow condition MPR2; (c) flow condition MPR3; (d) flow condition MPR4.

$V_{\text{ori}}$  is everywhere across the sample thickness smaller than the critical value  $V_{\text{ori,crit}}$  defined from flow condition MPR1, see Figure 5.19(a). This is in agreement with the experimental results that no visible oriented shear layer developed under flow conditions MPR3 and MPR4. Comparing conditions MPR1 and MPR2, the values of  $V_{\text{ori}}$  computed towards the slit wall for condition MPR2 are higher. To understand this we plot in Figures 5.20(a) and 5.20(b) the time evolution of the total shish-kebab and spherulitical volume close to the wall, where the highest volume fraction of oriented crystals is computed. As expected, the volume of shish-kebabs is higher for condition MPR2. Contributing to this, is the larger computed value for  $L_{\text{tot,real}}$ , see Figure 5.17, and the radial growth of kebabs. The predicted spherulitical volume for condition MPR2 is also found to be smaller than condition MPR1, further favoring a higher volume fraction of oriented crystals. The time evolution of the radial growth rate  $G(T, p)$ , given by Equation (5.21), at the same position close to the wall after wall quenching is shown in Figure 5.21(a) for conditions MPR1 and MPR2. One can clearly see that the radial growth for condition MPR1, due to differences in cooling history, see Figure 5.21(b), is higher, explaining the larger spherulitical volume predicted for this condition.

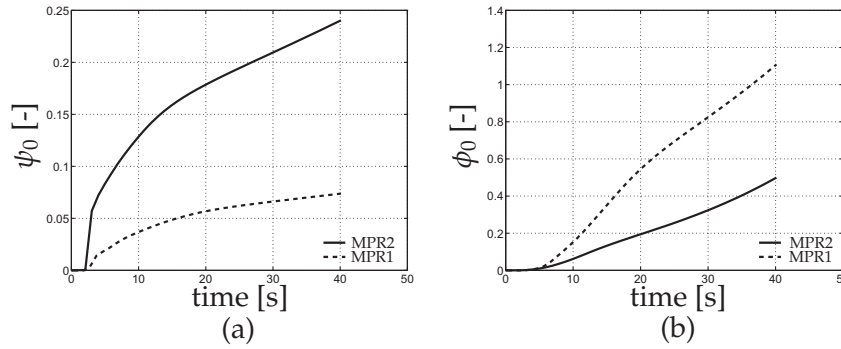


**Figure 5.20:** (a) Time evolution of the undisturbed shish volume  $\psi_0$ , close to the slit wall, for flow conditions MPR1 and MPR2; (b) time evolution of the undisturbed spherulitical volume  $\phi_0$ , close to the slit wall, for flow conditions MPR1 and MPR2.

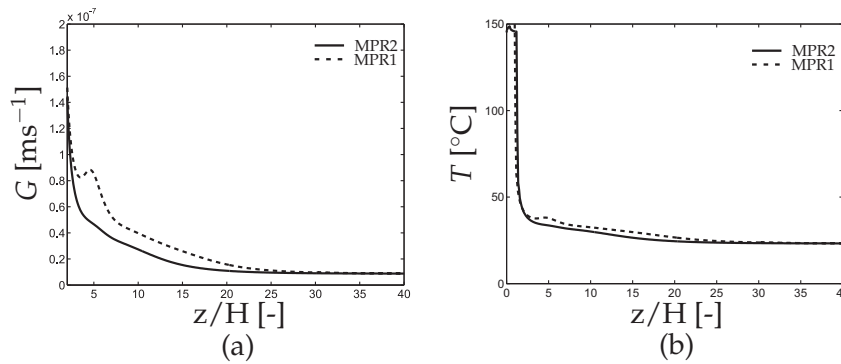


**Figure 5.21:** (a) Time evolution of the spherulitical growth rate  $G(T, p)$ , close to the slit wall, for flow conditions MPR1 and MPR2; (b) evolution in time of the temperature  $T$  after quench, for flow conditions MPR1 and MPR2.

## 5.6.2 Capillary rheometer

For the capillary rheometer the coupling of the viscosity with the degree of space filling gave rise to a non-smooth stress field. To circumvent this numerical problem, originated from a non-smooth viscosity distribution from the wall to the core, we did not couple the viscosity with the degree of space filling, Equation (5.7), with the consequence of reducing the effect of flow on crystallization. Figure 5.22 shows the computed total shish length per unit volume  $L_{\text{tot,real}}$ , the total number of flow induced nuclei  $N_{\text{f,real}}$  and the local average shish length  $\langle L \rangle$ , across the thickness of the slit at position 2, see Figure 5.2, for the capillary experimental flow conditions. The corresponding micrographs are given on top of the figure. The open circles denote the critical values for total shish length  $L_{\text{tot,crit}}$ , average shish length  $\langle L \rangle_{\text{crit}}$  and total number of flow-induced nuclei  $N_{\text{f,ori}}$  computed from condition MPR1. The values for  $L_{\text{tot,real}}$  computed at the transition of the oriented layer are close to  $L_{\text{tot,crit}}$  obtained from MPR1. However, the predicted values for  $\langle L \rangle$  for flow condition CA3 and CA1 is 3 orders of magnitude lower than the predicted value for the MPR exper-

iments, which is explained by the higher predicted critical number of flow-induced nuclei  $N_{f,ori} \sim 2$  orders higher. To verify the validity of morphological criteria based on shish length within the capillary experiments, the values of  $L_{tot,real}$  and  $\langle L \rangle$  computed from CA1 at the transition of the oriented shear layer to the spherulitical core are taken as critical criteria for condition CA3 (black dots). It can be seen that the dots fall on top of the curves, thus indicating that the model predicts at the transition of the oriented layer similar values for  $L_{tot,real}$  and  $\langle L \rangle$ , for completely different filling conditions. The criterion based on the total shish length per unit volume  $L_{tot,crit}$  is the one that gives the best agreement between the different experimental setups. It suggests that it is the total shish length per unit volume that determines the visibility of an oriented layer, and not the actual local shish length. The difference between  $\langle L \rangle_{crit}$  obtained from the MPR experiments and from the capillary experiments, can be explained on the basis of the different morphologies created by the experiments. In the MPR experiments, namely for flow conditions MPR1 and MPR2, three distinctive layers can be identified: an oriented shear layer, a fine grained layer and a spherulitical core. Instead, for the capillary rheometer experiments, the number and type of morphological layers differs. In this case, an oriented skin layer, a transition layer, an oriented shear layer and a spherulitical core, are identified. Thus, there is not a clear transition between the oriented shear layer and a fine-grained layer; therefore the comparison between the MPR results and the capillary results can be a bit misleading. The non-isothermal flow conditions under which the capillary experiments take place might explain the morphological differences. Nevertheless the model seems to give consistent results within each series of experiments, i.e., the average shish length criterion is valid within the MPR and the capillary rheometer experiments, and a reasonably good agreement in terms of  $L_{tot}$ . It is also interesting that the model captures the transition layer, between the skin and shear layers. For all the conditions, almost everywhere in this region the critical stretch of the high molecular weight  $\Lambda_{HMW}$ , which has to be surpassed for oriented crystals to grow (regime II), was not reached. It can be seen in Figure 5.22 that no shish-kebabs are predicted in that region by the model. This means that the coupling between the fast cooling close to the wall, and the transient viscoelastic behavior is captured quite well.

### Oriented volume based criterion

The computed volume fraction of oriented crystals at the transition to the oriented shear layer for the MPR experimental condition MPR1 ( $V_{ori} = 0.026 [-]$ ), was defined as a criterion  $V_{ori,crit}$  to identify the transition to the oriented shear layer. We now test the validity of this criterion in the capillary rheometer experimental results.

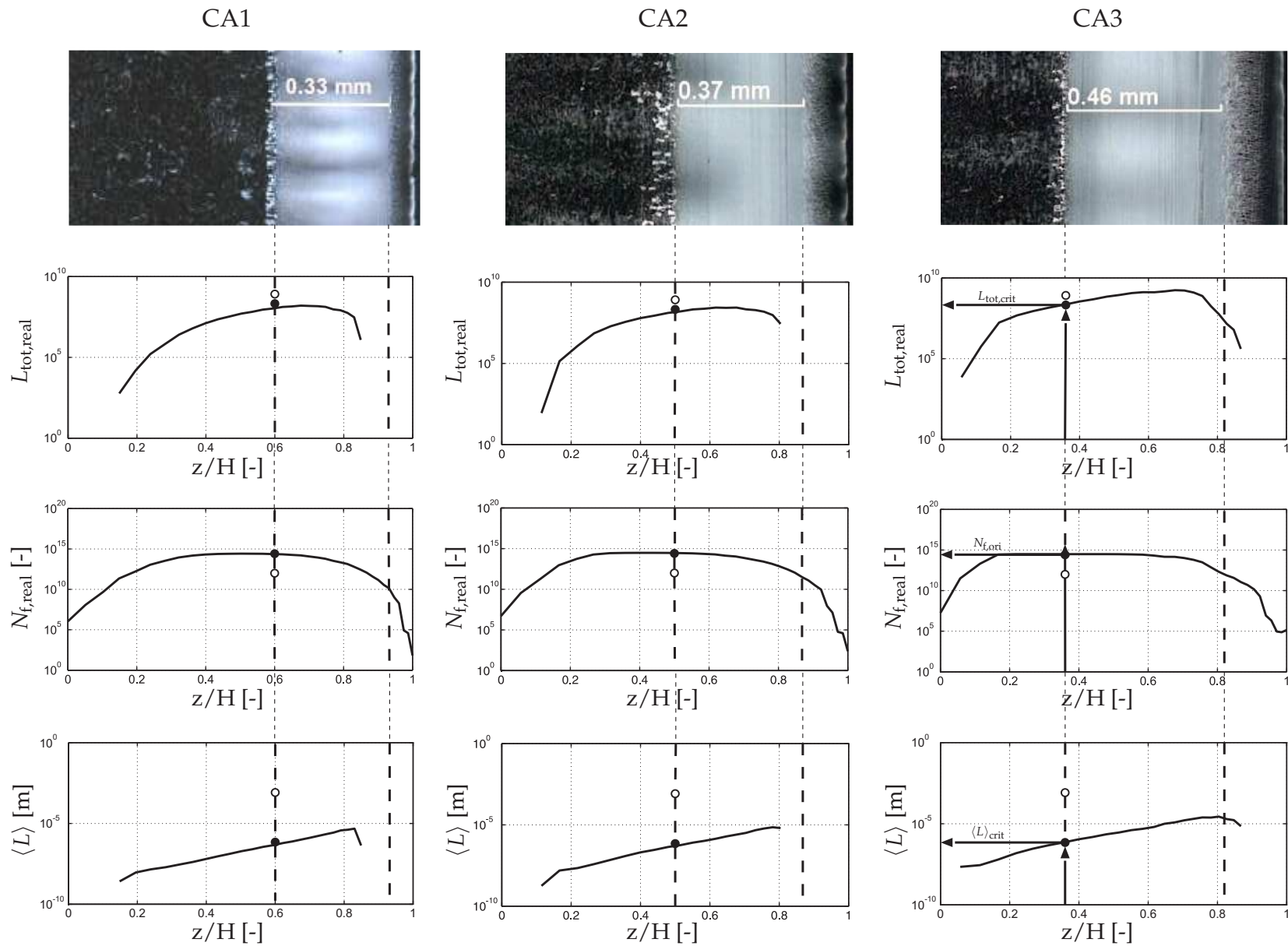


**Figure 5.22:** Distribution across half of the normalized slit thickness of the total shish length  $L_{tot,real}$ , the number of flow-induced nuclei per unit volume  $N_{f,real}$ , and the average shish length  $\langle L \rangle$ , after correcting for impingement, for flow conditions CA1, CA2 and CA3, at slit position 2.

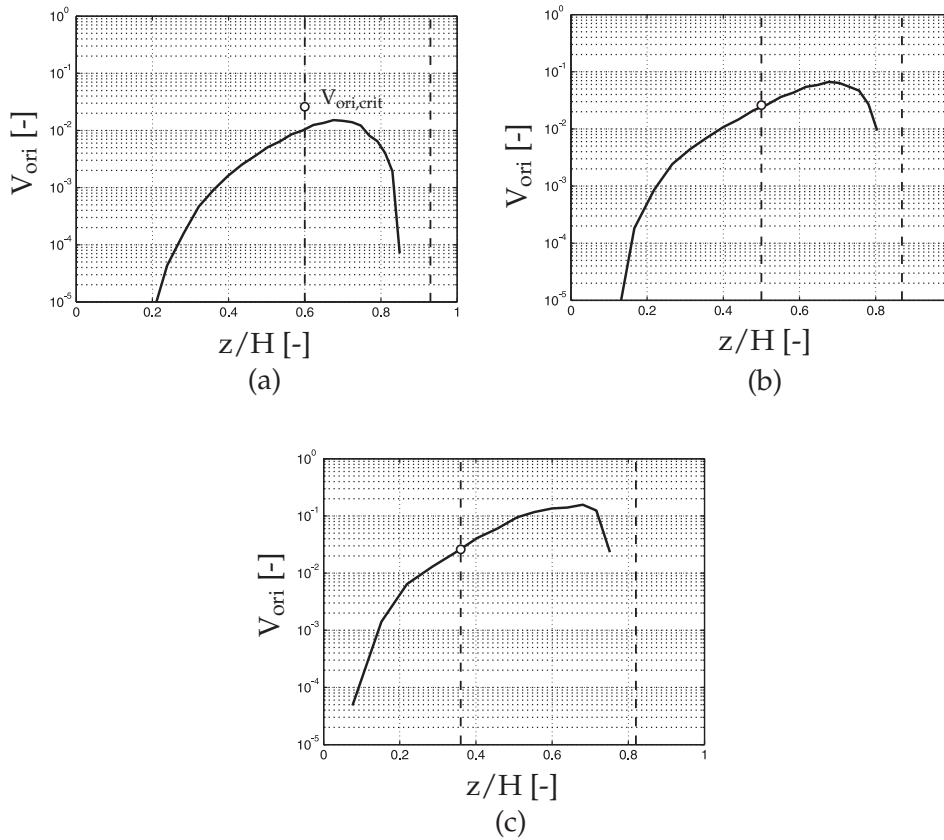


**Figure 5.23:** Distribution across half of the normalized slit thickness of the relative volume of oriented material,  $V_{ori} = \psi_0 / (\phi_0 + \psi_0)$ , across half of the normalized slit thickness at slit position 2: (a) flow condition CA1, (b) flow condition CA2, and (c) flow condition CA3.

In Figures 5.23(a), 5.23(b) and 5.23(c), we plot the volume fraction of oriented crystals for capillary conditions CA1, CA2 and CA3, respectively. The critical value  $V_{ori,crit}$ , taken from the MPR condition MPR1, is plotted as an open circle. For all flow conditions the predicted volume fraction of oriented crystals at the transition to the shear layer is remarkably similar, and the values are very close to the critical value  $V_{ori,crit}$ . For conditions CA2 and CA3 the agreement is excellent;  $V_{ori,crit}$  falls on top of the computed curves. This strongly indicates that the criterion based on  $V_{ori,crit}$  holds for experiments conducted under quasi-isothermal (MPR) and non-isothermal (capillary rheometer) conditions.

Due to start-up effects, which become more noticeable at high piston speeds (short flow times), the calculated average velocity in the slit for condition CA1, see Table 5.5, is over estimated. This could explain the lower predicted thickness of the shear oriented layer for this condition.

Based on the excellent agreement found for conditions CA2 and CA3, we plot for these conditions in Figures 5.24(a) and 5.24(b) the predicted and measured thickness

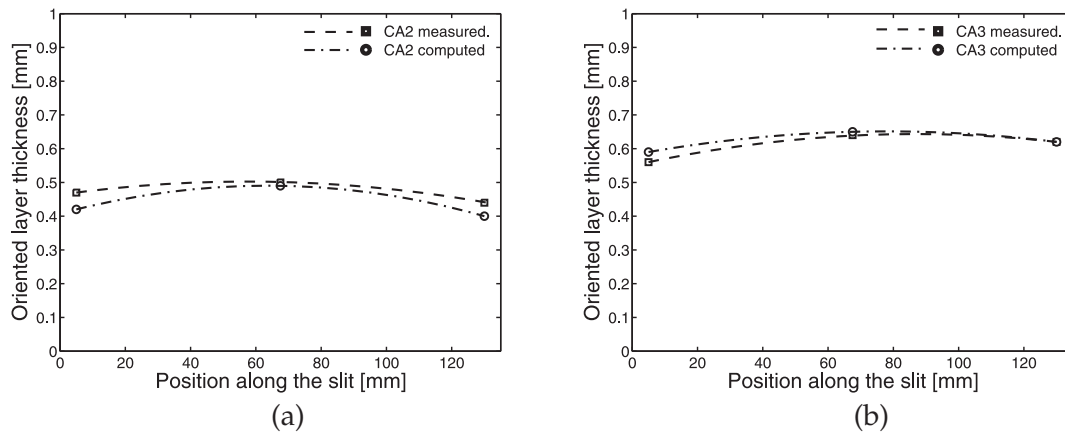


**Figure 5.24:** Symbols: measured and predicted oriented crystalline region thickness, based on the critical volume fraction of oriented crystals criterion  $V_{\text{ori,crit}}$ , for capillary flow condition (a) CA2 and (b) CA3. Lines are shown to guide the eye.

of the oriented region along the slit length at different positions along the slit. The predicted thickness of the oriented layer is close to the measured values and agrees well with the experimental trends: the thickness of the oriented crystalline region is higher at the center (position 2) of the slit.

## 5.7 Conclusions

In conclusion, we present in this study a model to predict the resulting morphology of semi-crystalline polymers when processed via injection molding related flows. A model within the framework of molecular-based rheological modeling is proposed, in which quiescent and flow-enhanced crystallization processes are coupled to the flow-history, and the deformation of long chains is assumed to drive flow-induced crystallization. The model is tested on a set of experimental results obtained using special experimental devices in which the processing history, i.e. deformation and thermal history, is accurately controlled. The approach adopted in this study aimed at, first of all, predicting flow-induced crystalline morphologies created under quasi-isothermal conditions (MPR) and then under non-isothermal conditions (capillary rheometer) that mimic injection molding conditions. The model predictions in terms of number, size and shape of crystalline structures for both non-oriented and oriented crystals, allows to establish criteria in terms of total shish length per unit volume  $L_{\text{tot,real}}$ , average shish length  $\langle L \rangle$  and volume fraction of oriented crystals  $V_{\text{ori}}$ , to identify the onset of an oriented shear layer. Such criteria are found to be in reasonably good agreement within the different experimental setups, between the tested flow conditions. Also, the predicted number of flow-induced nuclei at the transition of the morphological layers is found to be in agreement between all flow-conditions, within the MPR and capillary experiments. However, it is important to

stress, based on the model results, that criteria defined by  $\langle L \rangle_{\text{crit}}$  do not hold between isothermal and non-isothermal flow conditions. In contrast, criteria based on  $L_{\text{tot,real}}$  and  $V_{\text{ori}}$  seem to be in nearly quantitative good agreement with experimental results obtained under quasi-isothermal and non-isothermal flow conditions.

The morphological information predicted by the model is essential to construct the material microstructure, which could be embedded in a multi-scale modeling framework, as proposed in [122], to relate morphology to properties. Such approaches employ representative volume elements (RVE) of the microstructure to predict the material macroscopic mechanical response, thus using the microscale information to build an engineering scale material model.

Summarizing, we find the present results encouraging, in that a unified model for quiescent and flow-induced crystallization can be developed, sensitive to the molecular weight of the material, with few fitting parameters and generalized to other materials.

### Practical aspects of crystallization modeling

The application of elaborated models to predict the morphology of semi-crystalline materials, as the one presented in this study, in commercial software is still restricted by reasons of economical and practical nature. The main difficulty originates from the extensive material characterization required. A complete rheological characterization of the material is needed to determine the spectrum of relaxation times. Additionally, the characterization of quiescent crystallization kinetics has to be done in experiments in which spherulites are counted under an optical microscopy for different thermal and pressure histories. Furthermore, the approach suggested here to assess flow-induced crystallization kinetics combines the use of rheometry with numerical modeling, in which changes measured in the elastic modulus  $G'$  during crystallization, are predicted and used to fit the model parameters  $g_n$  and  $g_l$ . Last but not least, saturation studies also have to be done to determine the saturation level of flow-induced crystallization, which involve a shear flow device, e.g. Linkam shear cell, and optical microscopy. Hence, as the understanding of flow-enhanced crystallization phenomena improves, more material data are required to feed constitutive and kinetic models.

From a numerical point of view, the model presented here also poses some difficulties on current available software, as it requires two additional coupled problems to be solved: a two-mode viscoelastic stress problem, and a crystallization problem. The spatial discretization of the domain has to be sufficiently resolved to compute a smooth viscoelastic stress field and, consequently, the crystalline morphology. If using explicit-type of integration schemes to compute viscoelastic stresses, as the one proposed in Section 3.3.3, time steps become limited by the viscoelastic stress problem. Hence, computation times are significantly increased.





# 3-D Simulation of Injection molding: exploring the RCE mold

---

## Abstract

This chapter exploits the capabilities of the experimental molding tool developed by Silva et al. [102], the RCE (rotation, compression and expansion) mold, to induce and control different morphologies in injection molding discs applied to an isotactic polypropylene resin. This molding tool allows, by the mechanical action of one of its plates, to induce additional rotational, squeezing and expansion flows during mold filling. A combined experimental and numerical approach is followed in which we compute the thermal history and the flow kinematics, and relate it to the morphology developed under such complex thermal mechanical treatment. The microstructure of the injection molded discs is experimentally characterized by means of infrared spectroscopy and optical light microscopy. The distribution and morphology of the oriented crystalline layers is discussed based on the computed flow kinematics.

## 6.1 Introduction

The macroscopic properties of injection molded products are defined by the molecular structure of the polymer, the processing conditions applied, and part geometry chosen. Depending on the processing history, e.g. injection speed or cooling rates, different microstructures are induced, leading to different morphologies and, consequently, to different properties. In contrast to processes like fiber spinning, in which all material-fluid points experience the same processing history in axial direction, in injection molding the material microstructure develops locally according to the

in principle different thermal-mechanical history in each material-fluid point. This process-intrinsic characteristic has led to the development of non-conventional injection molding techniques which exploit the anisotropic nature of injection-molded parts as a basis for property improvement. Examples of such techniques are SCORIM (Shear Controlled Orientation in Injection Molding) [1] and Push-Pull [30].

Despite the development of numerical modeling tools for the injection molding process, little attention has been paid to the modeling of non-conventional injection molding techniques. In [102], a new injection molding tool - the RCE (Rotation, Compression and Expansion) mold - was used to manipulate the microstructure development during injection of a flat disk geometry. The possibility of generating and combining multiple flow types is the main novelty of this tool. More specifically, one of the cavity walls can rotate and move during the injection and holding stages, inducing an additional drag and squeeze flow to the radial filling flow. The authors have shown that the RCE molding tool is capable of generating different microstructures. In [103, 104], the RCE mold was used to manipulate the morphology of semi-crystalline polymers, and it was observed that upon increasing the rotation speed, the number of oriented layers increases. Furthermore, it was concluded that the complex velocity field resulting from an imposed mold-induced rotation-drag flow during radial mold filling is capable of generating novel morphologies. Recently the RCE mold was used to analyze the effect of rotation, compression (squeezing) and expansion on the orientation of fibers [130]. A combined experimental and numerical study was conducted in which a glass-fiber reinforced polypropylene was injection molded using the RCE mold. The Folgar-Tucker model [26] was implemented in an injection molding simulation code using a generalized Hele-Shaw formulation. The model predictions in terms of fiber orientation agreed with the experimental measurements. The authors concluded that the compression and expansion actions only had a small effect on the final orientation. However, the rotation imposed by the RCE mold decisively affected the final orientation, causing the fibers to align in the tangential direction across the entire thickness. It was asserted that the rotational drag flow overrules the effect of fountain-flow determining the fiber alignment across the entire cavity thickness.

Given the possibilities of this mold to manipulate the morphological development of polymers during injection molding, we conduct a combined experimental and numerical study to analyze its influence on the crystallization kinetics of an iPP resin. Injection molding experiments are preformed, in which we change the RCE mold rotational speed during filling, and characterize the morphology of the discs by means of optical light microscopy and infrared spectroscopy. Additionally, simulations are performed for similar conditions. Our main objective is to assess how rotation and squeezing affect the global kinematics and, from that, the effect of flow on the crystalline structure distribution. As a starting platform for our model we use the finite element-based injection molding code - VIp3D, as developed by Haagh [31]. Additional changes are introduced to take into account the special boundary conditions of the problem. The rotational or squeezing speed are changed in the simulations, and their effect on the global kinematics is analyzed. A benchmark numerical exper-

iment is defined to elucidate the resulting filling kinematics when adding rotation to a radial flow. The effects of computed kinematics on the observed morphologies is discussed.

## 6.2 Rotation compression expansion mold - RCE mold

The RCE mold was developed to improve and tailor the mechanical behavior of injection molding discs, via imposing controlled in-plane and through the thickness deformation fields during mold filling. Such deformation fields are the result of rotation or linear-displacement motions of one of the mold cavity surfaces. Schematic representations of the mold and of the possible mold moving actions are shown in Figure 6.1. The rotational and linear axial displacements can be controlled independently via two electric servomotors. These movements can be imposed in a steady fashion or in an oscillation mode, however in this study we only look at the influence of steady rotational and squeezing flows. For a more detailed description of the RCE mold the reader is referred to [102].

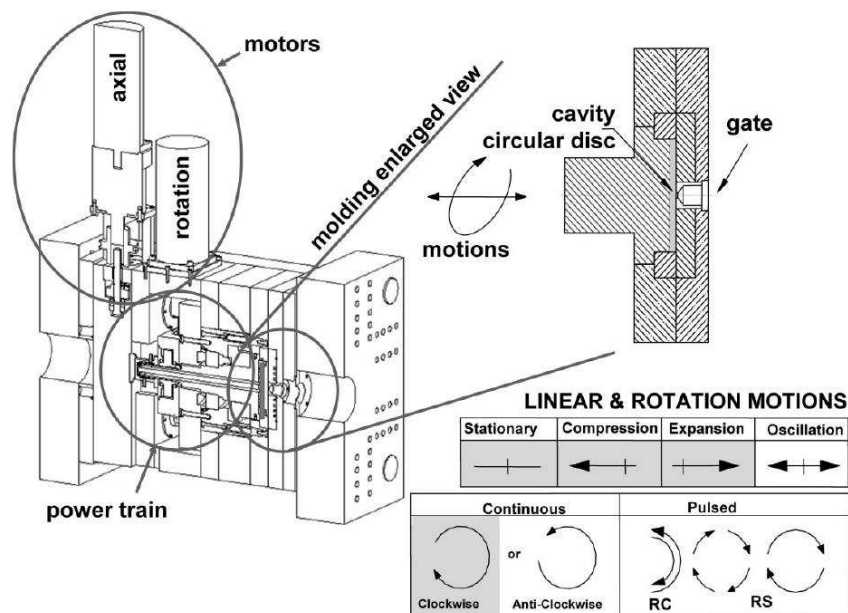


**Figure 6.1:** Schematic view of the RCE mold, detail of the mold cavity and operating modes, reproduced from [105].

**Table 6.1:** Injection molding conditions.

conditions	$T_{\text{flow}}$ [°C]	$\omega$ [rpm]
1	210	0
2	230	0
3	230	50
4	230	100
5	230	300

## 6.3 Experimental procedures

### 6.3.1 Material and processing conditions

An experimental study is performed with the RCE mold, in which the same isotactic polypropylene as presented in Chapter 5, iPP HD120MO, see Table 5.3, is used. Center-gated discs with a diameter of 150 mm and 4 mm thick are injection molded under different molding conditions: stationary conditions, i.e. no mold wall rotation, and non-conventional conditions in which the rotation speed of the plate is increased from 50 up to 300 rpm. The rotational flow induced by the RCE mold is imposed only during the filling stage. All the discs are produced using a Ferromatick Milacron K85 injection machine. The filling time is set to 5 s, the melt temperature to 230 °C and the mold temperature to 30 °C. At the end of filling a holding pressure of 10 MPa is imposed until the gate freezes off. The operative conditions of the RCE mold are summarized in Table 6.1.

### 6.3.2 Microstructure characterization

#### Polarized optical light microscopy

Cubes with an area of  $7 \times 7 \text{ mm}^2$  are cut from the discs at two different positions, P1 and P2, along the radius, see Figure 6.2. In order to assess the influence of the dominant flow, radial filling flow or rotational drag flow, on the microstructure developed, samples of  $15 \mu\text{m}$  are microtomed from two sides of the cubes. Figure 6.2 shows the layout used to cut out the cube-samples and indicates the different mode views to analyze the microstructure.

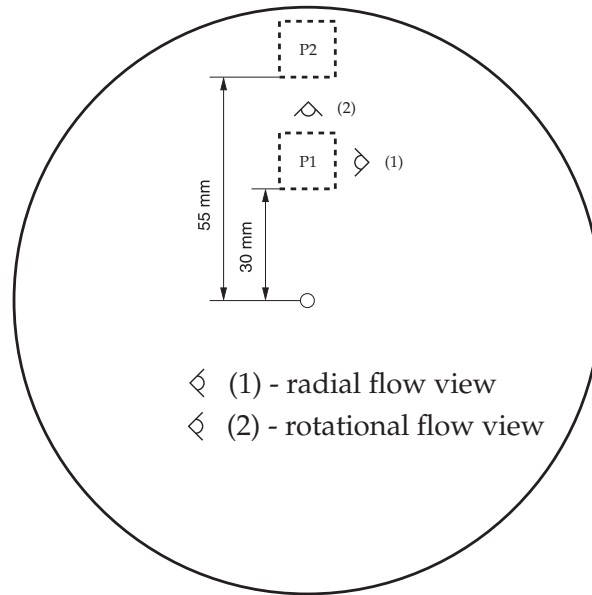


**Figure 6.2:** Cube-samples are cut from the injection molded discs at positions P1 and P2. From these cubes, samples are microtomed from two sides in order to visualize the microstructure developed in the vorticity and flow-direction planes.

### Fourier transform infrared (FTIR) spectroscopy

Infrared analysis are carried out to probe the crystallinity and molecular orientation distribution across the thickness of the samples. The degree of crystallinity,  $X_c$  is obtained from selected absorbed peaks that correspond to the crystalline phase, by applying Lambert and Beer's law [70]:

$$X_c = \frac{a_r A_{cr}}{a_{cr} A_r}, \quad (6.1)$$

in which  $a$  is defined as an absorption coefficient, and  $A$  as the absorbance. The indexes  $r$  and  $cr$  denote a reference and a crystalline peak, respectively. The ratio of absorption coefficients  $a_r/a_{cr}$  is set to 0.79, as suggested by [70]. The crystalline phase is here depicted by the peak at a wave length of  $841 \text{ cm}^{-1}$ .

The molecular orientation distribution is determined by infrared dichroism. The spectra are collected under cross polarizers and used to calculate the Herman's orientation function, which is given by:

$$f_p = \frac{3\langle \cos^2\theta_p \rangle - 1}{2} = \left( \frac{D_0 + 2}{D_0 - 1} \right) \left( \frac{D - 1}{D + 2} \right), \quad (6.2)$$

with  $D = \frac{A_{\parallel}}{A_{\perp}}$ , the dichroic ratio,  $A_{\parallel}$  and  $A_{\perp}$ , the absorbencies polarized along directions parallel and perpendicular to the flow direction, respectively. The Herman's

orientation function,  $f_p$  ( $p = c, av, am$ ) is a measure of the average angle,  $\theta_p$ , between the helix chain axis in a particular phase, crystalline (c), mixed (av) or amorphous (am) and the flow (stretch) direction. When  $f$  equals unity the helix chain axis is parallel to the stretch direction, zero when the system is randomly oriented and -0.5 when the helix axis is oriented perpendicular to the stretch direction.  $D_0$  is the dichroic ratio of an ideally oriented polymer, which is defined as  $D_0 = 2\cot^2\alpha_\nu$ , where  $\alpha_\nu$  is the transition moment angle at a specific wavelength,  $\nu$  [94]. To calculate the orientation of the crystalline phase,  $f_c$ , the transition moment angle is taken to be  $0^\circ$  [38].

## 6.4 Experimental results & discussion

The optical light micrographs exhibit, for all molding conditions, a morphology composed by a spherulitical core and a flow induced fine-grained region close to the mold walls, which consists of a dense fine-grained microstructure. According to the illustrated procedure Figure 6.2 used to microtome the samples, we present in Figure 6.3 optical light micrographs, for the molding conditions in which the rotation speed of the mold was changed, at the positions one and two along the radius.

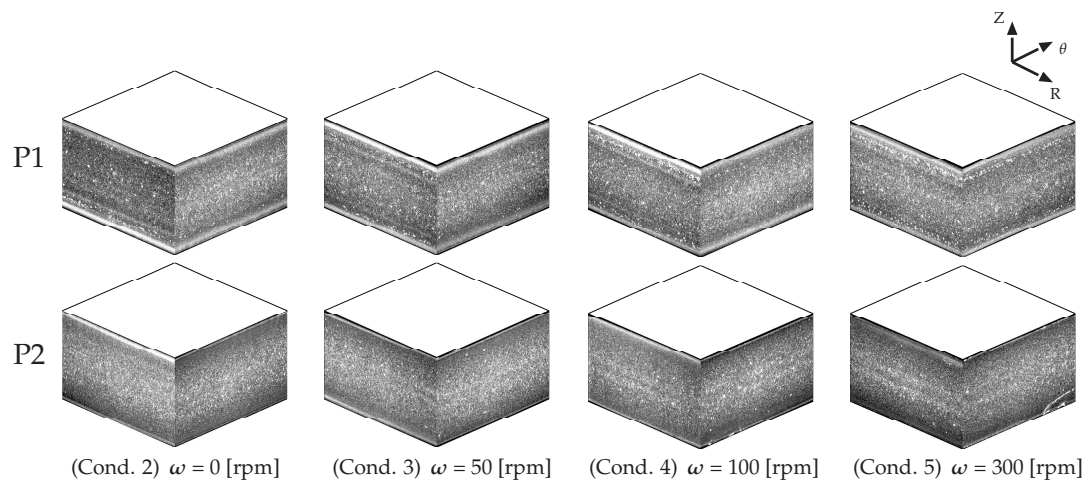


**Figure 6.3:** Micrographs obtained from polarized optical light microscopy.

The micrographs are assembled in cubes to show the morphology developed in the radial and rotational flow directions. It can be seen, that the thickness of the oriented crystalline region decreases along the radius, which is explained by the smaller shear and the shorter shear deformation history the material experiences further away from the gate. On the other hand, in the regions close to the gate, material solidifies under the effect of the shear deformation imposed by the filling flow due to longer cooling time. In Figures 6.4 and 6.5 we zoom in the micrographs taken in the radial and rotational view directions, for the conditions in which we vary the rota-

tional speed of the moving plate. For each molding condition we show the oriented region at radial positions one and two.

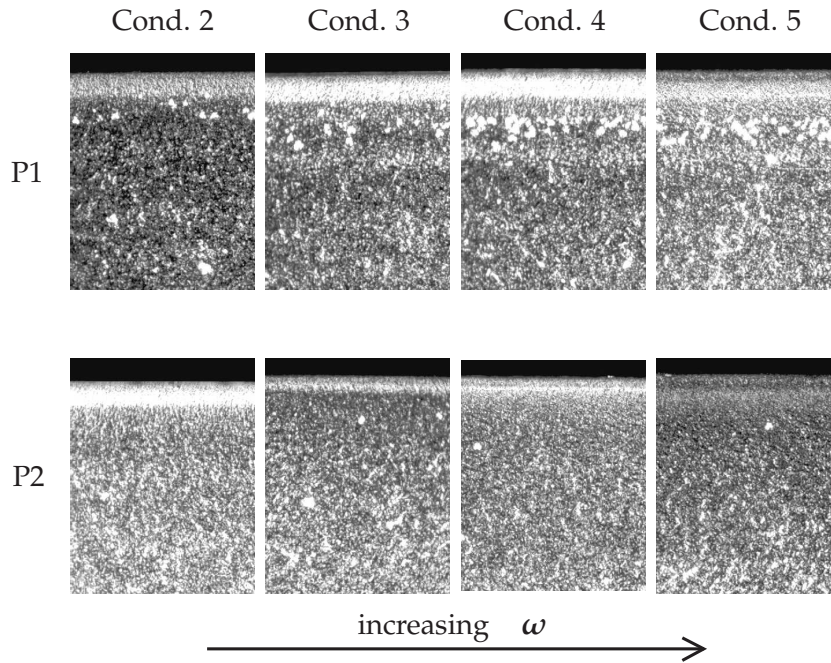


**Figure 6.4:** Fine-grained layer depicted from the radial flow view (see Figure 6.2).

Apart from the decreased thickness of the fine-grained region far from the gate for all the molding conditions, it can be seen that upon increasing the mold rotational speed the size distribution of crystals becomes more uniform but a different crystalline phase develops. Namely, bright spherulites appear in the vicinity of the fine-grained layer denoting the formation of  $\beta$ -phase crystals [100, 126]. The  $\beta$  modification of *i*-PP has a *frustrated* trigonal unit cell, instead of a monoclinic unit cell, typical of the  $\alpha$ -crystal phase. Upon heating,  $\beta$ -crystals re-crystallize into  $\alpha$ -phase crystals [55]. The  $\beta$ -modification typically develops in strongly deformed melts or in the presence of  $\beta$ -nucleating agents. Its formation is limited to a temperature window between 105 °C to 140 °C.  $\beta$ -crystals (spherulites or cylinders) are known to affect solid-state mechanical properties, namely they increase the material toughness [126]. However, given the narrow temperatures under which this crystal-phase develops, combined with its dependence on the deformations imposed by the flow-field, its formation and development is difficult to control in the complex thermal-mechanical environment of the injection molding process. Nevertheless, the stress-field induced by the rotation of the RCE mold seems to, remarkably, favor the formation of  $\beta$ -phase crystals. In Figures 6.6(a) and 6.6(b) we plot the thickness of the flow-induced fine-grained region for the molding conditions injected at  $T = 230$  °C to assess the influence of rotation speed. For all conditions an increase in rotation speed decreases the thickness of the oriented region. The effect of injection temperature is analyzed by comparing condi-



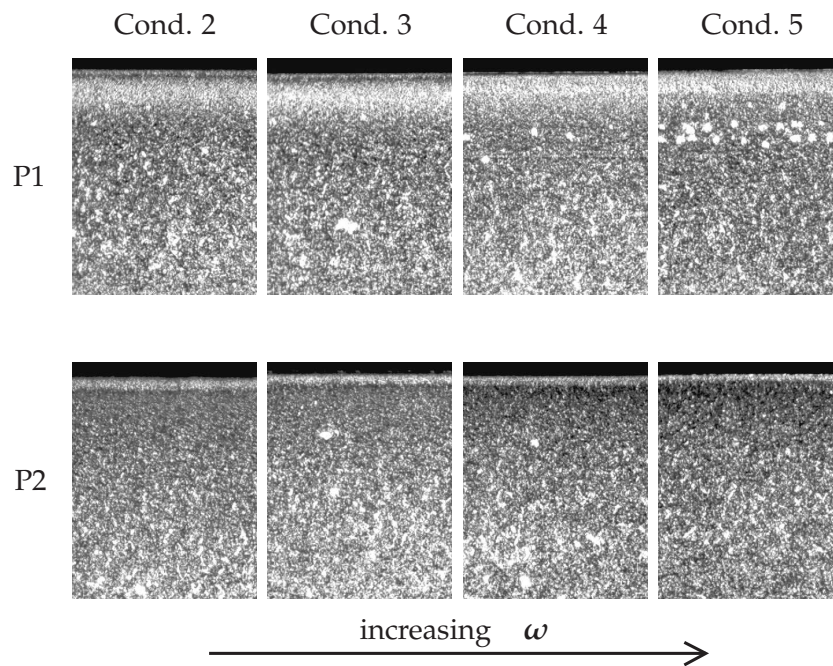


**Figure 6.5:** Fine-grained layer depicted from the rotational flow view (see Figure 6.2).

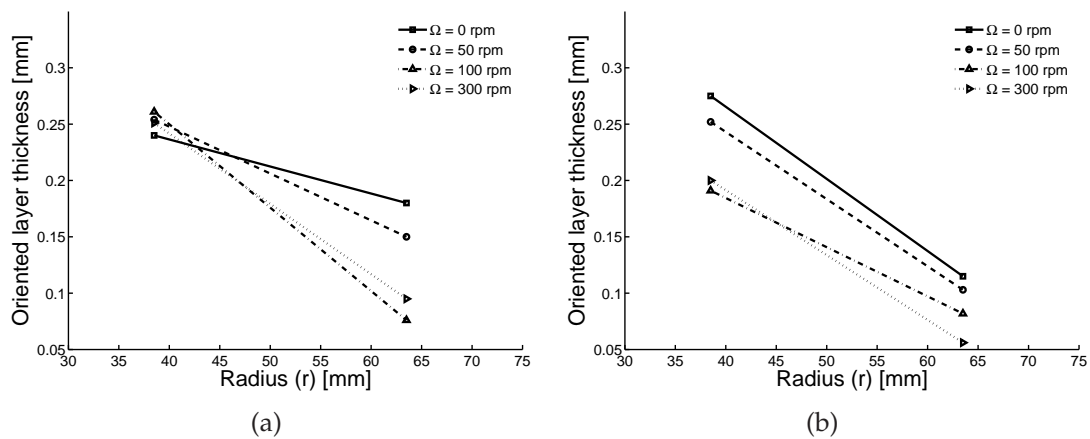


**Figure 6.6:** Thickness of the fine-grained layer in: (a) radial flow direction and (b) rotational flow direction.

tions 1 and 2, which is shown in Figure 6.7. As expected, the thickness of the oriented crystalline region increases with lowering the injection temperatures. Such a trend has been often reported and explained on the basis of higher molecular orientation as the result of the longer relaxation times of the molecules.

We proceed to analyze the FTIR results in terms of measured molecular orientation and crystallinity. In Figure 6.8(a) we plot for condition 3 the Hermans' orientation function  $f_c$  of the crystalline phase measured in the vorticity plane, across the disc

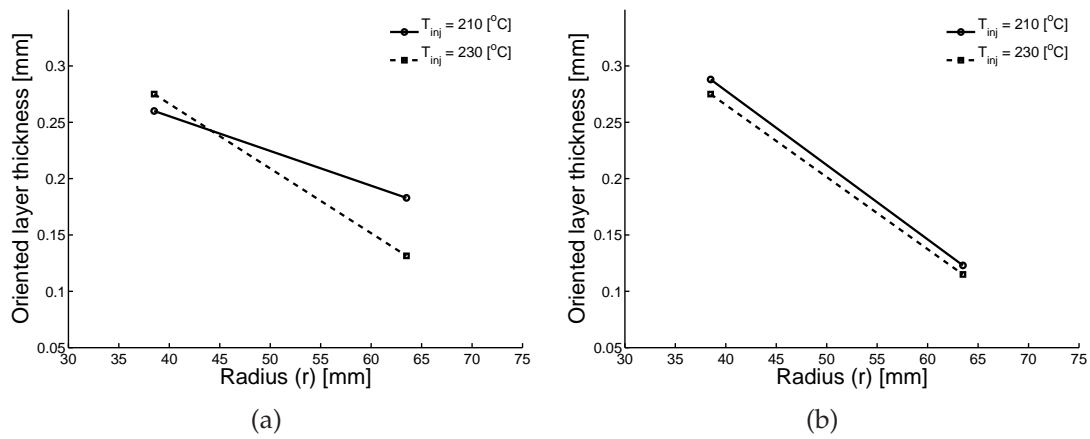


**Figure 6.7:** Thickness of the fine-grained layer in: (a) radial flow direction and (b) rotational flow direction.

thickness at positions 1. The measured orientation is zero. Identical results were found for all other molding conditions at all the measured positions, P1 and P2. Such result, obviously frustrates the analysis, but is clearly supported by the nonexistence of an oriented shear layer in the optical micrographs, see Figures 6.4 and 6.5. The cal-

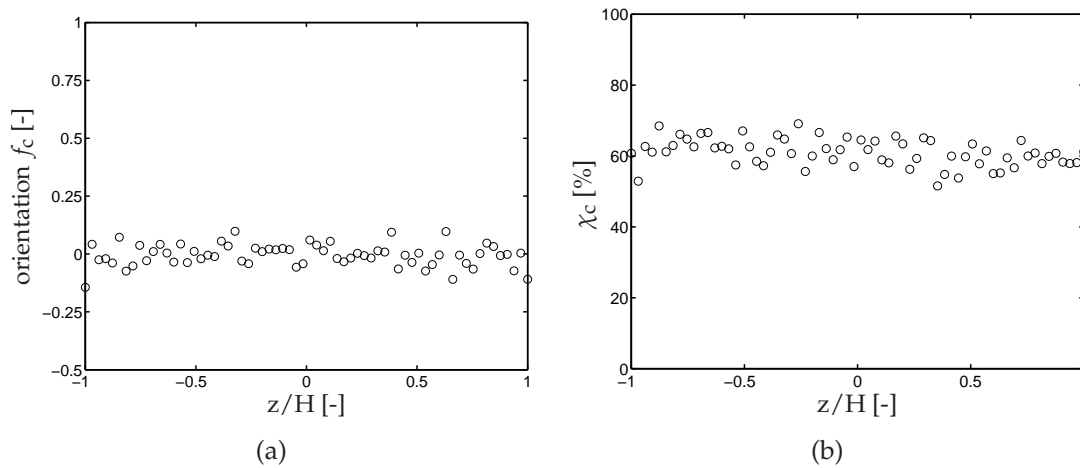


**Figure 6.8:** (a) Hermans' orientation function and (b) crystallinity  $\chi_c$ , measured in the vorticity plane over the thickness of the samples of condition 3 at radial-position 1 (see Figure 6.2).

culated crystallinity across the thickness from Equation (6.1), shown in Figure 6.8(b) for condition 3, is found equal to 60% for all conditions and measured disc locations. The same value was reported for iPP HD120MO in [40]. The large thickness of the discs and relatively high injection temperature favor together fast molecular relaxation. Therefore, the morphology developed does not contain an oriented crystalline morphology.

## 6.5 3-D computations of the RCE mold

To understand the complex thermal-mechanical fields induced by the RCE mold it is necessary to model the flow kinematics induced by the mold. Moreover, the prediction of the microstructure developed in the mold is of utmost importance. Given the rotation of one of the mold walls one cannot make use of the symmetry and solve the problem axi-symmetrically, hence fully 3-D computations are required to simulate the RCE mold experiments. We spatially discretized the computational domain with brick finite elements, with a discontinuous pressure of the type Crouzeix-Raviart -  $Q_2P_1^d$ , in which the velocity is approximated by a continuous piecewise polynomial of the second degree, and the pressure by a discontinuous complete piecewise polynomial of the first degree. The degrees of freedom at the nodal points correspond to the velocity components while at the central node the pressure and pressure gradients are computed. The integration on the element is performed using a 27-point Gauss rule. Figure 6.9 shows the computational domain, which is spatially resolved by a mesh with 17000 finite elements. The thickness of the disc is discretized with 10 elements. The gate is modeled as a cylinder of 2 mm diameter. The ratio between the gate diameter and the disc diameter is 75, which sets a large size ratio between the elements positioned nearby the disc edge and those close to the gate.

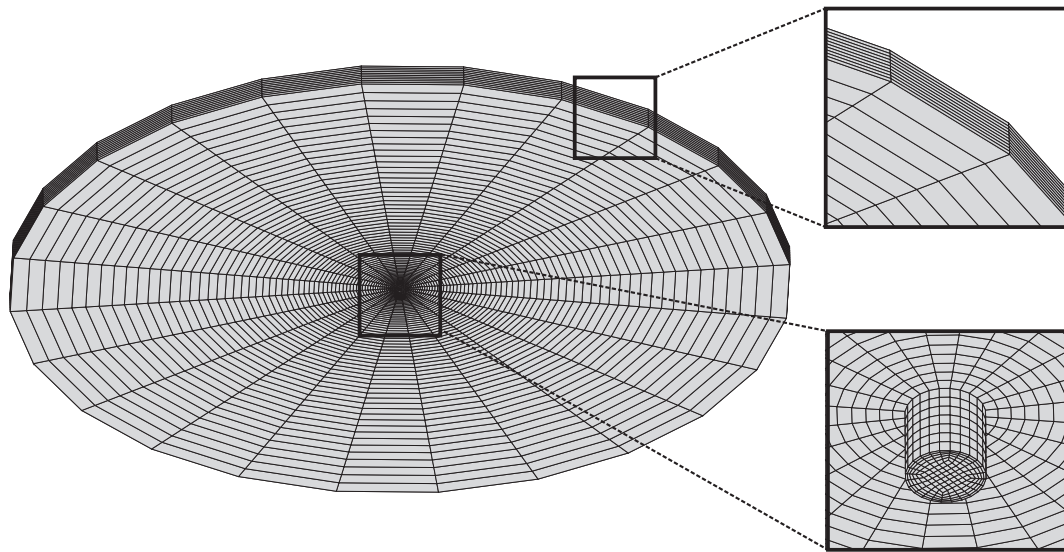


**Figure 6.9:** 3-D mesh for the computational domain, the enlargements show (bottom) the gate region and (top) the number of elements across the height.

The flow problem is governed by the equations presented in Chapter 2, Equations (2.21), (2.22) and (2.29), which are solved according to the numerical procedures presented in Section 2.2. The flow kinematics are assumed to be determined by the kinematic boundary conditions and a generalized Newtonian description is adopted

Equation (2.6). The viscosity dependence on shear rate and temperature is described by the Cross model, Equation (5.6). The model parameters used are listed in Table 5.2.

### 6.5.1 Boundary conditions

Special boundary conditions are required to induce the rotational and squeezing flows generated by the RCE mold. Boundary conditions are specified at  $\Gamma_e$ ,  $\Gamma_w$  and  $\Gamma_v$  designating the mold entrance, mold walls, and the air vents. The moving mold wall, which can rotate and translate with a linear displacement, is denoted as  $\Gamma_{mov}$ , because of the different boundary conditions to be assigned. At the mold entrance  $\Gamma_e$  a fully developed velocity profile is prescribed. As in the previous chapter, at the mold walls we change from slip to no-slip conditions through the use of dynamic Robin boundary conditions, see Section 2.1.4, which are a function of the type of the material label  $c$ . The wall temperature is set everywhere to  $60^\circ\text{C}$ .

#### Rotational-drag flow

The adjustable Robin boundary conditions are adapted to take into account the rotation and displacement of the RCE mold moving plate. Starting with standard injection molding conditions (stationary RCE mold conditions) the velocity and stress components  $\mathbf{u}_t$  and  $\mathbf{t}_t$  in tangential direction define a slip or non slip condition by setting a traction force at the wall. Accordingly, the boundary condition for the velocity and stress components  $\mathbf{u}_t$  and  $\mathbf{t}_t$  in tangential direction read:

$$a\mathbf{u}_t + \mathbf{t}_t = \mathbf{0} \quad \forall \mathbf{x} \in (\Gamma_w \cup \Gamma_v), \quad (6.3)$$

in which the dimensionless ‘Robin penalty parameter’  $a$  is defined as:

$$a = a(c) = \begin{cases} (\geq 10^6) & \text{if } c \geq 0.5: \text{ no slip or leakage} \\ 0 & \text{if } c < 0.5: \text{ slip or leakage} \end{cases}$$

To take into account the moving plate we adapt the above boundary condition to boundary condition to:

$$a\mathbf{u}_t + \mathbf{t}_t = \boldsymbol{\omega} \quad \forall \mathbf{x} \in (\Gamma_{mov} \cup \Gamma_v), \quad (6.4)$$

in which  $\boldsymbol{\omega}$  gives the rotation speed ( $\text{rad s}^{-1}$ ).

## Squeezing Problem, ALE Considerations

To take into account the RCE mold-induced squeezing flow, at the moving wall  $\Gamma_{\text{mov}}$  a squeezing velocity  $u_{\text{sq}}$  is prescribed:

$$\mathbf{n} \cdot \mathbf{u} = u_{\text{sq}} \quad \forall \mathbf{x} \in \Gamma_{\text{mov}}. \quad (6.5)$$

In addition, an algorithm to deform the grid-domain at each computational time step is introduced. The problem is no longer solved in a fixed grid (Eulerian description) but in an Arbitrary Lagrangian Eulerian (ALE) frame [21]. This implies that the mesh velocity  $\mathbf{u}_{\text{mesh}}$  has to be taken into account in all convective terms. We take the example of Equation (6.6), used to convect the material labels, that after the ALE correction reads:

$$\frac{\partial c}{\partial t} + (\mathbf{u} - \mathbf{u}_{\text{mesh}}) \cdot \nabla c = 0. \quad (6.6)$$

## 6.6 Computational results & discussion

### 6.6.1 Benchmark problem

To understand the effect of rotation during filling, we define a benchmark numerical problem in which we partially filled the mold cavity with a Newtonian fluid before injection. Making use of the pseudo concentration method we distribute over one of the halves of the initially filled polymer an additional concentration field, see Figure 6.10. We then resume the injection of the initial fluid at a constant flow rate, while at the same a rotational speed is prescribed at the top mold wall. The combined

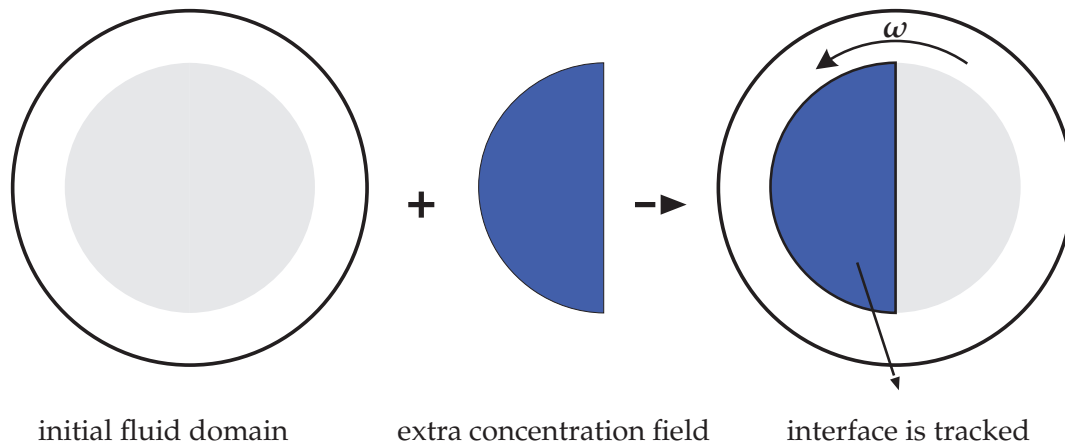


**Figure 6.10:** Addition of an extra material label field to a pre-filled disc molding cavity before injection.

influence of radial filling and rotation on the filling kinematics is depicted by the time evolution of the interface of the extra concentration field Figure 6.11.

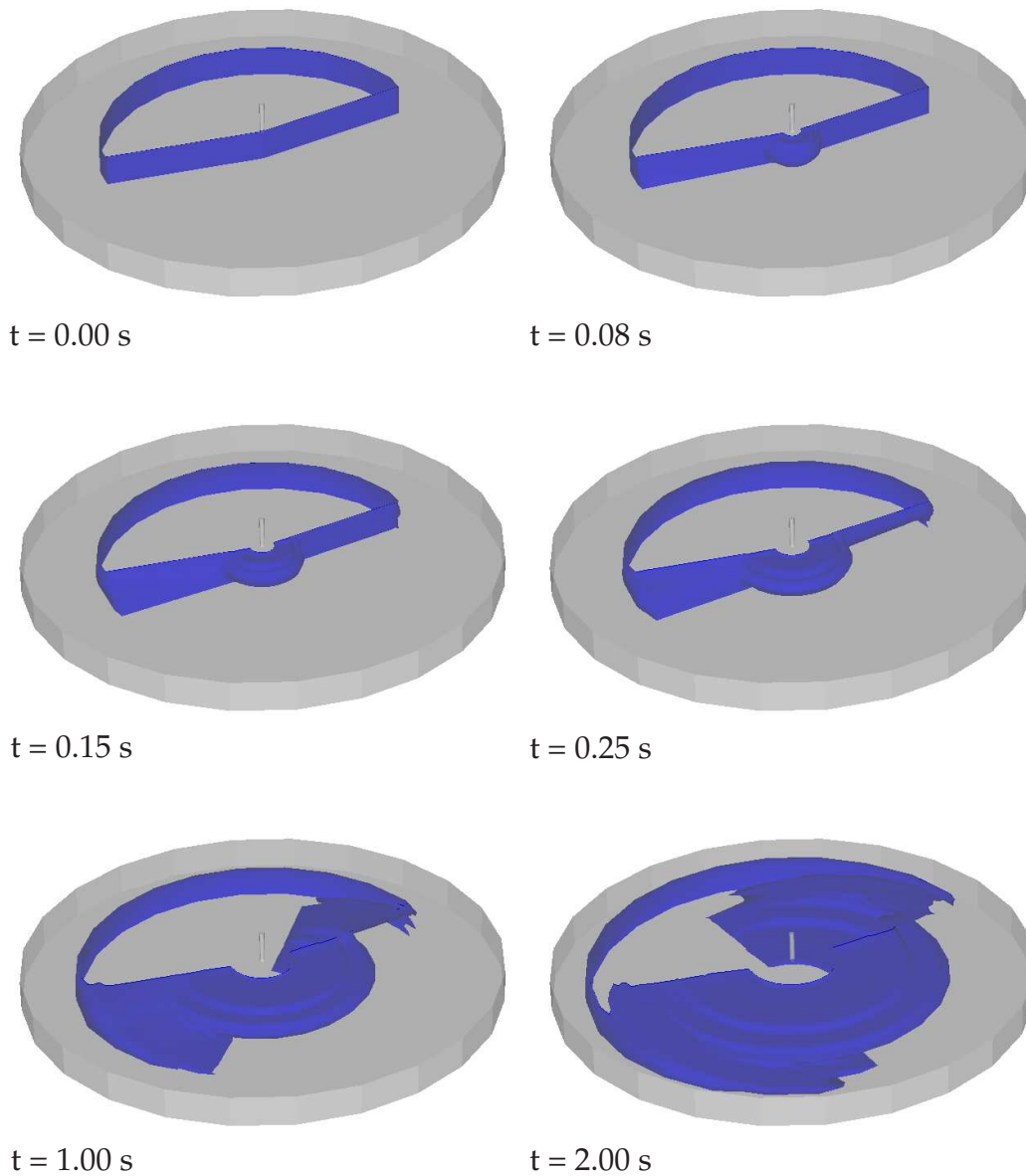


**Figure 6.11:** Time evolution of the interface of the extra concentration field.

### 6.6.2 RCE mold kinematics

Radial filling flow is a divergent flow. The increase of the flow-front area along the radius causes the radial filling speed to decrease, and, consequently, the magnitude of shear rates and the stretching at the flow front. Hence, the material deformation history significantly changes along the radius. Such change induces a high degree of anisotropy that often leads to warpage of the molded discs. The effect of adding a rotational-drag flow to the kinematics of radial flow is next analyzed. The simulations are limited to conditions 2, 3 and 4, see Table 6.1, since for the highest rotation speed ( $\omega = 300$  rpm) the problem became numerically unstable and convergence could not be found for the velocity problem. Figure 6.13 shows shear-rate profiles, with  $\dot{\gamma} = \sqrt{2\mathbf{D} : \mathbf{D}}$ , at various cross sections along the radius, see Figure 6.12, for molding conditions 2, 3 and 4.

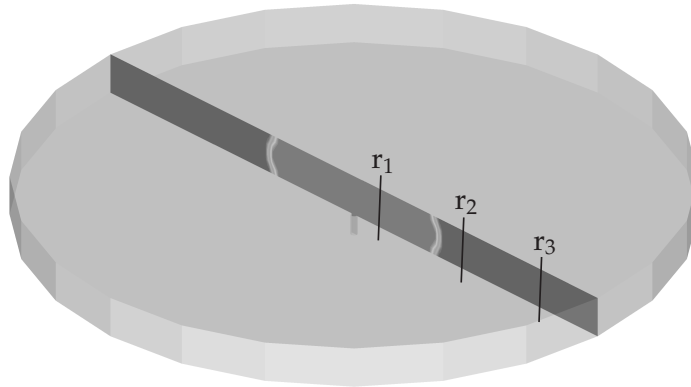


**Figure 6.12:** Plane depicting the material label field during mold filling. The lines denote the radial positions where results are analyzed:  $r_1 = 0.01$  m,  $r_2 = 0.03$  m and  $r_3 = 0.065$  m, respectively.

The effect of shear rate  $\dot{\gamma}$  by the increase in rotational speed along the radius counteracts the effect of radially decreasing filling speed. Thus, shear rates no longer decrease along the radius; i.e. the rotational flow induced by the RCE mold tends to radially balance (in an average sense) the shear rates. Furthermore, the shear rate profile changes upon rotation, instead of two peaks, typical from a non-isothermal filling flow, the profile becomes almost constant across the non-solidified part of the cavity's height, denoting the dominance of the rotational flow.

In Figure 6.14, we plot along the radius shear rates at the disc mid plane for conditions 2, 3 and 4, with a starting point offset a small distance from the center of the disc. The drastic effect of rotation on the flow kinematics can be seen, more noticeable for condition 4. Opposite to typical radial filling flow, the shear rate increases radially. Only in the vicinity of the gate region it decreases. Such dramatic change in

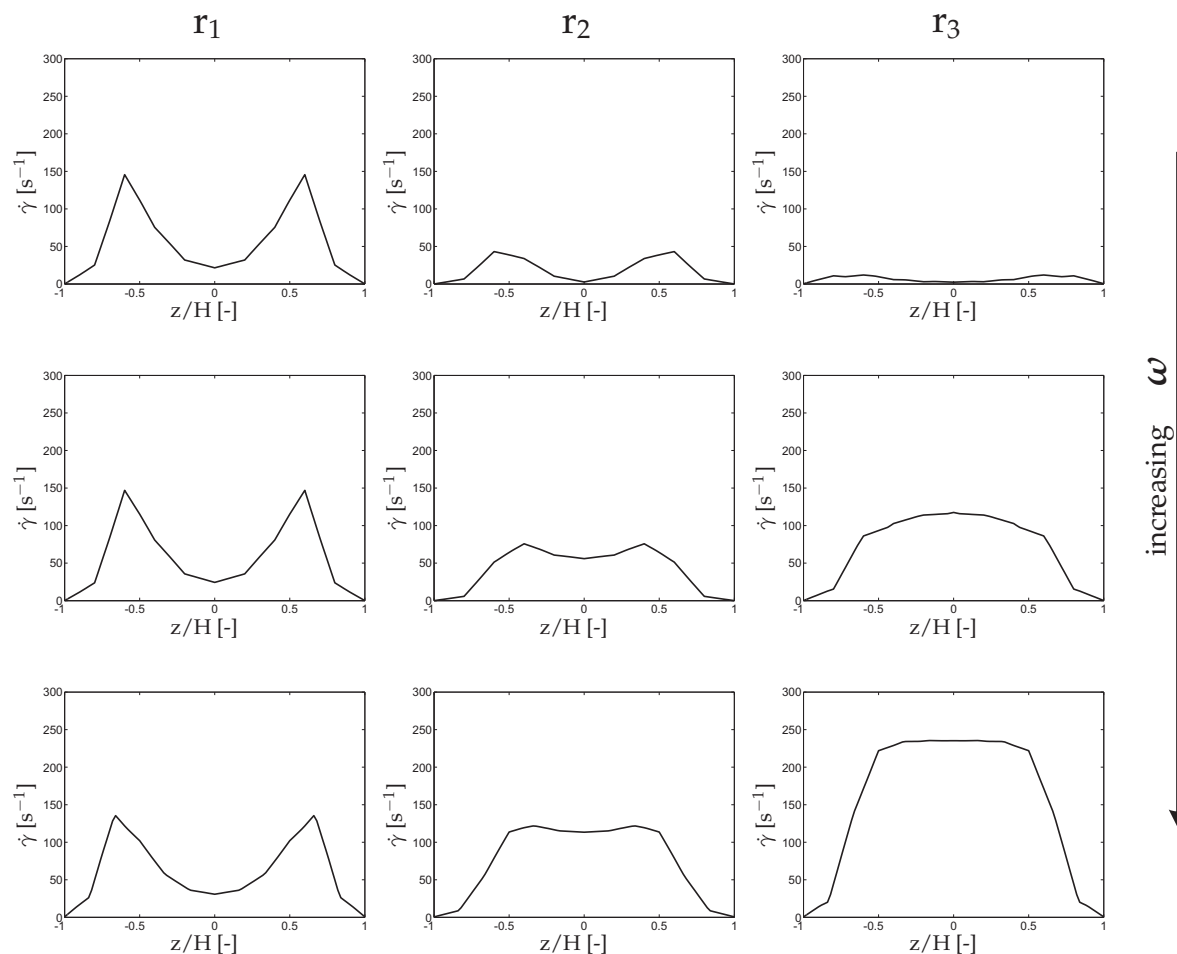


**Figure 6.13:** Shear rate profiles over the normalized disc thickness at radial positions  $r_1$ ,  $r_2$  and  $r_3$ , see Figure 6.12, with shear rate  $\dot{\gamma}$  defined as  $\dot{\gamma} = \sqrt{2\mathbf{D} : \mathbf{D}}$ .

flow kinematics, completely changes the deformation history of the material during filling. It is clear that the RCE mold can manipulate and change the development of the crystalline morphology of the molded discs. However, the effective deformation of molecules results from a coupled thermal-mechanical problem. In order to relate the predicted flow kinematics with the morphology observed by the optical micrographs, see Figures 6.6 and 6.7, we compute the Deborah numbers based on the Rouse time, defined as  $De_R = \dot{\gamma} \cdot \tau_R$ , for the longest chains. As described in Section 5.1, Van Meerveld et al. [125] classified different flow regimes depending on the Deborah number of the high end tail of the molecular weight distribution. The stretching of the high molecular weight chains, as extensively discussed in the previous chapter, drives flow induced crystallization, and, depending on the stretching Deborah number,  $De_R$ , oriented crystals may or may not develop. In Chapter 5, Deborah numbers for the different flow conditions of the MPR experiments, see Table 5.10, were computed close to the wall, using the rheological data listed in Table 5.2, and only when  $De_R > 4.0 \cdot 10^3$  an oriented layer developed. Since the same iPP



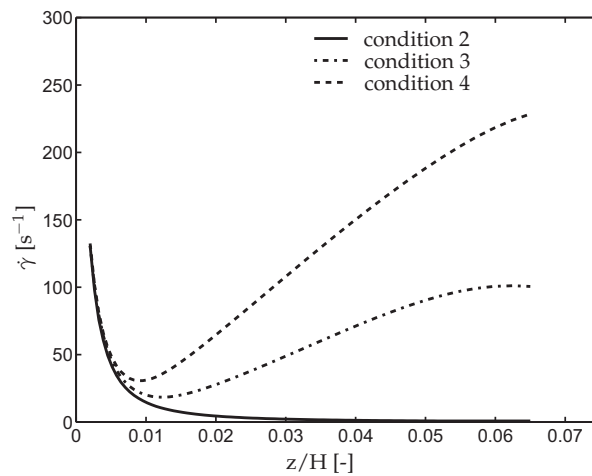


**Figure 6.14:** Shear rate evolution along the radius at the disc mid plane ( $z = 0$ ), with shear rate  $\dot{\gamma}$  defined as  $\dot{\gamma} = \sqrt{2\mathbf{D} : \mathbf{D}}$ , for molding conditions 2, 3 and 4.

resin is used in the injection molding experiments conducted with the RCE mold, we calculate  $De_R$  for the RCE molding conditions. We take condition 2 as an example, and plot in Figure 6.15  $De_R$  across the disc thickness at radial-position  $r_2$ . Only at the wall the computed  $De_R$  are of order  $10^3$ , but still  $< 4.0 \cdot 10^3$ , indicating that no shear oriented layer could have developed under the present flow conditions. For all other simulated conditions the computed Deborah numbers are  $< 4.0 \cdot 10^3$ . This is in agreement with the optical observations.

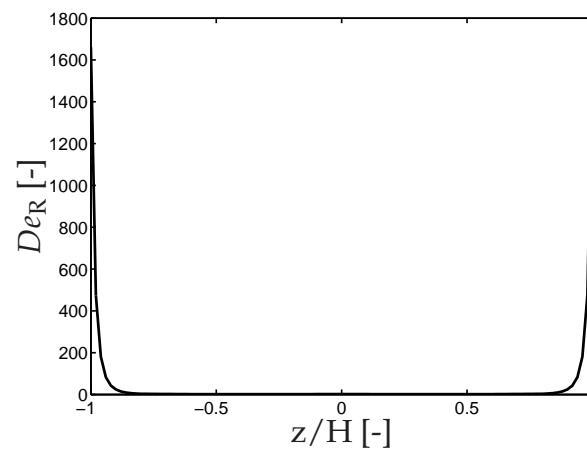


**Figure 6.15:** Deborah number based on the Rouse time of the longest chains, across the thickness of the disc for condition 2 and radial position  $r_2$ , see Figure 6.12.

## Squeezing effect

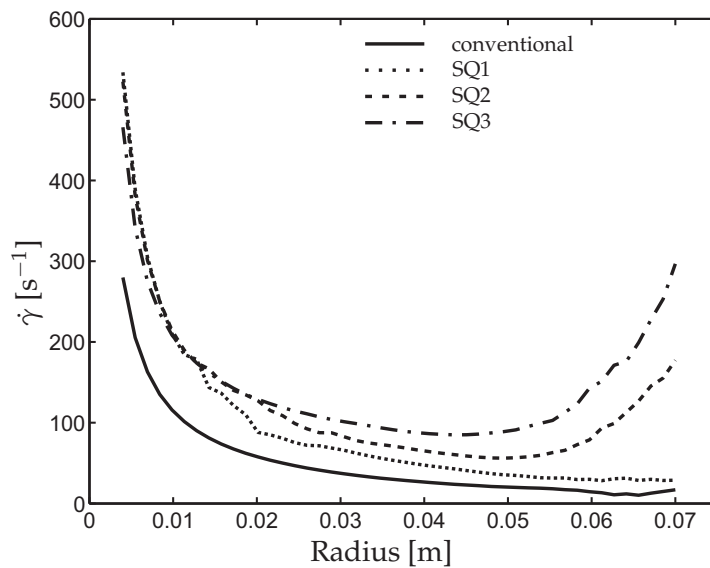
Even though the effect of squeezing flow on the morphology of the crystalline phase was not experimentally assessed in this study, we numerically analyze its effect on the kinematics combining RCE mold-induced rotational and squeezing flows. Three filling conditions are simulated, in which the rotational speed is changed, see Table 6.2, but the squeezing speed  $u_{sq} = -1.5 \cdot 10^{-4} \text{ m s}^{-1}$  prescribed at the walls, the volume flow rate  $\dot{Q} = 1.4 \cdot 10^{-5} \text{ m}^3 \text{ s}^{-1}$  and the injection temperature  $T_{inj} = 230 \text{ }^\circ\text{C}$  prescribed at the inlet, are kept constant.

**Table 6.2:** Rotational speeds used in the squeezing analysis.

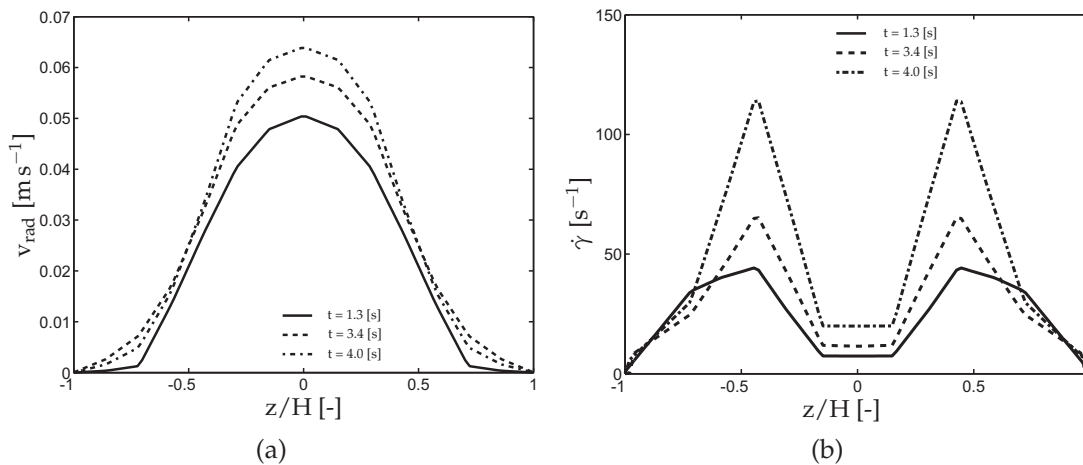
conditions	$\omega$ [rpm]
SQ1	0
SQ2	50
SQ3	100

Figure 6.16 shows the evolution of the shear rate along the radius when the cavity is almost filled, for the conventional case (condition 2, see Table 6.1), and for the squeezing conditions SQ1, SQ2 and SQ3. Shear rates are plotted at  $z = 0.8 \cdot 10^{-3} \text{ m}$ , where they are highest.

One can see that the decrease in the cavity height due to squeezing, as expected, increases the magnitude of the velocity gradients (shear rate), and that upon adding a rotational flow, the shear rate evolution along the radius attains a U shape profile. The effect of squeezing is also depicted in Figures 6.17(a) and 6.17(b), where the time evolution of the radial velocity profile and the shear rate profile for condition SQ1 (no rotation) is depicted at radial position  $r_2$ , see Figure 6.12. As the height of the mold cavity decreases, the radial velocity increases and thus the shear rates. Notice, that the profiles are plot over the normalized thickness. These results show that the squeezing flow imposed by the RCE mold can compensate for the radially decreasing filling velocity. Thus, the decrease in the cavity's height increases the velocity gradients, and minimizes, in an average sense, the drop in the shear rates along the radius. Furthermore, when combined with rotational flow, the squeezing flow further enhances the effect of the rotational flow.



**Figure 6.16:** Shear rate evolution along the radius at  $z = 0.8 \cdot 10^{-3}$  m for condition 2 (no rotation), and for squeezing conditions SQ1, SQ2 and SQ3.



**Figure 6.17:** Cross sections at radial position  $r_2$ , see Figure 6.12, for simulated condition SQ1 showing: (a) time evolution of the radial velocity and (b) corresponding shear rates.

## 6.7 Conclusions

The capability of the rotation, compression and expansion (RCE) mold to manipulate or control the morphological development of an iPP resin was assessed in this work. Optical micrographs from the disc samples, microtomed at several positions in the discs, show minor differences in terms of the developed morphology. Close to the walls a fine-grained crystalline layer is found, followed by a spherulitical core. No clear oriented layer is visible. The rotation exerted by the RCE mold during filling

had mild effects in developed morphology. It is observable that the increase of the rotational speed decreases the thickness of the fine-grained layer. Additionally, it favors the crystallization of  $\beta$ -phase crystals. From the FTIR analysis conducted, the Hermans' orientation function is found zero for all molding conditions over the thickness, agreeing with the morphology depicted by the optical light micrographs. The crystallinity is found to be constant for all conditions  $\chi_c = 60\%$ .

A numerical model to perform fully 3-D non-isothermal simulations of the injection molding experiments carried out with the RCE mold is proposed. The addition of the rotational flow to the radial-filling flow, is found, as expected, to counteract the decreasing radial-filling speed along the radius. Thus, the decreasing filling speed along the radius is compensated by the increase in rotational speed, balancing the shear rates along the radius. Such balancing is likely to affect the dimensional stability of the discs. From the computed kinematics Deborah numbers, based on the relaxation Rouse time of the longest molecules in the melt, were calculated to classify the flow conditions. In relation to the results obtained in Chapter 5 for the MPR experiments, the calculated Deborah numbers are found to be too low, further supporting the nonexistence of an oriented layer. Additionally, the effect of squeezing, and combined squeezing and rotation, on the kinematics was numerically investigated. The decrease in the cross sectional height of the mold cavity is found, as expected, to increase the radial velocity, and thus to affect the global kinematics.

In conclusion, the RCE mold, can in fact significantly change the filling kinematics of molded discs. The complex combination of flows requires a numerical tool to relate the experimentally observed morphologies and the flow conditions. Computational analysis are important to assess the thermal-mechanical deformation history of the melt. The calculated Deborah number based on the Rouse relaxation time of the longest chains in the melt, indicate that experiments should be done at different flow conditions for an oriented layer to develop. Furthermore, the high thickness of the discs (4 mm) favors fast relaxation of any induced orientation, therefor the thickness of the molded discs should be decreased.



# Conclusions and recommendations

---

## 7.1 Conclusions

### Residual stresses in GAIM

The use of gas-assisted injection molding, GAIM, in polymer processing has been motivated by the improved dimensional stability of molded parts. To understand why, we have numerically investigated the development of residual stresses in an injection molded rectangular cavity using polycarbonate, both via conventional and gas-assisted injection molding.

Firstly, the development of flow-induced stresses, originated by frozen-in orientation, was investigated. Computational results show a significant reduction in flow-induced stresses when using GAIM. Secondly, the development of thermally and pressure-induced stresses was assessed. The lower packing and holding pressures required during GAIM are found to be responsible for decreasing the development of these stresses. When compared with conventional injection molding, lower tensile stresses are found at the surface of the molded part.

Thus, the results presented strongly support the use of GAIM technology to produce molded parts with improved dimensional stability. The software package in which the modeling is implemented (VIp3D) is suited for analyzing more complex GAIM products. However, it was not the objective of this thesis to study such complex products but rather understanding how residual stresses develop in GAIM parts.

## Predicting the morphology of injection molded semi-crystalline materials

A model to predict the crystalline morphology of semi-crystalline polymers, in terms of number, shape and size of crystalline structures, developed within the framework of molecular-based rheological modeling, was derived. The molecular stretch of the longest chains in the melt,  $\Lambda_{\text{HMW}}$ , is assumed to drive flow-induced nucleation. A threshold in deformation is introduced via a critical molecular stretch,  $\Lambda_{\text{crit}}$ , which sets the transition from point-like to fibrillar nucleation. The growth of oriented crystals (shish) is assumed to be a non-selective process, in which all chains in the melt, regardless of their molecular weight, can participate. The average conformation of the chains, expressed by the second invariant of the deviatoric part of the elastic Finger tensor of the viscosity-averaged mode,  $J_2(\mathbf{B}_{e,\text{avg}}^d)$ , drives the shish length growth rate.

The model was tested using two sets of data obtained from two different experimental setups: a multipass rheometer under quasi-isothermal flow conditions, and a capillary rheometer under non-isothermal flow conditions. Based on the geometrical information of the predicted crystalline phase, different criteria were tested: the total shish length per unit volume,  $L_{\text{tot,real}}$ , the average shish length,  $\langle L \rangle$ , and volume fraction of oriented crystals,  $V_{\text{ori}}$ , found at the transitions from the shear oriented layer to a fine-grained layer, and from the fine-grained layer to a spherulitical core. The values predicted at these transitions are found to be in good agreement between the simulated flow conditions.

The predicted shish length per unit volume,  $L_{\text{tot,real}}$ , and relative volume of oriented material,  $V_{\text{ori}}$ , at the transition to the oriented shear layer, are found to be nearly in quantitative agreement, even between quasi-isothermal and non-isothermal flow conditions.

In conclusion, the crystallization model proposed addresses in a combined way quiescent and flow-induced crystallization, and couples the kinetics of flow-induced nucleation to viscoelastic phenomena. It requires only a few fitting parameters, and in the way it has been formulated can be generalized to other semi-crystalline materials.

The adopted strategy to predict the morphology development of semi-crystalline polymers in injection molding prototype flows proved to be successful. Crystallization kinetic models can only be validated when relating to experiments in which the thermal-mechanical deformation history of the material is accurately known.

## Manipulating the morphology of injection molded discs

The innovative rotation, compression and expansion, RCE, mold, developed to induce and manipulate the microstructure and properties of injection molded discs was modeled. Special boundary conditions were implemented in a 3-D injection molding code to incorporate the rotational and squeezing flows generated by the

RCE mold.

The experimental molding conditions chosen, failed to induce an oriented crystalline morphology. Nevertheless, computational results show that the rotation and compression operative modes can change dramatically the kinematics of the radial filling flow. Although the simulations conducted can help to understand the complex thermal-mechanical history experienced by the material, they still fall short of providing concise information of the underlying developed morphology. The use of the decoupled procedure and crystallization model proposed in Chapter 5 is hampered by the low mesh resolution used. To spatially resolve the transient development of viscoelastic stresses, and thereafter compute the flow-induced crystallization kinetics, would require a large number of finite elements that would yield a yet unfeasible computational time.

### **Main conclusions**

The deformation imposed on polymer melts, more specifically on the longest molecules, during injection molding determines the morphology the material microstructure acquires upon processing. Thus, in order to predict the material morphology, the computation of viscoelastic stresses is essential: they determine the state on which the material is vitrified, or how it crystallizes. In this work we have shown that by decoupling elastic effects from the flow kinematics, viscoelastic stresses can be easily computed, circumventing elastic instabilities that are numerically difficult to address. Different evolution models can then be added to predict the material morphological development based on the viscoelastic stress state. In the case of semi-crystalline materials, the problem is more complex, since the rheology is coupled to the developed crystalline phase. Having dealt with the processing of amorphous and semi-crystalline materials, within the mentioned decoupled approach, this work demonstrates the possibilities of this method, contributing new routes to predict the final properties of injection molded parts.

## **7.2 Recommendations**

The efficiency of the computation of the viscous flow problem could be improved using adaptive time stepping, based on the mesh resolution at the flow-front region. Thus, in the regions where the mesh is less resolved substantial computational time could be saved, complying at the same time the Courant criterion in those where the mesh is more refined. Additionally, the computation of viscoelastic stresses can also be made more stable and efficient using an implicit integration scheme.

The inclusion of a viscoelastic fluid model in the simulation of injection molding is a necessary step to predict elastic flow instabilities. In [44] a new method is proposed, in which a log-conformation representation is adopted to avoid numerical instabilities that arise at high Weissenberg numbers due to exponential growth of stresses.



The use of such a method is vital, since viscoelastic computations usually break down at Weissenberg numbers equal to one, which are far below those involved in the injection molding process.

The morphological information predicted by the crystallization model in Chapter 5 is essential to construct the material microstructure, which could be embedded in a multi-scale modeling framework, as proposed in [122], to relate morphology to properties. Such approaches employ representative volume elements (RVE) of the microstructure to predict the material macroscopic mechanical response, thus using the microscale information to build an engineering scale material model.

To improve the modeling of the capillary rheometer experiments one could adopt the fictitious domain method with distributed Lagrangian multipliers, see [28]. More specifically the method proposed by van Loon et al. [124], in which adaptive remeshing is not required. In this method, the fluid is described using a fixed mesh in an Eulerian frame while an updated Lagrangian formulation is used for the solid (the piston). To couple the fluid-solid responses Lagrange multipliers are defined along the fluid-solid interface, acting as a surface force exerted on the fluid by the solid. With this method the piston driven flow could be modeled without having to assume a fully developed Poiseuille flow at the slit inlet. Another possibility would be to employ the fictitious fluid method (variable viscosity), as used in [133], in which the piston (solid body) is replaced by a fluid whose viscosity is set to three or four orders of magnitude higher than that of the polymer melt. When compared to the fictitious domain method, this method has the advantage that no solid-fluid interaction needs to be considered.

The next step towards the prediction of the crystalline morphology in injection molded parts, would be to include changes in the specific volume due to crystallization. The new PVT apparatus developed in [121] allows the study of the combined effect of pressure, cooling rates and shear deformation on the specific volume of iPP at high pressures (up to 100 MPa) and cooling rates of  $100\text{ }^\circ\text{C s}^{-1}$ . Experimental PVT data obtained under semi-industrial conditions, is of utmost importance to derive an equation of state for semi-crystalline polymers. Only then can post-filling phases, i.e. packing and holding, be properly modeled, since to describe the correct pressure evolution inside the molding cavity, an understanding of crystallization kinetics under the combined effect of flow and pressure is required.

In order to exploit the capabilities of the RCE mold to induce oriented crystalline morphologies, the experiments conducted in Chapter 6 should be conducted with a lower wall thickness. The effect of decreasing the thickness of the discs in the cooling time is drastic, since cooling time  $t_c$  scales with the thickness of molded parts,  $h$ , according to:  $t_c \sim h^2$ . Thus, the decrease in thickness of the molded discs will significantly prevent the relaxation of flow-induced orientation.

Another strategy to study the crystalline morphological development using the RCE mold, is to add different concentrations of a small amount of high molecular weight material fractions, and study its catalyzing effect on the kinetics of flow-induced crystallization.

# Bibliography

---

- [1] P.S. Allan and M.J. Bevis. Scorim technology. *Plast. Rubb. Proc. Appl.*, 7:3, 1987.
- [2] P.R. Amestoy and I.S. Duff. Memory management issues in sparse multifrontal methods on multiprocessors. *Int. J. Supercomp. Appl.*, 7:64, 1989.
- [3] P.R. Amestoy and I.S. Duff. Vectorization of a multiprocessor multifrontal code. *Int. J. Supercomp. Appl.*, 3:41, 1989.
- [4] P.R. Amestoy and C. Puglisi. An unsymmetrical multifrontal lu factorization. *SIAM. J. Matrix Anal. Appl.*, 24:553, 2002.
- [5] M. Avrami. Kinetics of phase change 1. general theory. *J. Chem. Phys.*, 7:1103–1112, 1939.
- [6] M. Avrami. Kinetics of phase change 2. transformation-time relations for random distribution of nuclei. *J. Chem. Phys.*, 8:212–224, 1940.
- [7] F. Azzurri and G.C. Alfonso. Lifetime of shear-induced crystal nucleation precursors. *Macromolecules*, 38:1723–1728, 2005.
- [8] F.P.T. Baaijens. Calculation of residual stresses in injection molded products. *Rheol. Acta*, 30:284–299, 1991.
- [9] G.K. Batchelor. *An introduction to fluid mechanics*. Cambridge University Press, Cambridge etc, 1967.
- [10] A.C.B. Bogaerds, M.A. Hulsen, G.W.M. Peters, and F.P.T Baaijens. Stability analysis of injection molding flows. *J. Rheol.*, 48:765–785, 2002.
- [11] A.N. Brooks and T.J.R. Huges. Streamline upwind/ Petrov-galerkin formulation for convection dominated flows with particular emphasis on the incompressible Navier-Stokes equations. *Comput. Methods Appl. Mech. Engrg.*, 32:199–259, 1982.
- [12] L. Caspers. *Vip, an integral approach to the simulation of injection moulding*. PhD thesis, Eindhoven University of Technology, Eindhoven, The Netherlands, 1995.

- [13] S.C. Chen, N.T. Cheng, and S.Y. Hu. Simulations of primary and secondary gas penetration for a gas-assisted injection molded thin part with gas channel. *J. Appl. Polym. Sci.*, 67:1553–1563, 1997.
- [14] H.H. Chiang, C.A. Hieber, and K.K. Wang. A unified simulation of the filling and postfilling stages in injection molding. part 1: formulation. *Polym. Eng. Sci.*, 31:116–124, 1991.
- [15] H.H. Chiang, C.A. Hieber, and K.K. Wang. A unified simulation of the filling and postfilling stages in injection molding. part 2: Experimental verification. *Polym. Eng. Sci.*, 31:125–139, 1991.
- [16] H.H. Chiang, K. Himasekhar, N. Santhanam, and K.K. Wand. Integrated simulation of fluid flow and heat transfer in injection molding for the prediction of shrinkage and warpage. *J. Eng. Mater. Technol.*, 115:37–47, 1993.
- [17] R.M. Christensen. A critical evaluation for a class of micromechanics models. *J. Mech. Phys. Solids*, 38:379–404, 1990.
- [18] D.J. Coyle, J.W. Blake, and C.W. Macosko. The kinematics of fountain flow in mold-filling. *AIChE J.*, 33:1168–1177, 1987.
- [19] Y. Dimakopoulos and J. Tsamopoulos. Gas-assisted injection molding with fluids partially occupying straight or complex tubes. *Polym. Eng. Sci.*, 46:47–68, 2005.
- [20] M. Doi and S.F. Edwards. *The theory of polymer dynamics*. Clarendon Press, Oxford, 1986.
- [21] J. Donea, A. Huerta, J.-Ph Ponthon, and A. Ferran-Rodríguez. Arbitrary lagrangian-eulerian methods. In E. Stein, R. de Borst, and T.J.R Hughes, editors, *Encyclopedia of Computational Mechanics.*, volume 1, chapter 14. John Wiley & Sons, Ltd., Verlagsgesellschaft mbH, P.O.Box 10 11 61, D-69451 Weinheim, 2004.
- [22] L.F.A. Douven. *Towards the computation of properties of injection moulded products*. PhD thesis, Eindhoven University of Technology, Eindhoven, The Netherlands, 1991.
- [23] L.F.A. Douven, F.P.T. Baaijens, and H.E.H. Meijer. The computation of properties of injection-moulded products. *Prog. Polym. Sci.*, 20:403–457, 1995.
- [24] G. Eder and H. Janeschitz-Kriegl. Processing of polymers. In H.E.H Meijer, editor, *Material Science and Technology*, volume 18, chapter 5. VCH, Verlagsgesellschaft mbH, P.O.Box 10 11 61, D-69451 Weinheim, 1997.
- [25] P.J. Flory. Thermodynamics of crystallization in high polymers, crystallization induced by stretching. *J. Chem. Phys.*, 15:397–408, 1947.

- [26] F. Folgar and C.L. Tucker. Orientation behavior of fibers in concentrated suspensions. *J. Reinf. Plast. Compos.*, 3:98–119, 1984.
- [27] M. Fujiyama and T. Wakino. Structure of skin layer in injection-molded polypropylene. *J. Appl. Polym. Sci.*, 35:29–49, 1988.
- [28] R. Glowinski, T-W. Pan, T.I. Hesla, D.D. Joseph, and J. Périaux. A distributed lagrange multiplier/fictitious domain method for flows around moving rigid bodies: application to particulate flow. *Int. J. Numer. Methods Fluids*, 30:1043–1066, 1999.
- [29] A.M. Grillet, A.M. Bogaerds, G.W.M. Peters, F.P.T. Baaijens, and M. Bulters. Numerical analysis of flow mark surface defects in injection molding flow. *J. Rheol.*, 46:651–669, 2002.
- [30] L.M. Gutjahr and H. Becker. Scrim technology. *Kunststoffe*, 79:874, 1989.
- [31] G.A.A.V. Haagh and F.N. Van de Vosse. Simulation of three-dimensional polymer mould filling processes using a pseudo-concentration method. *Int. J. Numer. Methods Fluids*, 28:1355–1369, 1998.
- [32] D. Hansen and G.A. Bernier. Thermal conductivity of polyethylene: the effects of crystal size, density and orientation on the thermal conductivity. *Polym. Eng. Sci.*, 12:204, 1972.
- [33] D. Hansen and C.C. Ho. Thermal conductivity of high polymers. *J. Polym. Sci., Part A: Polym. Chem.*, 3:659, 1965.
- [34] C.H.V. Hastenberg, P.C. Wildervank, and A.J.H. Leeden. The measurement of thermal stresses distributions along the flow path in injection-molded flat plates. *Polym. Eng. Sci.*, 32:506–515, 1998.
- [35] C.A. Hieber. Modeling/simulating the injection molding of isotactic polypropylene. *Polym. Eng. Sci.*, 42:1387–1409, 2002.
- [36] C.A. Hieber and S.F. Shen. A finite-element/finite-difference simulation of the injection-molding filling process. *J. Non-Newtonian Fluid Mech.*, 7:1–32, 1980.
- [37] J.D. Hoffman and J.I. Lauritzen. Crystallization of bulk polymers with chain folding: theory of growth of lamellar spherulites. *J. Res. Natl. Bur. Stand.*, 65: 297–336, 1961.
- [38] M. Houska and M. Brummell. Characterization of molecular orientation in injection-molded thermoplastics by transmission and reflection infrared spectroscopy. *Polym. Eng. Sci.*, 27:917–924, 1987.
- [39] J.-W. Housmans, L. Balzano, D. Santoro, G.W.M. Peters, and H.E.H. Meijer. A design to study flow induced crystallization in a multipass rheometer. *Int. Polym. Proc.*, submitted, 2009.

- [40] J.-W. Housmans, M. Gahleitner, G.W.M. Peters, and H.E.H. Meijer. Structure-property relations in molded, nucleated isotactic polypropylene. *Polymer*, submitted, 2009.
- [41] J.-W. Housmans, R.J.A. Steenbakkers, P.C. Roozmond, G.W.M. Peters, and H.E.H. Meijer. Saturation of pointlike nuclei and the transition to oriented structures in flow-induced crystallization of isotactic polypropylene. *Macromolecules*, submitted, 2009.
- [42] D. Hristova and G.W.M. Peters. personal communication, 2009.
- [43] B.S. Hsaio, L. Somani, R.H. Avila-Orta, and C.A. Zhu. Unexpected shish-kebab structure in a sheared polyethylene melt. *Phys. Rev. Lett.*, 94:117802, 2005.
- [44] A.M. Hulsen, R. Fattal, and R. Kupferman. Flow of viscoelastic fluids past a cylinder at high weissenberg number: stabilized simulations using matrix logarithms. *J. Non-Newtonian Fluid Mech.*, 127:27–39, 2005.
- [45] W.R. Hwang, M.A. Hulsen, and H.E.H. Meijer. Direct simulations of particle suspensions in viscoelastic fluid in sliding bi-periodic frames. *J. Non-Newtonian Fluid Mech.*, 121:15–33, 2004.
- [46] W.R. Hwang, M.A. Hulsen, H.E.H. Meijer, and T.H. Kwon. Direct numerical simulations of suspensions of spherical particles in a viscoelastic fluid in sliding tri-periodic domains. In *XIVth International Congress on Rheology*, pages CR10–1 to CR10–3, Seoul, Korea, Republic of, 2004.
- [47] F. Ilinca and J.-F. Hetu. Three-dimensional filling and post-filling simulation of polymer injection molding. *Int. Polym. Proc.*, 16:291–301, 2001.
- [48] F. Ilinca and J.-F. Héту. Three-dimensional finite element solution of gas-assisted injection moulding. *Int. J. Numer. Methods Eng.*, 53:2003–2017, 2002.
- [49] F. Ilinca and J.-F. Hetu. Numerical investigation of the flow front behaviour in the co-injection moulding process. *Int. J. Numer. Methods Fluids*, 50:1445–1460, 2005.
- [50] A.I. Isayev, G. D. Shyu, and C.T. Li. Residual stress development in the injection molding of polymers. *Polym-Plast. Technol. Eng.*, 22:177–232, 1984.
- [51] K.M.B. Jansen. *Calculation and control of heat transfer in injection moulding*. PhD thesis, Technische Universiteit Delft, Delft, The Netherlands, 1993.
- [52] P. Jerschow and H. Janeschitz-Kriegl. On the development of oblong particles as precursors for polymer crystallization from shear flow: Origin of the so-called fine grained layers. *Rheol. Acta*, 35:127–133, 1996.
- [53] P. Jerschow and H. Janeschitz-Kriegl. The role of long molecules and nucleating agents in shear induced crystallization of isotactic polypropylenes. *Int. Polym. Proc.*, 22:72–77, 1997.

- [54] L. Johnson, P. Olley, and P.D. Coates. Gas assisted injection moulding. finite element modelling and experimental validation. *Plastics, Rubber and Composites*, 29:31–37, 2000.
- [55] P. Juhász, J. Varga, K. Belina, and H. Marand. Determination of the equilibrium melting point of the  $\beta$ -form of polypropylene. *J. Therm. Anal. Calorim.*, 69: 561–574, 2002.
- [56] G. Kalay, R.A. Sousa, R.L. Reis, A.M. Cunha, and M.J. Bevis. The enhancement of the mechanical properties of a high-density polyethylene. *J. Appl. Polym. Sci.*, 73:2473–2483, 1999.
- [57] M.R. Kamal and V. Tan. Orientation in injection molded polystyrene. *Polym. Eng. Sci.*, 19:558–563, 1979.
- [58] M.R. Kamal, R. A.L. Fook, and Aguilar J. R. H. Residual thermal stresses in injection moldings of thermoplastics: a theoretical and experimental approach. *Polym. Eng. Sci.*, 42:1098–1114, 1988.
- [59] M.R. Kamal, S.K. Goyai, and E. Chu. Simulation of injection mold filling of viscoelastic polymer with fountain flow. *AIChE J.*, 34:94–106, 1988.
- [60] A. Kech, H.-C. Ludwig, B. Moginger, P. Eyerer, and J. de Claville Christiansen. Push-pull. *Int. Polym. Proc.*, 15:202–207, 2000.
- [61] A. Keller and H.W.H. Kolnaar. Processing of polymers. In H.E.H Meijer, editor, *Material Science and Technology*, volume 18, chapter 5. VCH, Verlagsgesellschaft mbH, P.O.Box 10 11 61, D-69451 Weinheim, 1997.
- [62] P. K. Kennedy. *Practical and scientific aspects of injection molding simulation*. PhD thesis, Eindhoven University of Technology, Eindhoven, The Netherlands, 2008.
- [63] R.E. Khayat, A. Derdouri, and L.P. Herbert. A three dimensional boundary-element approach to gas-assisted injection molding. *J. Non-Newtonian Fluid Mech.*, 57:253–270, 1995.
- [64] K.H. Kim, A.I. Isayev, and K. Kwon. Flow-induced crystallization in the injection molding of polymers: A thermodynamic approach. *J. Appl. Polym. Sci.*, 95: 502–523, 2005.
- [65] S. Kimata, T. Sakurai, Y. Nozue, T. Kasahara, N. Yamaguchi, T. Karino, M. Shibayama, and J.A. Kornfield. Molecular basis of the shish-kebab morphology in polymer crystallization. *Science*, 316:1014–1017, 2007.
- [66] E.T.J. Klompen. *Mechanical properties of solid polymers: constitutive modelling of long and short term behaviour*. PhD thesis, Eindhoven University of Technology, Eindhoven, The Netherlands, 2005.

- [67] A.N. Kolmogoroff. On the statistic of crystallization development in metals. *Isvest Akad Nauk SSSR Ser Math*, 1:335, 1937.
- [68] G. Kumaraswamy. Crystallization of polymers from stressed melts. *J. Macromol. Sci., Polym. Rev.*, 45:375–397, 2005.
- [69] G. Kumaraswamy, R.K. Verma, A.M. Issaian, P. Wang, J.A. Kornfield, F. Yeh, B.S. Hsiao, and R.H. Olley. Shear-enhanced crystallization in isotactic polypropylene part2. analysis of the formation of the oriented "skin". *Polymer*, 41:8931–8940, 2000.
- [70] G. Lamberti and V. Brucato. Real-time orientation and crystallinity measurements during the isotactic polypropylene film-casting process. *J. Polym. Sci., Part B: Polym. Phys.*, 41:998, 1008, 2003.
- [71] G. Lamberti, G.W.M. Peters, and G. Titomanlio. Crystallinity and linear rheological properties of polymers. *Int. Polym. Proc.*, 22:303, 310, 2007.
- [72] C.T. Li, J.W. Shin, and Isayev A.I. Primary and secondary gas penetration during gas-assisted injection molding.part 1: formulation and modeling. *Polym. Eng. Sci.*, 44:983–991, 2004.
- [73] C.T. Li, J.W. Shin, and Isayev A.I. Primary and secondary gas penetration during gas-assisted injection molding.part 2: simulation and experiment. *Polym. Eng. Sci.*, 44:992–1002, 2004.
- [74] S. Liedauer, G. Eder, H. Janeschitz-Kriegl, P. Jerschow, W. Geymayer, and E. Inghic. On the kinetics of shear-induced crystallization of polypropylene. *Int. Polym. Proc.*, 8:236–244, 1993.
- [75] S. Liedauer, G. Eder, and H. Janeschitz-Kriegl. Crystallization in polypropylene melts. *Int. Polym. Proc.*, 10:243–250, 1995.
- [76] A.E. Likhtman and R.S. Graham. Simple constitutive equation for linear polymer melts derived from molecular theory: Rolie-poly equation. *J. Non-Newtonian Fluid Mech.*, 114:1–12, 2003.
- [77] M.R. Mackley, R.T.J. Marshall, and J.B.A.F. Smeulders. The multipass rheometer. *J. Rheol.*, 39:1293–1309, 1995.
- [78] C.W. Macosko. *Rheology: principles, measurements, and applications*. Wiley-VCH, New York, 1994.
- [79] A.YA. Malkin, V.P. Beghishev, I.A. Keapin, and Bolgov A. General treatment of polymer crystallization kinetcis-part 1. a new macrokinetic equation and its experimental verification. *Polym. Eng. Sci.*, 24:1396–1401, 1984.
- [80] J.F. Mandell, K.L. Smith, and D.D. Huang. Effects of residual stress and orientation on the fatigue of injection molded polysulfone. *Polym. Eng. Sci.*, 21: 1173–1180, 1981.

- [81] J.A. Martins, W. Zhang, and A.M. Brito. Saturation of shear-induced isothermal crystallization of polymers at the steady state and the entanglement-disentanglement transition. *Macromolecules*, 39:7626–7634, 2006.
- [82] H. Mavridis, A.N. Hrymak, and J. Vlachopoulos. The effect of fountain flow on molecular orientation in injection molding. *J. Rheol.*, 32:639–663, 1988.
- [83] H.E.H. Meijer. Processing of polymers. In H.E.H Meijer, editor, *Material Science and Technology*, volume 18, chapter 1. VCH, Verlagsgesellschaft mbH, P.O.Box 10 11 61, D-69451 Weinheim, 1997.
- [84] K. Nakamura, T. Watanabe, K. Katayama, and T. Amano. Some aspects of non-isothermal crystallization of polymers. 1. relationship between crystallization temperature, crystallinity, and cooling conditions. *J. Appl. Polym. Sci.*, 16:1077–1091, 1972.
- [85] S. Osher and S. Fedkiw. *Level set methods and dynamic implicit surfaces*. Springer-Verlag, New York, 2003.
- [86] R. Pantani, I. Coccorullo, V. Speranza, and G. Titomanlio. Modeling of morphology evolution in the injection molding process of thermoplastic polymers. *Prog. Polym. Sci.*, 30:1185–1222, 2005.
- [87] R. Pantani, I. Coccorullo, V. Speranza, and G. Titomanlio. Morphology evolution during injection molding: Effect of packing pressure. *Polymer*, 48:2778–2790, 2007.
- [88] T.D. Papathanasiou and M.R. Kamal. Filling of a complex-shaped mold with a viscoelastic polymer. part i: the mathematical model. *Polym. Eng. Sci.*, 33: 400–409, 1993.
- [89] M.A. Parvez, N.S. Ong, Y.C. Lam, and S.B. Tor. Gas-assisted injection molding: the effects of process variables and gas channel geometry. *J. Mater. Process. Technol.*, 121:27–35, 2002.
- [90] G.W.M. Peters, P.J.L. van der Velden, and H.E.H. Meijer. Multilayer injection moulding. *Int. Polym. Proc.*, 9:258–265, 1994.
- [91] A. Polynkin, J.F.T. Pittman, and J. Sienz. 3d simulation of gas assisted injection molding analysis of primary and secondary gas penetration and comparison with experimental results. *Int. Polym. Proc.*, 20:191–201, 2005.
- [92] D.V. Rosato and D.V. Rosato. *Injection molding handbook*. ITP, New York, 3rd edition, 2000.
- [93] Y. Saad and M.H. Schultz. Gmres: a generalized minimal residual algorithm for solving nonsymmetric linear systems. *SIAM, J. Matrix Anal.*, -:121–137, 1992.



- [94] R.J. Samuels. Infrared dichroism, molecular structure, and deformation mechanisms of isotactic polypropylene. *Die Makromolekular Chemie*, 4:241–270, 1981.
- [95] W. Schneider, J. Berger, and A. Kopp. Non-isothermal crystallization of polymers: Application of rate equations. *Physico-Chemical Issues in Polymers*, -:1043–1054, 1993.
- [96] B. Schrauwen. *Deformation and failure of semi-crystalline polymer systems*. PhD thesis, Eindhoven University of Technology, Eindhoven, The Netherlands, 2003.
- [97] B.A.G. Schrauwen, L.C.A. v. Breemen, A.B. Spoelstra, L.E. Govaert, G.W.M. Peters, and H.E.H Meijer. Structure, deformation, and failure of flow-oriented semicrystalline polymers. *Macromolecules*, 37:8618–8633, 2004.
- [98] A. Segal. *SEPRAN manual*. Leidschendam, The Netherlands, 1995.
- [99] M. Seki, D.W. Thurman, J.P. Oberhauser, and J.A. Kornfiel. Shear-mediated crystallization of isotactic polypropylene: the role of long-chain overlap. *Macromolecules*, 35:2583–2594, 2002.
- [100] C.-Y. Shen, Y.-G. Zhou, G.-Q. Zheng, C.-T. Liu, J.-B. Chen, and Q. Li. Stretching-induced  $\beta$ -crystal of ipp: Influence of stretching ratio. *Polym. Eng. Sci.*, 48: 2454–2458, 2008.
- [101] C.W. Shoemaker. *Moldflow design guide. A resource for plastic engineers*. Hanser Gardner publications, New York, 2006.
- [102] C.A. Silva, J.C. Viana, G.R. Dias, and A.M. Cunha. Mold for manipulation microstructure development. *Int. Polym. Proc.*, 20:27–34, 2005.
- [103] C.A. Silva, J.C. Viana, and A.M. Cunha. Manipulation of the microstructure of injection moldings in a special mold and their mechanical behavior. *Macromol. Mater. Eng.*, 291:1422–1435, 2006.
- [104] C.A. Silva, J.C. Viana, and A.M. Cunha. Novel morphologies produced by active shear rotation during injection molding. *Macromol. Mater. Eng.*, 292:655–665, 2007.
- [105] C.A. Silva, J.C. Viana, and A.M. Cunha. Fiber orientation in injection molding with rotating flow. *Polym. Eng. Sci.*, 48:395–404, 2008.
- [106] J.C. Simo. On a fully three-dimensional finite-strain viscoelastic damage model: formulation and computational aspects. *Comput. Methods Appl. Mech. Engrg.*, 60:153–173, 1987.
- [107] C.W.M. Sitters. *Injection moulding*. PhD thesis, Eindhoven University of Technology, Eindhoven, The Netherlands, 1988.

- [108] J. Smirnova, L. Silva, B. Monasse, J.-L. Chenot, and J.-M. Haudin. Structure development in injection molding. *Int. Polym. Proc.*, 20:178–185, 2005.
- [109] R.H. Somani, L. Yang, Hsiao B.S., and H. Fuitwala. Nature of shear-induced primary nuclei in ipp melt. *J. Macromol. Sci. Part B Phys.*, 42:515–531, 2003.
- [110] R.H. Somani, L. Yang, L. Zhu, and Hsiao B.S. Flow-induced shish-kebab precursor structures in entangled polymer melts. *Polymer*, 46:8587–8623, 2005.
- [111] E. I. Souheng Wu. Chain structure and entanglement. *J. Polym. Sci., Part B: Polym. Phys.*, 27:723–741, 1989.
- [112] R.J.A. Steenbakkers and G.W.M. Peters. Suspension-based rheological modeling of crystallizing polymer melts. *Rheol. Acta*, 47:643–665, 2008.
- [113] R.J.A. Steenbakkers and G.W.M. Peters. Flow-induced crystallization kinetics of polymers within the framework of rheological modeling. *in preparation*, 2009.
- [114] L.C.E. Struik. Orientation effects and cooling stresses in amorphous polymers. *Polym. Eng. Sci.*, 18:799–811, 1978.
- [115] F.H.M. Swartjes. *Stress Induced Crystallization in Elongational Flow*. PhD thesis, Eindhoven University of Technology, Eindhoven, The Netherlands, 2001.
- [116] Z. Tadmor. Molecular orientation in injection molding. *J. Appl. Polym. Sci.*, 18:1753–1772, 1974.
- [117] E. Thompson. Use of pseudo-concentrations to follow creeping viscous flows during transient analysis. *Int. J. Numer. Methods Fluids*, 6:749–761, 1986.
- [118] M.C. Tobin. The theory of phase transition kinetics with growth site impingement. ii. heterogeneous nucleation. *J. Polym. Sci., Part B: Polym. Phys.*, 14:2253–2257, 1976.
- [119] L.S. Turng, V.W. Wang, and K.K. Wang. Numerical simulation of co-injection molding filling process. *J. Eng. Mater. Technol.*, 115:48–53, 1993.
- [120] B.H.A.A. van den Brule and S.B.G. O'Brien. Anisotropic conduction of heat in a flowing polymeric material. *Rheol. Acta*, 29:580–587, 1990.
- [121] M.H.E. Van der Beek. *Specific volume of polymers. Influence of thermomechanical history*. PhD thesis, Eindhoven University of Technology, Eindhoven, The Netherlands, 2005.
- [122] J.A.W. van Dommelen, D.M. Parks, M.C. Boyce, W.A.M. Brekelmans, and F.P.T. Baaijens. Micromechanical modeling of intraspherulitic deformation of semicrystalline polymers. *Polymer*, 44:6089–6101, 2003.

- [123] D.W. van Krevelen. *Properties of Polymers*. Elsevier Science B.V., Amsterdam, The Netherlands, 1990.
- [124] R. van Loon, P.D. Anderson, J. de Hart, and F.P.T. Baaijens. A combined fictitious domain/adaptive meshing method for fluid-structure interaction in heart valves. *Int. J. Numer. Methods Fluids*, 46:533, 2004.
- [125] J. Van Meerveld, G.W.M. Peters, and M. Hütter. Towards the classification of flow induced crystallization experiments of polymer melts. *Rheol. Acta*, 44: 119–134, 2004.
- [126] J. Varga.  $\beta$ -modification of isotactic polypropylene: preparation, structure, processing, properties, and application. *J. Macromol. Sci. Part B Phys.*, 41:1121–1171, 2002.
- [127] J.F. Vega, D.G. Hristova, and G.W.M. Peters. Flow induced crystallization regimes and rheology of isotactic polypropylene: Effects of molecular architecture. *J. Therm. Anal. Calorim.*, submitted, 2009.
- [128] J.C. Viana, A.M. Cunha, and N. Billon. The thermomechanical environment and the microstructure of an injection moulded polypropylene copolymer. *Polymer*, 43:4185–4196, 2002.
- [129] S. Vleeshouwers and H.E.H. Meijer. A rheological study of shear induced crystallization. *Rheol. Acta*, 35:391–399, 1996.
- [130] J. Wang, C.A. Silva, J.C. Viana, F.W.J. van Hattum, A.M. Cunha, and C.L. Tucker III. Prediction of fiber orientation in a rotating compressing and expanding mold. *Polym. Eng. Sci.*, 48:1405–1413, 2008.
- [131] K. Watanabe, T. Susuki, T. Masubuchi, T. Taniguchi, J.-I. Takimoto, and K. Koyama. Crystallization kinetics of polypropylene under high pressure and steady shear flow. *Polymer*, 44:5843–5849, 2003.
- [132] R. Wimberger-Friedl, J.G. Bruin, and F.M. Schoo. Residual birefringence in modified polycarbonates. *Polym. Eng. Sci.*, 43:62–70, 2003.
- [133] W.F. Zoetelief. *Multi-component injection moulding*. PhD thesis, Eindhoven University of Technology, Eindhoven, The Netherlands, 1995.
- [134] W.F. Zoetelief, L.F.A. Douven, and J.I. Housz. Residual thermal stresses in injection molded products. *Polym. Eng. Sci.*, 36:1886–1896, 1996.
- [135] P.A. Zooler. A study of the pressure-volume-temperature relationships of four related amorphous polymers: polycarbonate, polyarylate, phenoxy and polysulfone. *Polym. Sci.*, 20:1453–1464, 1982.
- [136] H. Zuidema. *Flow induced crystallization of polymers*. PhD thesis, Eindhoven University of Technology, Eindhoven, The Netherlands, 2000.

- [137] H. Zuidema, G.W.M. Peters, and H.E.H. Meijer. Development and validation of a recoverable strain-based model for flow-induced crystallization of polymers. *Macromol. Theory Simul.*, 10:447–460, 2001.



# Samenvatting

---

Spuitgieten is een van de meest gebruikte technieken om polymere materialen vorm te geven. De techniek is populair doordat complexe geometrieën kunnen worden gerealiseerd met hoge productiesnelheden. Verbeteringen in de techniek, ingevoerd sinds de jaren 50, zijn voornamelijk gericht op verhoging van de productie-efficiency en van de productkwaliteit. Ook werden er onconventionele productietechnieken ontwikkeld, zoals gasinjectie en meercomponent-spuitgieten, terwijl daarnaast soms ook meerdere materiaalsoorten worden gebruikt, zoals bij het omspuiten van metalen of keramieke objecten. Productontwikkelaars richten zich nu op verkleining van de lengteschaal, verhogen van de precisie en voorspelling van de levensduur.

Om dit proces te ondersteunen zijn in de laatste 30 jaar verschillende numerieke modellen ontwikkeld. De meeste daarvan richten zich op verbeterd productontwerp om problemen te voorkomen met inhomogeen vulgedrag, ongebalanceerde druk- en temperatuurverdelingen en typische spuitgietproblemen als positie van samenvloei-naden en luchtinsluitingen. Ook richt de modelleringaandacht zich op het voorspellen van eigenschappen, voornamelijk gefocuseerd op de voorspelling van krimp en kromtrekgedrag.

Dit proefschrift poogt bij te dragen aan de voorspelling van eindeigenschappen van gespuitgiete producten en bouwt voort op het in onze groep ontwikkelde volledig driedimensionale computermodel, VIp3D, zoals dat in Hoofdstuk 2 wordt gepresenteerd. In Hoofdstuk 3 bestuderen we amorfe polymeren gespoten via GAIM, gasinjectie, en voorspellen de stromings-geïnduceerde residu-spanningen in termen van de ingevroren moleculaire oriëntatie. Hierbij wordt een ontkoppelde berekening gebruikt waarin de elastische effecten geen invloed hebben op de kinematica van de stroming. In Hoofdstuk 4 berekenen we de temperatuur- en drukgeïnduceerde spanningen, gebruikmakend van een gelineariseerd visco-elastisch constitutief model. De 3D resultaten worden vergeleken met 2D berekeningen bekend uit de literatuur.

Vervolgens richt de aandacht zich op semikristallijne polymeren en meer precies op de morfologie-ontwikkeling in isotactisch Polypropreen (iPP). De complexe thermo-mechanische geschiedenis die materiaaldeeltes ondergaan in het spuitgietproces, maakt het voorspellen van kristallisatie, gegeven de sterke afhankelijkheid daarvan van de stromingscondities, niet eenvoudig; zelfs de stroming in de extruder

kan invloed hebben. Vandaar dat eenvoudiger stromingen, met beter gedefiniëerde begin-en randvoorwaarden, vereist zijn om de modellen voor de beschrijving van kristallisatie-kinetiek te valideren. In Hoofdstuk 5 wordt de morfologieontwikkeling in iPP bestudeerd gebruikmakend van een zogenaamde multi-pass reometer en van een capillairviscosimeter. In beide opstellingen wordt het materiaal blootgesteld aan eenduidige stromingscondities en is de geschiedenis bekend; we noemen dit prototype stromingen. Het gehanteerde model maakt gebruik van een genestelde set differentiaalvergelijkingen om stromings-geïnduceerde kristallisatie te beschrijven. De voorspelde laagdiktes, die gedeeltelijk het gevolg zijn van stromings-geïnduceerde kristallisatie, en gedeeltelijk van kristallisatie in rust, worden vergeleken met experimentele resultaten verkregen met gepolariseerde optische microscopie. De voorspelde morfologieën blijken opvallend en verheugend kwantitatief.

In Hoofdstuk 6 richten we ons op de experimentele en numerieke morfologieën zoals die zich ontwikkelen bij het spuitgieten van een schijf, waarbij gebruik is gemaakt van een nieuwe, zij het wat academische, spuitgiet-technologie waarin één helft van de matrijs tijdens injectie kan roteren en transleren. De microstructuur wordt gekarakteriseerd en de moleculaire oriëntatie gemeten. De volledige 3D simulaties blijken in staat het proces te beschrijven.

Tot slot worden in Hoofdstuk 7 de belangrijkste conclusies samengevat en aanbevelingen voor toekomstig onderzoek gegeven.

# Acknowledgments

---

The conclusion of this work is only possible due to the constant support of my colleagues at the MaTe group. Your help during these years was vast, and reminds me that knowledge, in general, can only be built in an open and supportive environment. I express a special word of gratitude to Han Meijer. I am truly thankful for the opportunity you gave me to do my PhD at MaTe, as well as for your interest in my work. Your direct criticism, and confidence in my research were essential for the completion of this thesis. I proceed to my daily-base supervisors. I express my gratitude to Patrick Anderson. Your numerical influence was decisive in defining the scope of this work. I am also thankful to Gerrit Peters, since day one I have found your sharpness challenging. I also found the many FIC group meetings particularly valuable for my research. Last, I thank António Cunha who first suggested me to visit the TU/e in 2003, though you were not directly involved in this work, you played an important part in my decision to start a PhD.

I proceed thanking the VIP-VIP3D team, on whose shoulders this work stands. I also thank Pauline Schmit (thanks for all the FTIR samples!), Anne Spoelstra and Sjef Garenfeld for their cooperation. I am also thankful to Leo Wouters and Patrick van Brakel for their constant assistance. Another word of appreciation goes to Rudi Steenbakkens, with whom I had endless discussions on flow-induced crystallization that resulted in the model proposed in Chapter 5. Also to Tae Gon Kang I am thankful for his support with FEM-related problems, and to Tim van Erp for having helped me with the FTIR measurements presented in Chapter 6. I also thank Júlio Viana for having carried out the injection molding experiments at University of Minho and characterized the samples via POLM. I am also grateful to Vinayak Khatavkar for having impersonated, in many occasions, the Sepran manual at my request (still have to make up for all those beers). Last, but definitely not least, I would like to express my gratitude to my dear friend and office companion, Izzet Özdemir, who besides having always been available to discuss problems, also helped me with MSC Marc.

All other MaTe colleagues I thank for the fun it was sharing these years with you. Without any order in mind: Matej Hrapko (best weddings are in Slovakia!), Roel Janssen (how many laps?), Marco van den Bosch (Aikido-brother in arms), my first house mates in Eindhoven: Pawan Tiwari (Indian brother) and Mohammad Ab-



ham, M.K. Singh (friendship with chaos), Jan-Willem Housmans (fastest electron in Grenoble), my first office mates (Yuriy Kasyanyuk and Roy Engelen), Gabriel Chao (Viva las Pampas!), Julien Giboz (merci pour Catia!), Mohammad Samimi (Salam Alaikum!), Cem Tasan (look to the future!), Britta Hirschberger (Zum Wohl!), Tuncay Yalcinkaya (heavy metals!), Pieter Janssen (It's nonsense!!!), Christophe Pelletier (ça marche?), Jérôme Noailly (nos vemos Muleke!), Müge Erinc (Günaydin!), Linda Tufano (Vesuvio), Reinhard and Andrea Forstner (see you in Linz!), Sebastiaan Boers (what a car!), Ana Soares (Viva a Madeira!)... and all others who I don't mention in such detail but who deserve it nonetheless: Isa Ertürk, Peter Janssen, Gwen Mulder, Rene Ubachs, Katia Viatkina, Murthy Kolluri, Yvonne Schroeder, Varvara Kouznetsova, Arash Fard, Esther Poitier, Luigi Balzano, Jules Harings, Kristel Boonen, Tom Engels, Michiel Baltussen, Alexei Balmachnov, Young Joon Choi, Mahdi Hosseini, Graham McShane. I would like also to thank MaTe's distinctive secretaries, Marleen, Yvon and Alice, for always being in good mood.

I thank my friend Sjoerd Cloos for the elegant cover he designed for this thesis (bedankt!), and to all my friends outside the TU/e world who provided me with much needed distractions from my work.

I finish by thanking my family for having stayed always in close contact. Thank you for your moral and spiritual support! *Obrigado!*

# Curriculum vitae

---

Frederico Marques Custódio was born in Leiria, Portugal, on December 3rd, 1978. He completed his pre-university secondary education in 1997 at Escola Secundária Francisco Rodrigues Lobo in Leiria. He then went to study Polymer Engineering at University of Minho. After receiving his degree in Polymer Engineering, he worked for two years as a research fellow in PIEP, an institute for polymer processing research, in Guimarães, Portugal. There, his work dealt with the development and application of new materials for an automotive seat module, and was conducted under the supervision of professor António Cunha. During his stay at PIEP he and professor António Cunha developed a new process for injection molding, which resulted in a patent.

He then started his PhD program at the Materials Technology Group in Eindhoven, under joint supervision of dr.ir. Patrick Anderson, dr.ir. Gerrit Peters and professor Han Meijer, focusing on predicting the morphology and properties of injection molded parts. He also participated in, and successfully completed, 5 modules of the post-graduate course RPK on Polymer Science: chemistry, physics, properties, processing and innovations.